Low Temperature Laboratory

Fluctuations, relaxation and proximity effect in superconducting circuits

Joonas Peltonen

Aalto University

DOCTORAL DISSERTATIONS

Aalto University publication series
DOCTORAL DISSERTATIONS 112/2011

Fluctuations, relaxation and proximity effect in superconducting circuits

Joonas Peltonen

Doctoral dissertation for the degree of Doctor of Science in Technology to be presented with due permission of the School of Science for public examination and debate in Auditorium AS1 at the Aalto University School of Science (Espoo, Finland) on the 11th of November 2011 at 12 noon.

Aalto University
School of Science
Low Temperature Laboratory
PICO group

Supervisor
Prof. Matti Kaivola

Instructor
Prof. Jukka Pekola

Preliminary examiners
Prof. Yuri Galperin, University of Oslo, Norway
Prof. Ilari Maasilta, University of Jyväskylä, Finland

Opponent
Prof. Norman Birge, Michigan State University, USA

Aalto University publication series
DOCTORAL DISSERTATIONS 112/2011

ISBN 978-952-60-4351-7 (pdf)
ISBN 978-952-60-4350-0 (printed)
ISSN-L 1799-4934
ISSN 1799-4942 (pdf)
ISSN 1799-4934 (printed)

Unigrafia Oy
Helsinki 2011

Finland

The dissertation can be read at http://lib.tkk.fi/Diss/

Aalto University

Abstract

Aalto University, P.O. Box 11000, FI-00076 Aalto www.aalto.fi

Author
Joonas Peltonen

Name of the doctoral dissertation
Fluctuations, relaxation and proximity effect in superconducting circuits

Publisher School of Science

Unit Department of Applied Physics, Low Temperature Laboratory

Series Aalto University publication series DOCTORAL DISSERTATIONS 112/2011

Field of research Engineering Physics, Physics

Manuscript submitted 23 August 2011 **Manuscript revised** 17 October 2011

Date of the defence 11 November 2011 **Language** English

☐ **Monograph** ☒ **Article dissertation (summary + original articles)**

Abstract

Mesoscopic physics investigates structures smaller than the everyday macroscopic scale but larger than the scale of individual atoms, with properties that can often only be explained in terms of the laws of quantum mechanics. A typical mesoscopic electrical component is a tunnel junction, formed by a thin insulating oxide layer separating two metallic electrodes. In this thesis, various mesoscopic circuits containing sub-micron tunnel junctions between normal (N) and superconducting (S) metals are studied experimentally at sub-kelvin temperatures. An emphasis is placed on the influence of electrical fluctuations on the systems, as well as the strong connection between electrical and thermal transport in them.

We first demonstrate that a Josephson tunnel junction between two S electrodes functions as an on-chip detector of current fluctuations in a wide band of frequencies, potentially useful for studying charge transport in various mesoscopic systems. The lifetime of the zero-voltage state in a current-biased junction is very sensitive to the fluctuations in the bias current. We are able to observe the non-Gaussian nature of the shot noise generated by electrons tunneling across another nearby tunnel junction coupled to the detector junction.

Several of the experiments in this thesis probe how the transport close to a transparent interface between a superconducting and a normal conducting electrode is modified by the phenomenon of superconducting proximity effect. We present direct measurements of electron overheating in a normal metal weak link between two superconductors, explaining the routinely observed hysteretic current-voltage characteristic. Electronic temperature is probed locally by contacting the N island to an additional S electrode via an oxide barrier (I), thereby forming an NIS tunnel junction. Connecting the S electrodes of such a proximity SNS weak link into a closed loop, we further demonstrate use of the structure as a sensitive magnetometer with low dissipation. We probe also the electronic thermal conduction of short S wires between two N terminals. Due to the inverse proximity effect, the thermal conductance is found to be strongly enhanced beyond the value for a bulk superconductor.

We consider theoretically the prospects for rectifying thermal fluctuations by an NIS junction in a suitable electromagnetic environment, thereby realizing a Brownian refrigerator. Finally, we report the observation of increased cooling power in a voltage-biased NIS junction in small applied magnetic fields. This is attributed to enhanced relaxation of the hot electrons injected into the S lead of the junction.

Keywords superconductivity, tunnel junctions, Josephson effect, proximity effect

ISBN (printed) 978-952-60-4350-0 **ISBN (pdf)** 978-952-60-4351-7

ISSN-L 1799-4934 **ISSN (printed)** 1799-4934 **ISSN (pdf)** 1799-4942

Location of publisher Espoo **Location of printing** Helsinki **Year** 2011

Pages 207 **The dissertation can be read at** http://lib.tkk.fi/Diss/

A! Aalto-yliopisto

Tiivistelmä

Aalto-yliopisto, PL 11000, 00076 Aalto www.aalto.fi

Tekijä
Joonas Peltonen

Väitöskirjan nimi
Fluktuaatiot, relaksaatio ja läheisilmiö suprajohtavissa rakenteissa

Julkaisija Perustieteiden korkeakoulu

Yksikkö Teknillisen fysiikan laitos, Kylmälaboratorio

Sarja Aalto University publication series DOCTORAL DISSERTATIONS 112/2011

Tutkimusala Teknillinen fysiikka, fysiikka

Käsikirjoituksen pvm 23.08.2011 **Korjatun käsikirjoituksen pvm** 17.10.2011

Väitöspäivä 11.11.2011 **Kieli** Englanti

☐ **Monografia** ☒ **Yhdistelmäväitöskirja (yhteenveto-osa + erillisartikkelit)**

Tiivistelmä

Mesoskooppinen fysiikka tutkii yksittäisiä atomeja suurempia rakenteita, joiden ominaisuuksien selittäminen vaatii kuitenkin usein kvanttimekaniikan käyttöä. Tyypillinen mesoskooppinen sähköinen komponentti on tunneliliitos, jonka muodostaa ohut eristävä oksidikerros kahden metallisen normaali- (N) tai suprajohtavan (S) elektrodin välissä. Tässä työssä tutkitaan kokeellisesti lukuisia mesoskooppisia sähköisiä piirejä alle yhden kelvinin lämpötiloissa. Keskeisiä painotuksia ovat sähköisen kohinan vaikutukset sekä sähkön- ja lämmönkuljetuksen kytkeytyminen toisiinsa näissä nano- ja mikrometriluokan rakenteissa.

Kahden suprajohteen välisen Josephson-tunneliliitoksen osoitetaan soveltuvan herkäksi virtakohinan mittariksi laajalla taajuusalueella. Supravirtatilan elinikä virtabiasoidussa Josephson-liitoksessa riippuu vahvasti virran kohinasta. Elektronien tunnelointi ilmaisinliitoksen kanssa samaan sähköiseen piiriin yhdistetyssä tunneliliitoksessa tuottaa raekohinaa, jonka tilastollisen jakauman poikkeama normaalijakaumasta pystytään havaitsemaan. Periaatetta voidaan yleisesti hyödyntää mesoskooppisten rakenteiden sähkönkuljetuksen tutkimuksessa.

Useat tämän väitöskirjan mittaukset havainnoivat miten sähkön- ja lämmönkuljetus muuttuvat niin sanotun suprajohtavan läheisilmiön vuoksi lähellä NS-rajapintaa. Tyypillinen ilmiötä hyödyntävä rakenne on kahden suprajohteen ja niiden välisen N-saarekkeen muodostama SNS-liitos. Tässä työssä N-saarekkeen elektronien ylikuumenemisen osoitetaan johtavan monissa kokeissa havaittuun hystereettiseen virta-jännitekäyrään. Paikallista elektronilämpötilaa mitataan NIS-tunneliliitoksella, jonka muodostaa N-saarekkeelle oksidikerroksen (I) kautta kytkeytyvä S-elektrodi. Kun SNS-liitoksen S-elektrodit on yhdistetty suprajohtavaksi silmukaksi, rakenteen osoitetaan toimivan herkkänä magneettikenttäanturina, jonka etuna ovat pienet tehohäviöt. NIS-liitoksia hyödynnetään lisäksi mitattaessa lämmönkuljetusta lyhyessä suprajohtavassa langassa N-elektrodien välillä, jossa lämmönjohtavuuden havaitaan voimistuvan käänteisen läheisilmiön vaikutuksesta.

Tässä työssä tutkitaan myös teoreettisesti kohinajäähdytystä NIS-liitoksessa: Sopivissa olosuhteissa normaalimetallin ennustetaan jäähtyvän pelkästään sähköisten fluktuaatioiden synnyttämän lämpövirran seurauksena. Lopuksi, jännitebiasoidun NIS-liitoksen jäähdytystehon havaitaan kasvavan pienessä magneettikentässä. Tätä mallinnetaan liitoksen S-elektrodiin syötettyjen kuumien elektronien parantuneella relaksaatiolla.

Avainsanat suprajohtavuus, tunneliliitos, Josephsonin ilmiö, läheisilmiö

ISBN (painettu) 978-952-60-4350-0 **ISBN (pdf)** 978-952-60-4351-7

ISSN-L 1799-4934 **ISSN (painettu)** 1799-4934 **ISSN (pdf)** 1799-4942

Julkaisupaikka Espoo **Painopaikka** Helsinki **Vuosi** 2011

Sivumäärä 207 **Luettavissa verkossa osoitteessa** http://lib.tkk.fi/Diss/

ACKNOWLEDGEMENTS

The work described in this thesis was carried out in the PICO group of the Low Temperature Laboratory (LTL), Aalto University (former Helsinki University of Technology till December 2009).

Above all, I would like to thank my instructor and research group leader, Prof. Jukka Pekola for his professional guidance, devotion, and enthusiasm towards new challenges. His practical knowledge of both experimental and theoretical methods has been invaluable to this work. I thank him as well as Prof. Mikko Paalanen, the director of LTL, for letting me take part in research at the laboratory. I am indebted to Prof. Matti Kaivola for acting as my supervisor on behalf of the Department of Applied Physics, and for swiftly taking care of the practical issues.

I wish to thank Dr. Matthias Meschke from the PICO group for teaching me a notable part of my experimental knowledge of low temperature measurements, and for the time every time I stopped by his door. I give a big thanks to all the present and former members of the group for creating the relaxed and pleasant but ambitious working environment: I am grateful to Antti Kemppinen, Jonne Koski, Ville Maisi, Juha Muhonen, and Olli-Pentti Saira for sharing the office over the years, as well as to Thomas Aref, Timothé Faivre, Simone Gasparinetti, Meri Helle, Tommy Holmqvist, Sergey Kafanov, Sarah MacLeod, Mikko Möttönen, Alexander Savin, Andrey Timofeev, Juha Vartiainen, and Youngsoo Yoon. Also the fellow students at the other groups of the laboratory, including Matti Laakso, Matti Manninen, Antti Paila, Pauli Virtanen, Juha Voutilainen, and numerous others, have made the years enjoyable.

I am greatly indebted to our collaborators Hervé Courtois, Francesco Giazotto, Tero Heikkilä, Frank Hekking, Nikolai Kopnin, Paolo Solinas, and Pauli Virtanen: A considerable part of the work described in this thesis is based on their input.

I gratefully acknowledge the financial support from the Finnish Academy of Science and Letters, Vilho, Yrjö, and Kalle Väisälä Foundation. I thank the LTL secretaries for their patience with all my questions. Similarly, I thank the technical personnel as well as students and researchers from various research groups working at the Micronova Centre for Micro and Nanotechnology, among other things for making cleanroom work seem almost as that in the office.

I thank my friends for at least trying to remind me that there is other life besides physics. Last, I express my deepest thanks to my family for the endless support and understanding during the years.

Espoo, July 2011

Joonas Peltonen

LIST OF PUBLICATIONS

This thesis consists of an overview and of the following publications.

I J. T. Peltonen, A. V. Timofeev, M. Meschke, and J. P. Pekola, *Detecting current noise with a Josephson junction in the macroscopic quantum tunneling regime*, Journal of Low Temperature Physics **146**, 135–159 (2007).

II A. V. Timofeev, M. Meschke, J. T. Peltonen, T. T. Heikkilä, and J. P. Pekola, *Wideband detection of the third moment of shot noise by a hysteretic Josephson junction*, Physical Review Letters **98**, 207001 1–4 (2007).

III J. T. Peltonen, A. V. Timofeev, M. Meschke, T. T. Heikkilä, and J. P. Pekola, *Detecting non-Gaussian current fluctuations using a Josephson threshold detector*, Physica E: Low-dimensional Systems and Nanostructures **40**, 111–122 (2007).

IV H. Courtois, M. Meschke, J. T. Peltonen, and J. P. Pekola, *Origin of hysteresis in a proximity Josephson junction*, Physical Review Letters **101**, 067002 1–4 (2008).

V M. Meschke, J. T. Peltonen, H. Courtois, and J. P. Pekola, *Calorimetric readout of a superconducting proximity-effect thermometer*, Journal of Low Temperature Physics **154**, 190–198 (2009).

VI F. Giazotto, J. T. Peltonen, M. Meschke, and J. P. Pekola, *SQUIPT - Superconducting Quantum Interference Proximity Transistor*, Nature Physics **6**, 254–259 (2010).

VII M. Meschke, J. T. Peltonen, J. P. Pekola, and F. Giazotto, *Tunnel Spectroscopy of a Proximity Josephson Junction*, arXiv:1105.3875, 5 pages, submitted for publication (2011).

VIII J. T. Peltonen, P. Virtanen, M. Meschke, J. V. Koski, T. T. Heikkilä, and J. P. Pekola, *Thermal Conductance by the Inverse Proximity Effect in a Superconductor*, Physical Review Letters **105**, 097004 1–4 (2010).

IX J. V. Koski, J. T. Peltonen, M. Meschke, and J. P. Pekola, *Laterally proximized aluminum tunnel junctions*, Applied Physics Letters **98**, 203501 1–3 (2011).

X J. T. Peltonen, M. Helle, A. V. Timofeev, P. Solinas, F. W. J. Hekking, and J. P. Pekola, *Brownian refrigeration by hybrid tunnel junctions*, Physical Review B **84**, 144505 1–14 (2011).

XI J. T. Peltonen, J. T. Muhonen, M. Meschke, N. B. Kopnin, and J. P. Pekola, *Magnetic-Field-Induced Stabilization of Non-Equilibrium Superconductivity*, arXiv:1108.1544, 5 pages, submitted for publication (2011).

Throughout the overview, these publications are referred to by their Roman numerals.

AUTHOR'S CONTRIBUTION

The author fabricated all the samples studied in publications **V**, **VI**, and **IX**, most structures for publications **IV**, **VIII**, and **XI**, and assisted in sample fabrication for publications **I**, **II**, **III**, and **VII**. The author had the main responsibility of the measurements in publications **VIII**, **IX** and **XI**, and a significant role in publications **IV** and **V**. The author assisted in the measurements described in **I**, **II**, **III**, and **VII**. All the data analysis in publications **III**, **VIII**, and **XI** as well as the numerical calculations in **X** were done by the author, and the author participated in the analysis of the measurement results for publications **I**, **II**, **IV**, **V**, and **IX**. The author wrote manuscripts **I**, **III**, **VIII**, and **X**, a major part of manuscript **XI**, part of manuscripts **VI** and **IX**, and took part in preparing manuscripts **II**, **IV**, **V**, and **VII**.

Contents

Chapter 1

Introduction

Year 2011 marks the 100th anniversary since the discovery of superconductivity, one of the most influential developments of the 20th century condensed matter physics. This macroscopic quantum phenomenon exhibited by certain metals at low temperatures and its several unique properties, above all the lossless flow of electric current, have led to a vast number of applications ranging from very strong magnets to extremely sensitive particle and electromagnetic field detectors.

Several aspects of superconductivity have been studied already for more than 60 years, including the proximity effect that takes place at an interface between a superconducting and a non-superconducting material. It describes how the properties of the structure change gradually across the boundary as the superconductivity "leaks" into the other material close to the contact [1]. The early structures consisted typically of layers of thin metallic films sandwiched on top of each other, as only the film thickness could be controlled accurately to the level of 1 nm. In the last two or three decades, advances in fabrication techniques such as electron beam lithography have made it possible to craft structures with also the lateral dimensions ranging from nano- to micrometers. Mesoscopic physics is devoted to the study of such objects, larger than the scale of atoms but smaller than the everyday macroscopic scale, with properties that can often be explained only in terms of the laws of quantum mechanics.

An important class of mesoscopic components are tunnel junctions, usually formed by a thin insulating oxide layer separating two metallic electrodes. Charge transport across the structure is due to the quantum mechanical tunneling of electrons through the insulating barrier. A Josephson tunnel junction is formed when both the electrodes are superconducting, and the dissipationless current is carried by so-called Cooper pairs, two electrons moving in a correlated fashion [2, 3]. Another kind of a Josephson weak link consists of a short piece of normal-conducting metal in direct contact with two superconductors, where the magnitude of the maximum supercurrent is determined by the proximity effect in the normal wire. In this thesis, various mesoscopic metallic structures containing superconducting and normal-conducting materials have been studied experimentally.

Properties of metallic superconductors are well known in general, but in areas such as heat transport in tunnel junction and proximity circuits, several open questions remain.

Moreover, well-controlled metallic circuits provide a model system for understanding the behavior of new components based on mixing superconducting metals with for example carbon nanomaterials, single molecules, two dimensional electron gases in semiconductor heterostructures, or exotic superconductors. The present work shows electron overheating to play a major role in determining the transport characteristics of a proximity Josephson junction. A similar structure is operated as a new type of a sensitive detector for small magnetic fields. An enhancement of thermal conductance through a short superconducting wire in good contact with normal metals is observed, relevant for better control of heat flows in detector applications of proximity structures. Likewise, the thermalization of hot quasiparticles (individual electrons) injected into a superconductor is shown to be enhanced by a small magnetic field. This can be utilized for example to construct more effective solid-state electronic refrigerators.

A more recent development in mesoscopic physics is the realization that fluctuations ever present in mesoscopic electrical circuits can be more than merely an experimental artefact to be minimized [4–6]: When a conductor is biased by an electric voltage, the current fluctuates around a certain average value. The nonequilibrium shot noise arises from the discreteness of the charge carriers, and contains additional information about the underlying charge transport mechanisms not present in the average current. Both theoretical and experimental progress has been towards the measurement and characterization of the full distribution of the fluctuations. Part of this thesis shows that the lifetime of the supercurrent state of a Josephson junction functions as a sensitive probe of shot noise, being able to distinguish the asymmetry of the current fluctuations beyond the variance. Besides providing a fingerprint of the charge transport processes, in mesoscopic systems useful work can be extracted from the fluctuations. This is analyzed in a proposed scheme of rectifying thermal fluctuations in a hybrid tunnel junction between a normal metal and a superconductor, resulting in a net cooling of the normal metal electrode.

Organization of this overview

Chapter 2 reviews the basics of superconductivity, tunnel junctions, as well as the superconducting proximity effect. Relevant experimental techniques are discussed in Ch. 3. Chapter 4 includes a brief discussion of noise and FCS in mesoscopic physics, and a summary of the experiments on the detection of non-Gaussian noise with hysteretic Josephson junctions. Chapter 5 discusses the hysteresis commonly observed in various types of lateral proximized superconducting weak links. This is followed by Ch. 6, describing experiments on the interferometer structure based on a proximity weak link. Chapter 7 analyzes the measurements of thermal conductance in a short superconducting wire under the influence of inverse proximity effect. In the last part, Ch. 8 analyzes the prospects of rectifying electrical fluctuations by a hybrid tunnel junction, towards the realization of a Brownian refrigerator. Chapter 9 describes experiments on the influence of small magnetic fields on the electronic refrigeration in hybrid tunnel junctions, showing the crucial importance of effective relaxation of excess quasiparticles in a superconductor under quasiparticle injection. Finally, Ch. 10 contains a brief summary and outlook of the work.

Chapter 2

Superconductivity, tunnel junctions, and the proximity effect

We start by discussing the phenomenon of superconductivity and one of its consequences, namely the Josephson effect.

2.1 Basic properties of BCS superconductors

The phenomenon of superconductivity was discovered in 1911 [7], when H. Kamerlingh Onnes noticed that the electrical resistance of a sample of mercury became too small to measure when it was cooled below 4.2 K. This dissipationless electrical current is a defining feature of superconducting materials. The phenomenon is manifest below a material specific critical temperature T_{C}. Aluminum (Al) is a typical metallic, low-temperature superconductor, with $T_{\mathrm{C}} \simeq 1.2$ K in bulk and reaching up to 2.7 K in thin films [8]. As explained from first principles in 1957 by the Bardeen–Cooper–Schrieffer (BCS) theory [9, 10], superconductivity is a phenomenon where the quantum nature of electrons is evident on a macroscopic scale. It is one of the most fascinating consequences of the quantum nature of matter to arise from the collective behavior of an interacting many-body system. Below T_{C}, the lowest energy state of the system is reached when electrons pair up into weakly bound Cooper pairs [11]: two electrons with opposite spins and exactly opposite momenta of equal magnitude move in a strongly correlated fashion. The formation of Cooper pairs is energetically favorable at a low enough temperature, if there is even a weak effective attractive interaction between the electrons. In a conventional superconductor such as Al, the origin of superconductivity is a phonon-mediated attractive interaction between two electrons, coherently scattering from these vibrations of the ionic lattice: One electron moving in the metal lattice attracts positive ions. As a result, other electrons are drawn closer and the electrons indirectly feel each other. The relevance of phonons to superconductivity is verified by several important experiments, where for example T_{C} was observed to depend on the Debye frequency ω_{D} and therefore the mass of the atoms forming the lattice [12, 13].

The correlation of electrons can be quantified by the position-dependent pair ampli-

tude $F(\vec{r})$, which depends on the statistical average of a pair of electron field operators [3]. The amplitude F is related to the so-called pair potential $\tilde{\Delta}(\vec{r}) = g(\vec{r})F(\vec{r})$, where $g(\vec{r})$ is the strength of the effective attractive interaction between the electrons. This complex number $\tilde{\Delta}(\vec{r})$ with magnitude $|\tilde{\Delta}(\vec{r})| \equiv \Delta$ and phase $\phi(\vec{r})$ serves as an order parameter of the superconducting state: In the ground state of a superconducting metal, all the electrons condense to the exactly same quantum state, which can be described by a single macroscopic wave function. The magnitude Δ vanishes in a normal metal or in a superconductor at temperatures above T_C, but has a finite value when the material is in the superconducting state. The temperature-dependent value $\Delta(T)$ is called the superconducting energy gap, because it gives the separation in energy between the single-particle excitations (quasiparticles) and the ground state condensate of the Cooper pairs. A minimum amount of energy Δ per electron is required to break a Cooper pair and introduce a quasiparticle excitation to the system. The Cooper pairs can carry a supercurrent without a difference in chemical potentials caused by an applied bias voltage, and dissipative electrical currents only start flowing once the temperature is high enough to break Cooper pairs.

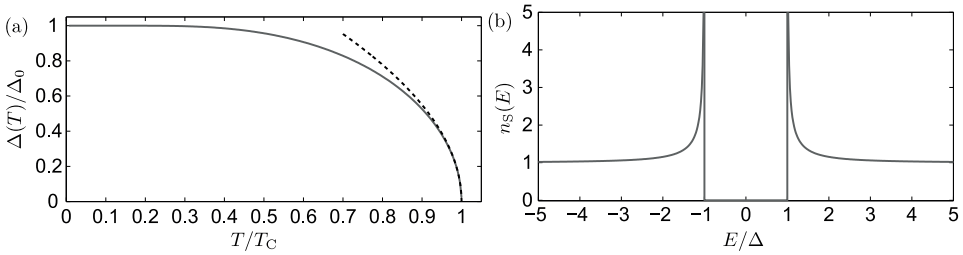

Figure 2.1: (a) Temperature dependence of the BCS energy gap Δ as a function of the reduced temperature T/T_C. (b) Normalized BCS quasiparticle density of states.

Temperature dependence of the energy gap $\Delta(T)$ can be solved from

$$\frac{1}{\lambda} = \int_{\Delta(T)}^{\hbar\omega_\mathrm{D}} dE \frac{1}{\sqrt{E^2 - \Delta(T)^2}} \tanh\left(\frac{E}{2k_\mathrm{B}T}\right), \tag{2.1}$$

where ω_D is the Debye frequency, and the dimensionless parameter λ denotes the interaction constant, characterizing the strength of the phonon-mediated attractive interaction between the electrons in the superconducting state. In low-temperature superconductors, $\lambda \ll 1$ [3]. At T_C the gap vanishes, and Eq. (2.1) gives $k_\mathrm{B}T_\mathrm{C} \simeq 1.13\hbar\omega_\mathrm{D}e^{-1/\lambda}$, demonstrating the sensitivity of T_C to the value of the interaction constant. On the other hand, in the limit of zero temperature, Eq. (2.1) yields $\Delta(0) \equiv \Delta_0 = \hbar\omega_\mathrm{D}/\sinh(1/\lambda)$. For $\lambda \ll 1$ we therefore find $\Delta_0 \simeq 1.76k_\mathrm{B}T_\mathrm{C}$. Importantly, for such weak coupling superconductors, $\Delta(T)/\Delta_0$ solved from Eq. (2.1) depends only on the quantity T/T_C, as shown in Fig. 2.1 (a). At low temperatures, $\Delta(T)$ deviates only exponentially little from Δ_0. It starts to be suppressed only when there is a considerable number of thermal quasiparticles, around $T \gtrsim T_\mathrm{C}/3$. Close to T_C, the temperature dependence is well approximated

by $\Delta(T)/\Delta_0 \simeq 1.74\sqrt{1-T/T_\mathrm{C}}$, included in Fig. 2.1 (a) as the dashed line. On the other hand, in an ideal BCS superconductor the density of states (DoS) for single-particle excitations is obtained from

$$n_\mathrm{S}(E) = \frac{|E|}{\sqrt{E^2-\Delta^2}}\theta(E^2-\Delta^2), \tag{2.2}$$

illustrated in Fig. 2.1 (b). In Eq. (2.2), the quasiparticle energy E is measured with respect to the Fermi energy E_F, and $n_\mathrm{S}(E)$ is normalized by N_0, the normal state DoS at E_F. Integrating $n_\mathrm{S}(E)$ from $-E'$ to E' with $E' \gg \Delta$ yields $2E'$, demonstrating that the total number of quasiparticle states is the same in both the normal and the superconducting state - every forbidden state within Δ from E_F is lifted above the gap. For aluminum, we have $N_0 \simeq 2 \times 10^{47}$ J^{-1}m^{-3}, and $E_\mathrm{F} \simeq 12$ eV, corresponding to a Fermi velocity $v_\mathrm{F} \simeq 2 \times 10^6$ ms^{-1} [3, 14]. Although $E_\mathrm{F} \gg \Delta_0 \simeq 200$ μeV, at temperatures $T \ll T_\mathrm{C}$ the superconducting state is well protected as the number of thermal quasiparticles is suppressed by $\exp(-\Delta/k_\mathrm{B}T)$.

2.2 Josephson junctions

The quantum coherent nature of the superconducting ground state gives rise to a large variety of phenomena, including the so-called Josephson effect [2, 3, 15–17]: As first predicted theoretically by Josephson in 1962 [18] and observed experimentally in 1963 [19], a dissipationless supercurrent can flow through a system consisting of two superconducting electrodes separated by a weak link. Figure 2.2 (a) depicts schematically one realization of such a structure, generally referred to as a Josephson junction (JJ), in the form of a SIS (Superconductor-Insulator-Superconductor) JJ, one of the most common building blocks of mesoscopic superconducting electrical circuits. Besides a thin insulating oxide layer, the weak link can be formed, e.g., by a short region of normal metal or a point-like constriction in the superconducting material. As shown in the sketch and the scanning electron micrograph of Fig. 2.2 (b), an actual SIS junction can consist of two overlapping layers of aluminum on a silicon substrate separated by a thin layer of aluminum oxide. In contrast, Fig. 2.2 (c) illustrates a lateral weak link formed by a short piece of normal-conducting metal (red) between the superconductors (blue). The supercurrent

$$I_\mathrm{S}(\varphi) = I_\mathrm{c}\sin\varphi \tag{2.3}$$

through the tunnel junction arises when there is a difference $\varphi = \phi_1 - \phi_2$ of the superconducting order parameter phase between the S electrodes. On the other hand, the phase can often to a good approximation be assumed to be a constant within each electrode. To an even better approximation the magnitude of the order parameter, i.e., the energy gap Δ is constant in the bulk of a clean superconductor. In other types of weak links the current–phase relation may not be purely sinusoidal, but contains also higher harmonics ($\sin 2\varphi$, etc.) [2].

The tunneling of electrons across a thin insulating barrier is a quantum mechanical phenomenon. In a Josephson junction the tunneling of Cooper pairs is due to the interference of the macroscopic wavefunctions of the two S electrodes. In Eq. (2.3), also known

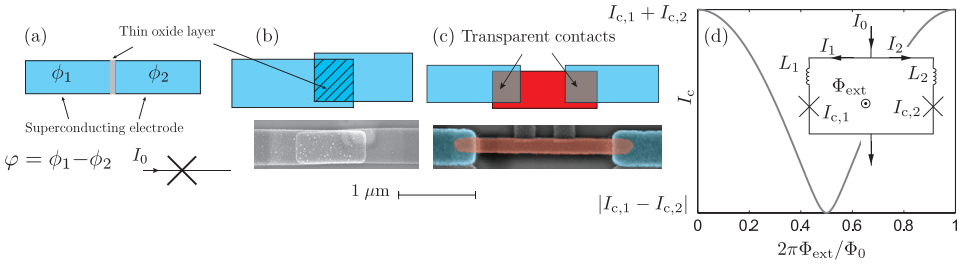

Figure 2.2: (a) Schematic drawing of a Josephson junction formed by a thin insulating layer between two S electrodes. The cross is the electrical circuit symbol for a JJ supercurrent element. (b) A more realistic overlap-type Josephson tunnel junction, together with a scanning electron micrograph of an Al-AlOx-Al junction [see Sec. 3.1]. (c) A lateral weak link, which can exhibit Josephson effect similar to a tunnel junction. (d) Flux modulation of the critical current and a schematic drawing of a DC-SQUID, consisting of two JJs in parallel in a superconducting loop.

as the DC Josephson relation, the critical current I_c sets the maximum current the junction can sustain before a finite voltage appears across the electrodes. From a microscopic tunnel Hamiltonian model of an SIS junction, I_c is found to depend on the temperature T, energy gap Δ, and the normal state resistance R_T of the junction via

$$I_c = \frac{\pi\Delta}{2eR_T} \tanh\left(\frac{\Delta}{2k_BT}\right), \tag{2.4}$$

known as the Ambegaokar-Baratoff formula [20], and valid near T_C also for other types of weak links [3]. On the other hand, based on Eq. (2.1), at $T \ll T_C$ the critical current can be considered as a temperature-independent parameter of the junction. Equation (2.3) is supplemented by the AC Josephson relation

$$V = \frac{\hbar}{2e}\frac{d\varphi}{dt}, \tag{2.5}$$

relating the voltage V across the junction to the time derivative of the phase difference. In a junction biased by a current $I < I_c$, the phase difference is constant and the current flows as supercurrent, $V = 0$. On the other hand, in a voltage biased JJ, the supercurrent alternates in time as becomes evident by integrating Eq. (2.5) and inserting the phase $\varphi(t)$ into Eq. (2.3). This AC Josephson effect was first observed in 1963 [21]. Importantly, Eq. (2.5) forms also the basis for the use of JJs as the SI standard of electrical voltage [22, 23]. Biasing a JJ by an AC current with a very accurately known frequency causes an accurately defined voltage to appear over the structure. Moreover, Eqs. (2.3) and (2.5) can be combined to integrate the electrical work to give the free energy $\int dt I_S V = \text{ const. } - E_J \cos\varphi$ stored in the junction. Here, $E_J = \hbar I_c/(2e)$ is the Josephson energy, characterizing the strength of the coupling between the two junction electrodes.

To observe the phase-dependent supercurrent, $E_\mathrm{J} \gtrsim k_\mathrm{B}T$ is required to overcome the smearing by thermal fluctuations.

So far the discussion has been limited to the Josephson effect in a single junction. Importantly, connecting two junctions in parallel into a superconducting loop opens up new possibilities when the loop is threaded by an external magnetic flux Φ_ext. In such a structure denoted as a DC SQUID (DC Superconducting Quantum Interference Device) [24, 25], see inset of Fig. 2.2 (d), it turns out that the gauge-invariant phase differences φ_1 and φ_2 across the individual junctions are constrained by $\varphi_1 - \varphi_2 = 2\pi\Phi/\Phi_0 \pmod{2\pi}$, known as the relation of flux quantization [3]. Here $\Phi_0 = h/(2e) \simeq 2.07 \times 10^{-15}$ Wb is the magnetic flux quantum, and $\Phi = \Phi_\mathrm{ext} - \Phi_\mathrm{ind}$ the total flux through the loop with Φ_ind denoting the induced screening flux due to to circulating current in the loop. In the limit of negligible loop inductance, $\Phi = \Phi_\mathrm{ext}$. Combining this constraint, the DC Josephson relation of Eq. (2.3), and the requirement of current conservation, it follows that the two-junction SQUID behaves as a single JJ with the flux-modulated critical current $I_\mathrm{c} = \sqrt{I_{\mathrm{c}1}^2 + I_{\mathrm{c}2}^2 + 2I_{\mathrm{c}1}I_{\mathrm{c}2}\cos(2\pi\Phi_\mathrm{ext}/\Phi_0)}$ [2]. This modulation is illustrated in Fig. 2.2 (d) for $I_{\mathrm{c}2}/I_{\mathrm{c}1} = 0.8$. Flux-dependence of the SQUID critical current forms the basis for the use of JJs as extremely sensitive detectors of magnetic field [24, 26], as well as controllable artificial atoms for quantum computing [27]. In this work, DC SQUIDs are utilized in **I** as JJs with tunable critical current. Moreover, in **VI** and **VII** flux quantization allows to control the phase difference across a single SNS weak link embedded into a superconducting loop, forming a different kind of an interferometer structure.

2.2.1 The RCSJ model

To describe how the phase difference evolves in time in a JJ current biased above I_c, or to predict the shape of the current–voltage (IV) characteristic, the model needs to be extended beyond Eqs. (2.3) and (2.5). One of the most widely employed descriptions of JJs is the Resistively and Capacitively Shunted Junction (RCSJ) model [2, 28, 29], where a JJ is treated as a parallel combination of a capacitance C, an ideal Josephson tunneling element with the current–phase relation given by Eq. (2.3), and an effective resistance R (or more generally a frequency dependent admittance), see inset of Fig. 2.3 (a). The finite geometric capacitance between the junction electrodes and a possible shunting capacitance are modeled through C, whereas R describes the dissipative equilibrium environment of the junction at temperature T, assumed to generate equilibrium current fluctuations $\delta I_\mathrm{th}(t)$ with zero mean and variance $\langle \delta I_\mathrm{th}(t)\delta I_\mathrm{th}(t')\rangle = 2k_\mathrm{B}T\delta(t-t')/R$. For a JJ biased by a possibly time-dependent current $I_\mathrm{b}(t) = I_0 + \delta I(t)$, requirement of current conservation yields the classical Langevin equation

$$I_0 + \delta I_\mathrm{th}(t) + \delta I(t) = I_\mathrm{c}\sin\varphi(t) + \frac{\hbar}{2eR}\dot{\varphi}(t) + \frac{C\hbar}{2e}\ddot{\varphi}(t). \tag{2.6}$$

Multiplying Eq. (2.6) by $\hbar/2e$ allows us to write it in the form

$$m\ddot{\varphi}(t) + U'(\varphi(t)) + m\gamma\dot{\varphi}(t) = \xi(t) + \eta(t), \tag{2.7}$$

corresponding to the damped motion of a particle of mass $m \equiv \hbar^2 C/(4e^2)$ along the φ–coordinate in the tilted periodic Josephson cosine potential

$$U(\varphi) = -E_\mathrm{J}\left(\frac{I_0}{I_\mathrm{c}}\varphi + \cos\varphi\right). \tag{2.8}$$

In Eq. (2.7), $\gamma \equiv 1/(RC)$ is the damping constant, $\xi(t) \equiv \hbar\delta I_\mathrm{th}(t)/(2e)$ with $\langle\xi(t)\xi(t')\rangle = (2m\gamma/\beta)\delta(t-t')$ the random force acting on the particle, and $\eta(t) \equiv \hbar\delta I(t)/(2e)$ is the external time-dependent, possibly random driving force. Introducing the charging energy $E_\mathrm{C} = e^2/(2C)$ of the junction allows us to write the mass as $m = \hbar^2/(8E_\mathrm{C})$. Above, $\beta = (k_\mathrm{B}T)^{-1}$ is the inverse temperature, and the prime denotes the differentiation $d/d\varphi$ whereas the dot stands for d/dt. As shown in Fig. 2.3 (c), the tilt of the "washboard" potential is set by the constant bias current I_0: at $I_0 = I_\mathrm{c}$ the local potential minima (wells) disappear.

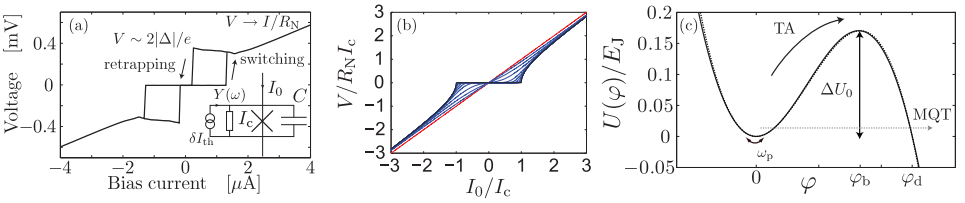

Figure 2.3: (a) Hysteretic IV curve of a typical weakly damped JJ, showing the supercurrent at zero voltage and the sudden switch to the finite voltage state (the quasiparticle branch). Inset: Equivalent circuit of a JJ in the RCSJ model. (b) IV characteristics of an overdamped junction at different temperatures. (c) One well–barrier segment of the cosine potential (solid) and its cubic approximation (dashed) for $I_0 = 0.8I_\mathrm{c}$. The well is located at $\varphi = 0$ and the barrier top at φ_b. ΔU_0 denotes the dimensionless barrier height and φ_d its maximum width, whereas ω_p is the oscillation frequency at the potential minima. Arrows sketch the MQT and TA escape processes discussed in Sec. 2.2.2.

In view of Eq. (2.8), we can understand the main features of an IV characteristic of a typical SIS JJ such as the one illustrated in Fig. 2.3 (a). For simplicity, we consider initially the limit of zero temperature and negligibly weak damping, set $\eta(t) = 0$ and neglect any quantum effects. We take the potential of Eq. (2.8) to be shifted so that it has a minimum at $\varphi = 0$ and a maximum at $\varphi = \varphi_\mathrm{b}$ as in Fig. 2.3 (c). Then, for bias currents $I_0 < I_\mathrm{c}$ the particle sits at one of the potential minima. This point is characterized by the curvature-related plasma frequency $\omega_\mathrm{p} = \sqrt{U''(0)/m}$. At nonzero temperatures, ω_p gives the typical classical oscillation frequency of the particle around the minimum. A localized phase with $\langle\dot{\varphi}\rangle = 0$ corresponds to the junction being in the zero voltage, i.e., supercurrent state. As the bias current is increased to $I_0 \gtrsim I_\mathrm{c}$, the junction switches abruptly to its finite voltage state and the phase starts rolling freely down the potential hill. This picture of a switching event remains valid also for nonzero damping, as long as the junctions are underdamped with a quality factor $Q = \omega_\mathrm{p}RC > 1/\sqrt{2}$.

In this thesis, in the experiments involving SIS junctions, we employed only weakly damped junctions. For such JJs with large capacitance, switching from the supercurrent to the dissipative state has a very sharp dependence on the bias current, making them useful as threshold detectors of current: A bias current $I_0 \gtrsim I_c$ is easily detectable as a voltage $\simeq 2\Delta/e$ quickly develops over the junction. Moreover, as shown in Fig. 2.3 (a), the IV curves of underdamped junctions are strongly hysteretic, making it easier to observe that the junction has escaped from the supercurrent state. Once the junction has switched to the normal state, the phase will continue running down the potential without retrapping (re-localization) to any of the subsequent local minima until the bias current is reduced below a certain retrapping current $I_r \ll I_c$ [3, 30]. This current is indicated also in Fig. 2.3 (b). For weakly damped junctions, an approximate criterion for I_r is obtained by equating the energy difference between two adjacent local potential maxima to the energy dissipated when the phase moves from one maximum to another, giving $I_r \simeq 4I_c/(\pi Q_r)$, where Q_r is another inversely damping-dependent quality factor, generally different from Q.

On the other hand, for the lateral SNS weak links with a short normal metal between two superconducting electrodes described in this work, both the geometric capacitance and the resistance R are small compared to the SIS junctions. Consequently, $Q \ll 1$, and the phase dynamics are overdamped. The particle is either localized or moves diffusively from one minimum to the next. Neglecting the $\ddot{\varphi}(t)$–term in Eq. (2.7) and setting $\eta(t) = 0$, one finds the zero temperature IV characteristic to satisfy $V = R\sqrt{I_0^2 - I_c^2}$: For $I_0 < I_c$ the junction is in the supercurrent state, whereas ohmic behavior is recovered at $I_0 \gg I_c$. For such SNS junctions, a finite temperature will result in smearing of the characteristic. To analyze this as well as the behavior of SIS junctions at finite temperatures, one can solve the stochastic differential equation of Eq. (2.7), or the equivalent Fokker-Planck equation.

For convenience we introduce the dimensionless bias current $x_0 = I_0/I_c$ and write the plasma frequency explicitly as $\omega_p = \sqrt{8E_J E_C \varphi_0}/\hbar$. Here, $\varphi_0 = \sqrt{1 - x_0^2}$ accounts for the change of the oscillation frequency due to the bias dependent tilt of the potential. When dealing with underdamped junctions, we can neglect retrapping of the phase and concentrate on a single well–barrier segment of the potential, and approximate $U(\varphi)$ by the third order polynomial [see Fig. 2.3 (c)]

$$U(\varphi) \simeq 3\Delta U \left(\frac{\varphi}{\varphi_b}\right)^2 \left(1 - \frac{2}{3}\frac{\varphi}{\varphi_b}\right) = \frac{1}{2} m\omega_p^2 \varphi^2 \left(1 - \frac{2}{3}\frac{\varphi}{\varphi_b}\right), \tag{2.9}$$

which gives identical values at every x_0 for the barrier height and curvatures at the well bottom and the barrier top, when compared to the full expression for the cosine potential. The φ–coordinate is measured with respect to the potential minimum which is simultaneously the zero level of energy. Importantly, the height of the barrier is given by $\Delta U \equiv \Delta U_0 E_J = 2E_J\,(\varphi_0 - x_0 \arccos x_0) \simeq 4\sqrt{2}E_J\,(1 - x_0)^{3/2}/3$, where the last approximation is valid in the limit $x_0 \to 1$.

In the absence of the external fluctuations $\eta(t)$, Eq. (2.6) is the classical Langevin equation for damped motion in a tilted periodic potential, valid for $\beta\hbar\omega_p \ll 1$, and forming the starting point for extensive research on Brownian motion [31–33]. These investigations

of Brownian motion can be generalized to the very low temperature limit $\beta\hbar\omega_\mathrm{p} \gg 1$, where quantum nature of the macroscopic φ–variable becomes essential. In the potential of Eq. (2.9), the problem is that of a particle escaping from a metastable well. The essential task is to find the the lifetime of the metastable state, or its inverse, the decay rate of the state [34, 35]. Metastability means that the barrier height ΔU is high compared to the temperature and the plasma frequency, so that it makes sense to define an escape rate Γ, which then is the largest timescale of the problem. At $\Delta U \simeq k_\mathrm{B}T$, retrapping and phase diffusion become relevant, and a single unambiguous escape rate cannot be defined. The lifetime is the average time it takes for a particle initially localized in the well region to make a transition to the free running state. At finite temperatures, the phase can escape from the local minima over the barrier top by classical thermal activation (TA) due to the random force $\xi(t)$ from thermal fluctuations, even if $I_0 < I_\mathrm{c}$. This is a stochastic process, so that for example the switching and retrapping currents in an underdamped JJ are observed to vary randomly. On the other hand, at the lowest temperatures the escape occurs via macroscopic quantum tunneling (MQT) through the barrier. These two escape mechanisms are illustrated in Fig. 2.3 (c).

2.2.2 Escape from a metastable state

Neglecting quantum effects, the average lifetime can be calculated by stochastic simulation of the Langevin equation of Eq. (2.7). For an analytic estimate of the escape rate, an alternative starting point is the Fokker-Planck equation for the phase space probability distribution $P(\varphi, \dot\varphi, t)$ [36]

$$\frac{\partial P}{\partial t} = -v\frac{\partial P}{\partial \varphi} + \frac{1}{m}\frac{\partial U(\varphi)}{\partial \varphi}\frac{\partial P}{\partial v} + \gamma\left[P + v\frac{\partial P}{\partial v} + \frac{1}{m\beta}\frac{\partial^2 P}{\partial v^2}\right]. \tag{2.10}$$

Here, the velocity $v = \dot\varphi$ is to be treated as an independent variable. The form of Eq. (2.10) is based on the properties $\langle\xi(t)\rangle = 0$ and $\langle\xi(t)\xi(t')\rangle = (2m\gamma/\beta)\delta(t-t')$ of the white Gaussian thermal noise. As reviewed for example in [34, 36–38], the widely used classical Kramers rate for escape by thermal activation [39] is then obtained by a flux-over-population –prescription as

$$\Gamma = \frac{j_\mathrm{b}}{n_0} = \frac{\int_{-\infty}^{\infty} d\varphi \int_{-\infty}^{\infty} dv\; vP(\varphi, v)\delta(\varphi - \varphi_\mathrm{b})}{\int_{-\infty}^{\infty} d\varphi \int_{-\infty}^{\infty} dv\; P(\varphi, v)} = \frac{\int_{-\infty}^{\infty} dv\; vP(\varphi_\mathrm{b}, v)}{\int_{-\infty}^{\infty} d\varphi \int_{-\infty}^{\infty} dv\; P(\varphi, v)}. \tag{2.11}$$

Here, j_b is the probability current out of the potential well calculated at the barrier top, whereas n_0 is the population of the well. Once a probability-current-carrying solution $P(\varphi, v)$ has been found, one obtains

$$\Gamma^\mathrm{TA} = \frac{\omega_\mathrm{r}}{2\pi}\exp\left[-\frac{\Delta U}{k_\mathrm{B}T}\right] \quad \text{with} \quad \omega_\mathrm{r} = \omega_\mathrm{p}\left(\sqrt{\frac{1}{4Q^2}+1} - \frac{1}{2Q}\right). \tag{2.12}$$

The result can be viewed as a product of an attempt frequency $\omega_\mathrm{r}/(2\pi)$ and an exponential activation factor $\exp[-\Delta U/(k_\mathrm{B}T)]$. The part of this work related to on-chip detection of shot noise deals with the question of how this escape rate is affected by additional

nonequilibrium fluctuations $\eta(t)$. For typical experimental parameters we can approximate $\omega_r \simeq \omega_p$ and concentrate on changes in the dominating exponential factor. The Q–dependent prefactor can be thought to diminish the attempt frequency $\omega_p/(2\pi)$ due to dissipative recrossings of the barrier. This formula is valid for intermediate to high dissipation $Q \lesssim \Delta U/(k_B T)$: we assumed the dissipation to be strong enough so that the well region remains at thermal equilibrium. At very high Q–values corresponding to low dissipation, the escape is limited by energy diffusion instead of spatial diffusion as in the analysis of this section. However, dissipation affects only the prefactor of the rate — the exponential factor $\Delta U/(k_B T)$ remains the same. This Kramers turnover problem has been analyzed for example in [34, 36, 38].

As mentioned above, at low temperatures with $\hbar\omega_p \gg k_B T$, another channel for the escape of the phase from the well dominates the overbarrier TA: In the MQT process the phase tunnels through the barrier and the junction enters the finite voltage state. In the limit of low temperatures and negligible dissipation the junction can be described in terms of the ideal Hamiltonian

$$\mathcal{H} = \frac{\hat{q}^2}{2C} - E_J \cos\hat{\varphi} - \frac{\hbar}{2e} I\hat{\varphi}, \tag{2.13}$$

where $\hat{q}$ and $\hat{\varphi}$ are now the quantum mechanical conjugate charge and phase operators satisfying $[\hat{q}, \hat{\varphi}] = 2ei$. It can be viewed as a quantum analog of Eq. (2.7), and in the limit $E_J \gg E_C$ relevant for this work the junction behaves as a quantum particle in the potential $U(\varphi)$, with approximately $\Delta U/(\hbar\omega_p)$ metastable energy levels in the well. At $T = 0$, $Q \gg 1$ only the ground level is populated, and the MQT escape happens from this energy. The effects of finite T and Q can be analyzed in terms of a master equation [40, 41], including the transitions between the levels and the tunneling rate out of the well starting at each level.

The MQT phenomenon and its dependence on the dissipative environment has been analyzed at length in [42–45]. Its experimental observation [46–53] gave remarkable evidence in favor of quantum behavior of a macroscopic, collective variable. In the MQT regime the decay rate Γ becomes almost independent of T. The transition from TA to MQT behavior in the decay process of the metastable supercurrent state occurs around the crossover temperature $T_{cr} = \hbar\omega_r/(2\pi k_B)$ [38, 45] above which thermal hopping prevails. For large capacitance junctions with $E_J \gg E_C$ the phase is a good quantum number, and charging effects can be neglected. In the limit $T \to 0$ the rate of MQT from the ground state in the potential well is approximated by $\Gamma^{MQT} = Ae^{-B}$, bearing close resemblance to the TA rate. In the MQT regime, however, the prefactor

$$A = \frac{\omega_p}{2\pi} 12\sqrt{6\pi} \sqrt{\frac{\Delta U}{\hbar\omega_p}} \left[1 + \frac{1.43}{Q} + \mathcal{O}(1/4Q^2)\right] \tag{2.14}$$

and, importantly, the exponent

$$B = \frac{36}{5} \frac{\Delta U}{\hbar\omega_p} \left[1 + \frac{45\zeta(3)}{2\pi^3 Q} + \mathcal{O}(1/4Q^2)\right] \tag{2.15}$$

differ from those in Eq. (2.12). Here, $\zeta(z)$ is the Riemann zeta-function with $\zeta(3) \simeq 1.202$. The above rate expressions for TA and MQT are valid in the high and low temperature

limits, respectively. For a very crude estimate of the rate in the crossover region one can simply sum up these contributions. This is in acceptable agreement with experiments but neglects the complicated interplay between quantum tunneling and thermal fluctuations [38].

2.2.3 Measuring the escape rate

In Sec. 2.2.2 we introduced the RCSJ model of JJs and discussed how an underdamped junction initially in its metastable supercurrent state has a certain decay rate Γ to the finite voltage state. To probe Γ experimentally, we measure the escape probability $P_{\rm esc}$ from the supercurrent state at different bias currents I_0. The rate Γ is related to the probability $P_{\rm stay} = 1 - P_{\rm esc}$ of the JJ staying in the supercurrent state via

$$\frac{dP_{\rm stay}(t)}{dt} = -\Gamma(t)P_{\rm stay}(t), \quad \text{or} \quad P_{\rm stay}(t) = \exp\left[-\int_0^t dt'\Gamma(t')\right], \tag{2.16}$$

where the time dependence of Γ is determined by that of the bias current. For a bias pulse of constant height I_0 and duration Δt, switched on adiabatically at $t = 0$, Eq. (2.16) gives

$$P_{\rm esc} = 1 - e^{-\Gamma(I_0)\Delta t}. \tag{2.17}$$

Due to the exponential I_0-dependence of Γ, trapezoidal bias current pulses with rise times well exceeding 10% of Δt can be used, and the escape happens dominantly at the plateau value of the current. For a hysteretic underdamped junction the transition to the normal state is observed as a voltage $\simeq 2\Delta/e$ developing over the junction, which is easy to detect experimentally. For a large number N, $10^3 - 10^4$ in a typical experiment, of bias current pulses fed through the junction, the escape probability is obtained as the fraction $P_{\rm esc} = N_{\rm switch}/N$, where $N_{\rm switch}$ is the number of observed voltage pulses. A short section of a typical sequence of I_0-pulses fed through the junction and the randomly appearing voltage pulses are included in Fig. 2.4 (a). In this manner, $P_{\rm esc}$ is determined up to a statistical error $\Delta P = \sqrt{P_{\rm esc}\left(1 - P_{\rm esc}\right)/N}$ due to the standard deviation of the binomially distributed switching events.

For a fixed pulse length Δt, there is a certain range of currents I_0 over which $P_{\rm esc}$ changes from 0 to 1. To characterize the shape of a typical S-shaped $P_{\rm esc}(I_0)$ –curve, known as the cumulative escape probability histogram, we define the switching current I_x according to $P_{\rm esc}(I_x) = x$. One pays attention especially to the middle point $I_{0.5}$ and the width $\Delta I = I_{0.9} - I_{0.1}$ of the curve as a function of different parameters. In the regime of thermal activation, based on Eq. (2.12), we find that the histogram middle position and the width are decreasing functions $\propto (k_{\rm B}T/E_{\rm J})^{2/3}$ [53, 54]. On the other hand, in the MQT regime, the position and width become almost independent of T, allowing to determine the crossover temperature $T_{\rm cr}$ if a broad range of T is covered. The symbols in Fig 2.4 (a) show a set of histograms measured with $\Delta t = 400$ μs and $N = 10^4$ in a relatively short range of T. The positions and widths at the highest temperatures are compared to the TA model with $C = 80$ fF and $I_{\rm c} = 0.65$ μA, neglecting dissipation. The predicted crossover temperature is $T_{\rm cr} \simeq 200$ mK. With these values of $I_{\rm c}$ and C, the

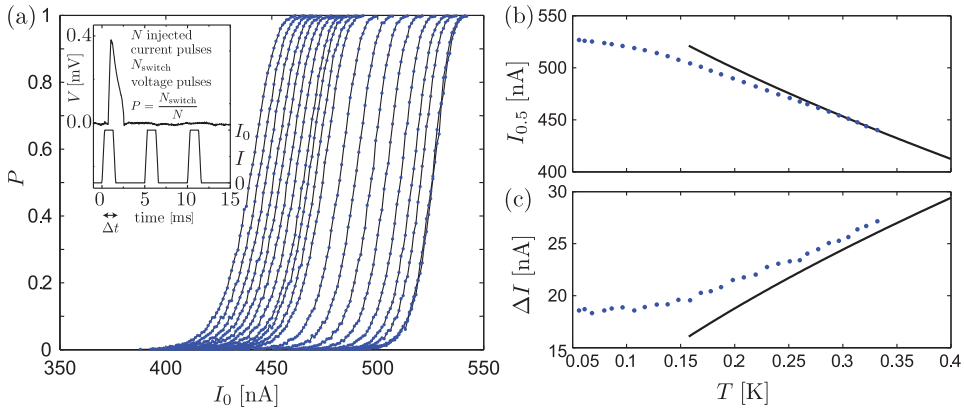

Figure 2.4: (a) Measured escape probability histograms for a single JJ at various bath temperatures. Inset: Principle of determining the escape probability. (b)–(c) Histogram positions and widths as a function of T, extracted from (a). The lines show the prediction of the TA model with $Q \gg 1$.

MQT formula with $Q \gg 1$ predicts that the histogram position and middle point saturate to $I_{0.5} \simeq 530$ nA and $\Delta I \simeq 15$ nA. The slightly higher observed saturation in ΔI can be partially attributed to the neglect of dissipation, as well as low frequency noise in the bias current due to imperfect filtering which tends to increase the histogram width (see [55] and **I**).

2.3 Quasiparticle tunneling in hybrid junctions

In the previous sections we considered fully superconducting Josephson junctions, and properties of the supercurrent due to the tunneling of Cooper pairs. In this section we review the tunneling of quasiparticles in a general hybrid tunnel junction between two electrodes. An important special case is the normal metal – insulator – superconductor (NIS) junction, in which one of the electrodes is a BCS superconductor such as Al, and the other electrode is a normal metal, e.g., Cu. Quasiparticle tunneling in such a structure biased by a voltage V is illustrated in Fig. 2.5 (a) on the energy diagram. On the left, the normal metal distribution function is plotted with the energy axis in the vertical direction. The barrier is in the middle, whereas the right side sketches the superconductor DoS, showing the occupied states below $-\Delta$, and the empty ones above $+\Delta$. The quasiparticles have a finite probability of absorbing energy from fluctuations in the electromagnetic environment of the junction, indicated by the function $P(E - E')$. The arrows indicate the process of a qp at energy E in the normal metal absorbing energy $E' - E$ while tunneling and ending at E' in the S electrode. The junction environment is modeled according to the circuit in Fig. 2.5 (b), consisting of the junction capacitance C, and a frequency-dependent impedance $Z(\omega)$ at temperature T_R. A shunt capacitor across the

junction combines to C, or can be contained in $Z(\omega)$.

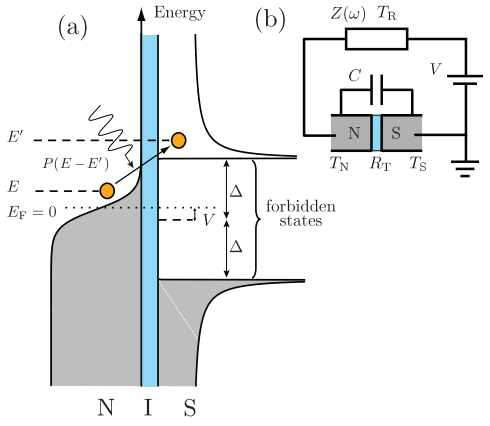

Figure 2.5: (a) Schematic representation of qp tunneling in a voltage biased NIS junction. (b) Circuit model for an NIS junction in a dissipative environment.

To calculate the electric and heat currents in the junction, we utilize the standard $P(E)$-theory (for a review, see [56, 57]) describing a tunnel junction embedded in a general electromagnetic environment [58–60]. The starting point is the Hamiltonian $H = H_{\rm qp} + H_{\rm T} + H_{\rm env}$, where

$$H_{\rm qp} = \sum_{k\sigma} \epsilon_k c^\dagger_{k\sigma} c_{k\sigma} + \sum_{q\sigma} \epsilon_q c^\dagger_{q\sigma} c_{q\sigma} \tag{2.18}$$

describes quasiparticles with wave vectors k and q, spin σ, and energies ϵ_k and ϵ_q in the two leads of the junction. $c^\dagger$ and c denote the fermionic quasiparticle creation and annihilation operators, whereas

$$H_{\rm T} = \sum_{kq\sigma} T_{kq} c^\dagger_{q\sigma} c_{k\sigma} e^{-i\varphi} + \text{H.c.} \tag{2.19}$$

is the tunneling Hamiltonian describing the annihilation of a quasiparticle with wave vector k and spin σ, and the creation of a quasiparticle with q and σ in the other electrode (and vice versa). In Eq. (2.19), T_{kq} is the tunneling matrix element corresponding to this process, and φ is the phase operator conjugate to the charge on the junction, with the operator $\exp(-i\varphi)$ having the effect of changing the junction charge by e, the charge of one electron. Finally, $H_{\rm env}$ describes the environment of the junction, which does not have to be specified microscopically at this point. A tunneling Hamiltonian description requires the two electrodes to be only weakly coupled, whence the theory is perturbative in the junction conductance and neglects higher order tunneling processes. The basic theory can be, however, extended to deal with higher conductances [61]. For simplicity, we assume the normal state tunneling resistance $R_{\rm T}$, proportional to the inverse of the average tunneling matrix element $|T^2|$, to satisfy $R_{\rm T} \gg R_{\rm K}$ with the resistance quantum $R_{\rm K} \equiv h/e^2 \simeq 26$ kΩ. In addition, the theory assumes that charge equilibrium prevails

before each tunneling event, so that the time between the tunneling events should exceed the charge relaxation time. Also, the voltage is assumed to drop sharply across the barrier.

We start by writing down the particle and energy rates in a general hybrid junction biased by a constant voltage V, with normalized DoS $n_i(E)$ in each electrode ($i = 1, 2$). We furthermore assume that the two conductors are in (quasi) equilibrium, i.e., their energy distribution functions obey the Fermi-Dirac form $f_i(E) = 1/(1 + \exp(\beta_i E))$ with the inverse temperature $\beta_i = (k_\mathrm{B} T_i)^{-1}$. Here, importantly, the temperatures T_i need not be equal, and the energies are measured with respect to the Fermi level. In general the electrode temperatures are determined consistently by the various heat fluxes in the complete system, usually via coupling to the lattice phonons at a certain bath temperature. The assumption of quasiequilibrium requires electron-electron relaxation to be much faster compared to other channels, mainly compared to the electron-phonon relaxation. Only then the distribution functions can be written with the help of an effective, in general position-dependent, temperature [62]. Many of the following results require only the electron-hole symmetry $f_i(E) = 1 - f_i(-E)$ to hold.

In a Fermi Golden rule approximation, after tracing out states of the environment, the total electron tunneling rate from electrode i to electrode j reads [56]

$$\Gamma^{+} = \frac{1}{e^2 R_\mathrm{T}} \int_{-\infty}^{\infty} \int_{-\infty}^{\infty} dE dE' n_i(E) n_j(E' + eV) f_i(E) \left[1 - f_j(E' + eV)\right] P(E - E'). \quad (2.20)$$

We assume $i \to j$ to be the forward direction favored by a positive bias voltage V. The function $P(E)$ is obtained as the Fourier transform

$$P(E) = \frac{1}{2\pi\hbar} \int_{-\infty}^{\infty} dt \exp\left[J(t) + iEt/\hbar\right], \quad (2.21)$$

with the phase-phase correlation function $J(t)$ defined as

$$J(t) = \langle \varphi(t)\varphi(0)\rangle - \langle \varphi(0)\varphi(0)\rangle = \frac{1}{2\pi} \int_{-\infty}^{\infty} d\omega S_\varphi(\omega) \left[e^{-i\omega t} - 1\right]. \quad (2.22)$$

Here, $S_\varphi(\omega)$ is the spectral density $S_\varphi(\omega)$ of the phase fluctuations $\varphi(t)$, i.e., the average value of $\varphi(t)$ satisfies $\langle \varphi(t)\rangle = 0$. Equations (2.21) and (2.22) assume Gaussian statistics of the phase. For stationary fluctuations one has $S_\varphi(\omega) = \int_{-\infty}^{\infty} d\omega e^{i\omega t} \langle \varphi(t)\varphi(0)\rangle$. To relate $P(E)$ and $J(t)$ to more physical quantities, we use the fundamental defining relation between the phase $\varphi(t)$ and the voltage fluctuation $\delta V(t)$ across the junction. We have $\varphi(t) = (e/\hbar) \int_{-\infty}^{t} dt' \delta V(t')$, from which it follows that in the frequency domain the relation $\varphi(\omega) = (e/\hbar)\delta V(\omega)/(-i\omega)$ holds. Consequently, $S_\varphi(\omega)$ is connected to the voltage noise spectral density $S_V(\omega)$ at the junction via $S_\varphi(\omega) = (e/\hbar)^2 S_V(\omega)/\omega^2$. This formulation [63], emphasizing the influence of the environment through the fluctuations it generates, is especially useful if the electrical environment as seen from the junction cannot be reduced to a parallel impedance $Z(\omega)$ at a single, unique temperature T_R. For instance, the junction can be coupled via reactive, i.e., non-dissipative, elements to multiple noise sources, possibly at differing temperatures. The voltage noise $S_V(\omega)$ at the junction can be further expressed in terms of a transimpedance $Z_\mathrm{T}(\omega)$, and the spectral

density $S_I(\omega)$ of intrinsic current fluctuations generated in the dissipative element that forms the environment, i.e, $S_V(\omega) = |Z_\mathrm{T}(\omega)|^2 S_I(\omega)$. For a given $Z(\omega)$ and a temperature $k_\mathrm{B}T_\mathrm{R} = \beta_\mathrm{R}^{-1}$ of the environment, the uniquely defined function $P(E)$ can be interpreted as the probability density per unit energy for the tunneling particle to exchange energy E with the environment [56], with $E > 0$ corresponding to emission and $E < 0$ to absorption. With Fig. 2.5 (a) and this interpretation at hand, it is straightforward to arrive at the tunneling rate in Eq. (2.20) with the correct occupation factors and energy arguments. In an analogous manner, we obtain the backward tunneling rate from j to i as

$$\Gamma^- = \frac{1}{e^2 R_\mathrm{T}} \int_{-\infty}^{\infty}\int_{-\infty}^{\infty} dE dE' n_i(E) n_j(E'+eV)\left[1-f_i(E)\right] f_j(E'+eV) P(E'-E). \quad (2.23)$$

Assuming an equilibrium environment consisting of $Z(\omega)$ at T_R, the function $J(t)$ in Eq. (2.22) can be written as

$$J(t) = 2\int_0^\infty \frac{d\omega}{\omega} \frac{\mathrm{Re}\left[Z_\mathrm{t}(\omega)\right]}{R_\mathrm{K}} \{\coth(\beta_\mathrm{R}\hbar\omega/2)[\cos(\omega t)-1] - i\sin(\omega t)\}. \quad (2.24)$$

Here, $Z_\mathrm{t}(\omega) = 1/[i\omega C + Z^{-1}(\omega)]$, is the total impedance as seen from the tunnel junction, i.e., a parallel combination of the "external" impedance $Z(\omega)$ and the junction capacitance C. This corresponds to a source of current fluctuations with the spectral density

$$S_I(\omega) = \hbar\omega \mathrm{Re}[Z(\omega)^{-1}][\coth(\beta_\mathrm{R}\hbar\omega/2)+1], \quad (2.25)$$

transforming to voltage noise across the junction with the transimpedance $Z_\mathrm{T} = Z_\mathrm{t}$. Inserting $J(t)$ from Eq. (2.24) into Eq. (2.21), one importantly finds that $P(E)$ is positive for all E, is normalized according to $\int_{-\infty}^{\infty} dE P(E) = 1$, and satisfies detailed balance $P(-E) = \exp(-\beta_\mathrm{R}E)P(E)$: at low T_R, absorbing an energy E from the environment is exponentially suppressed compared to the probability for emission.

Utilizing the symmetry of the DoS around $E = 0$ and the property $f_i(E) = 1 - f_i(-E)$ of the Fermi function, we note that Eqs. (2.20) and (2.23) can be rewritten in the form

$$\Gamma^\pm = \frac{1}{e^2 R_\mathrm{T}} \int_{-\infty}^{\infty}\int_{-\infty}^{\infty} dE dE' n_i(E \mp eV) n_j(E') f_i(E \mp eV)\left[1-f_j(E')\right] P(E-E'). \quad (2.26)$$

With the tunneling rates at hand, the quasiparticle current through the junction reads

$$I(V) = e\left[\Gamma^+(V) - \Gamma^-(V)\right] = \frac{1}{eR_\mathrm{T}} \int_{-\infty}^{\infty}\int_{-\infty}^{\infty} dE dE' n_j(E')\left[1-f_j(E')\right] P(E-E') \times \left\{ n_i(E-eV) f_i(E-eV) - n_i(E+eV) f_i(E+eV) \right\}. \quad (2.27)$$

Similarly to the particle tunneling rates in Eq. (2.26), we write down the energy flow of forward tunneling quasiparticles from electrode i to electrode j as

$$\dot{Q}^+ = \frac{1}{e^2 R_\mathrm{T}} \int_{-\infty}^{\infty}\int_{-\infty}^{\infty} dE dE' n_i(E) n_j(E'+eV) E f_i(E)\left[1-f_j(E'+eV)\right] P(E-E'). \quad (2.28)$$

For the backward tunneling from j to i we have

$$\dot{Q}^- = \frac{1}{e^2 R_\mathrm{T}} \int_{-\infty}^{\infty}\int_{-\infty}^{\infty} dE dE' n_i(E) n_j(E'+eV) E f_j(E'+eV)\,[1-f_i(E)]\,P(E'-E), \quad (2.29)$$

and the net heat flux out of i is given by $\dot{Q}_i = \dot{Q}^+ - \dot{Q}^-$. Again, the argument of $P(E)$ has differing sign for the two opposite processes, corresponding to either emission or absorption from the environment. Utilizing the same symmetries as when manipulating Eqs. (2.20) and (2.23) into Eq. (2.26), the net heat flow reads

$$\begin{aligned}\dot{Q}_i =& \frac{1}{e^2 R_\mathrm{T}} \int_{-\infty}^{\infty}\int_{-\infty}^{\infty} dE dE' n_i(E) E f_i(E) P(E-E') \times \\ & \Big\{ n_j(E'+eV)\left[1-f_j(E'+eV)\right] + n_j(E'-eV)\left[1-f_j(E'-eV)\right] \Big\}. \end{aligned} \quad (2.30)$$

As a special case, let us consider an NIS junction with an energy-independent DoS in the N electrode close to E_F, $n_\mathrm{N}(E) \equiv 1$, and an S electrode with the smeared BCS DoS $n_\mathrm{S}(E) = |\mathrm{Re}[(E+i\gamma)/\sqrt{(E+i\gamma)^2-\Delta^2}]|$. Here, the small parameter $\gamma \ll \Delta$ accounts for the finite lifetime of the quasiparticles due to inelastic scattering [64]. It is also often used as a phenomenological parameter to account for the sub-gap current observed in practical NIS junctions [65, 66]. A further important limit is a low-impedance environment $\mathrm{Re}[Z_\mathrm{t}(\omega)] \ll R_\mathrm{K}$ in which only elastic tunneling is allowed, $P(E-E') = \delta(E-E')$. This corresponds to the typical on-chip environment of a junction without special careful engineering, as the impedance is of the order of the vacuum impedance. In this case, Eqs. (2.27) and (2.30) simplify considerably, yielding the standard expression [62, 67, 68] for the qp current

$$\begin{aligned} I(V) &= \frac{1}{eR_\mathrm{T}} \int_{-\infty}^{\infty} dE n_\mathrm{S}(E)\,[f_\mathrm{N}(E-eV) - f_\mathrm{S}(E)] \\ &= \frac{1}{2eR_\mathrm{T}} \int_{-\infty}^{\infty} dE n_\mathrm{S}(E)\,[f_\mathrm{N}(E-eV) - f_\mathrm{N}(E+eV)]\,. \end{aligned} \quad (2.31)$$

The latter form demonstrates explicitly that the current in an NIS junction is sensitive only to the normal metal temperature, making it a widely used thermometer that is able to probe the temperature locally in N electrodes [62]. Temperature of the S electrode influences the IV characteristic only through the T_S-dependence of the energy gap; this is negligible at $T_\mathrm{S} \lesssim T_\mathrm{C}/3$. Importantly, in an NIS junction subjected to radiation from a hot ($k_\mathrm{B}T_\mathrm{R} \gtrsim \Delta$) ohmic environment modeled as an effective resistance $R \ll R_\mathrm{K}$, the current from Eq. (2.27) with an ideal BCS DoS ($\gamma = 0$) coincides with Eq. (2.31) with $\gamma = 2\pi(R/R_\mathrm{K})(k_\mathrm{B}T_\mathrm{R})/\Delta$ [66]. For $k_\mathrm{B}T_\mathrm{N} \ll \Delta$ and $eV \lesssim \Delta$, the Fermi functions in Eq. (2.31) can be approximated by their exponential tails. This yields

$$I \simeq \frac{2\Delta}{eR_\mathrm{T}} K_1\!\left(\frac{\Delta}{k_\mathrm{B}T_\mathrm{N}}\right) \sinh\!\left(\frac{eV}{k_\mathrm{B}T_\mathrm{N}}\right) \simeq \frac{\Delta}{eR_\mathrm{T}} \sqrt{\frac{\pi k_\mathrm{B}T_\mathrm{N}}{2\Delta}}\, e^{\frac{eV-\Delta}{k_\mathrm{B}T_\mathrm{N}}}, \quad (2.32)$$

where $K_\alpha(x)$ is the modified Bessel function of the second kind, of order α. This shows how the current increases exponentially close to Δ, as the bias voltage shifts the Fermi levels enough to allow qps to tunnel to the available states above the gap.

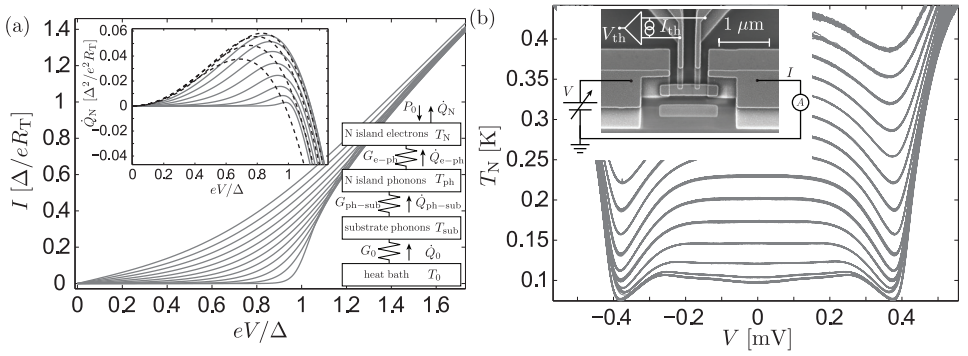

Figure 2.6: (a) Calculated IV curve of a single NIS junction at $T_\mathrm{N} = 0.05,\ 0.1, \ldots, 0.6 \times T_\mathrm{C}$. Insets: The corresponding calculated cooling power, and a general thermal model of the system. For clarity, the $\dot{Q}_\mathrm{N}$–curves for the four highest T_N are shown as dashed lines. (b) Typical measured electronic temperature of the N island as a function of the cooler bias voltage, at various bath temperatures. Inset: Scanning electron micrograph of a small N island (Cu) contacted by four NIS tunnel junctions to Al electrodes, together with the measurement scheme.

In an analogous manner, the heat extracted from N reads

$$\dot{Q}_\mathrm{N} = \frac{1}{e^2 R_\mathrm{T}} \int_{-\infty}^{\infty} dE n_\mathrm{S}(E)(E - eV) \left[f_\mathrm{N}(E - eV) - f_\mathrm{S}(E) \right]. \tag{2.33}$$

and the heat deposited into the S electrode is

$$-\dot{Q}_\mathrm{S} = \frac{1}{e^2 R_\mathrm{T}} \int_{-\infty}^{\infty} dE n_\mathrm{S}(E) E \left[f_\mathrm{N}(E - eV) - f_\mathrm{S}(E) \right], \tag{2.34}$$

so that $-\dot{Q}_\mathrm{S} = \dot{Q}_\mathrm{N} + IV$. In Fig. 2.6 (a) we show the IV characteristic of a single NIS junction calculated at several temperatures T_N. The left inset plots the cooling power $\dot{Q}_\mathrm{N}$ for various temperatures $T_\mathrm{N} = T_\mathrm{S}$. It is positive for bias voltages $eV \lesssim \Delta$ with a maximum slightly below Δ, coinciding with the onset of qp current. In this range of bias voltages, the gap acts as an energy filter, allowing only the highest energy qps to tunnel. This results in electronic cooling of the N island [62, 69]. On the other hand, at higher biases also qps below the Fermi energy can tunnel, resulting in strong heating. In the low temperature limit the cooling power can be approximated similarly to the current in Eq. (2.32). Importantly, the optimal bias voltage is $eV_\mathrm{opt} \simeq \Delta - 0.66 k_\mathrm{B} T_\mathrm{N}$, and

$$\dot{Q}_\mathrm{opt} \simeq \frac{\Delta^2}{e^2 R_\mathrm{T}} \left[0.59 \left(\frac{k_\mathrm{B} T_\mathrm{N}}{\Delta} \right)^{3/2} - \sqrt{\frac{2\pi k_\mathrm{B} T_\mathrm{S}}{\Delta}} \exp\left(-\frac{\Delta}{k_\mathrm{B} T_\mathrm{S}} \right) \right]. \tag{2.35}$$

gives the corresponding maximum cooling power.

Two NIS junctions can be connected in series back-to-back, sharing a common N electrode. In such a SINIS structure biased at $eV \simeq 2\Delta$, the electrons of a small N island can be cooled effectively below the phonon temperature $T_{\rm bath}$: One of the junctions is extracting hot electron-like qps, whereas the other one is injecting "cold" holes. This forms the basis for practical solid-state microrefrigerators [62, 70, 71]. In this work, we commonly employ a standard configuration of a single N island contacted by four NIS tunnel junctions. One pair of them acts as a SINIS cooler in a voltage biased mode, and the other pair as a SINIS thermometer at a small constant bias current $I_{\rm th}$. The current through each of the junctions in the cooler SINIS is given by Eq. (2.31) evaluated at $V/2$. On the other hand, the total cooling power is given by $2\dot{Q}_{\rm N}(V/2)$. Small junction asymmetry (differing normal state tunnel resistances $R_{\rm T,1}$ and $R_{\rm T,2}$) has only a minor effect on the IV characteristic of the series structure, because the exponential onset of the current "aligns" the voltage drops across each junction close to $V/2$ [72]. The typical measurement scheme for such a four junction structure is shown in the inset of Fig. 2.6 (b).

A calibration between the N island electron temperature and the thermometer voltage is obtained by measuring the voltage $V_{\rm th,0}$ ($V_{\rm th}$ at $V = 0$, when $T_{\rm N} \simeq T_{\rm bath}$) while varying the (cryostat) bath temperature $T_{\rm bath}$. Figure 2.6 (b) shows $T_{\rm N}$ at various $T_{\rm bath}$ when the cooler is operating. This $T_{\rm N}$ is obtained by "deconvolving" the voltage $V_{\rm th}$ with the calibration $V_{\rm th,0}$. At each $T_{\rm bath}$, a clear drop in $T_{\rm N}$ is observed at $eV \simeq \pm 2\Delta$, before the onset of heating due to hot qp injection. In this work, we typically denote the minimum temperature at $V_{\rm opt}$ by $T_{\rm N,min}$, and define the temperature drop $\Delta T = T_{\rm N,min} - T_{\rm N,0}$ relative to $T_{\rm N,0}$, the value of $T_{\rm N}$ at $V = 0$.

The right inset of Fig. 2.6 (a) includes the thermal diagram of the system. At each V and $T_{\rm bath}$, the electronic temperature $T_{\rm N}$ of the N island is determined by the balance between the cooling power $\dot{Q}_{\rm N}$ and the heat flow from the N island phonons to N electrons, and from other relevant channels. This is described by the steady-state heat balance equation

$$\dot{Q}_{\rm N} - \Sigma_{\rm N}\Omega_{\rm N}(T_{\rm ph}^5 - T_{\rm N}^5) - P_0 = 0, \tag{2.36}$$

where $T_{\rm ph}$ denotes the phonon temperature of the island. The second term gives the electron-phonon heat flow for a normal metal island of volume $\Omega_{\rm N}$ and electron phonon coupling constant $\Sigma_{\rm N}$. For Cu, $\Sigma_{\rm N} \simeq 2 \times 10^9$ Wm^{-3}K^{-5} [62]. At the millikelvin temperatures reached in a dilution refrigerator, the temperatures of electrons in a thin metal film can differ significantly from the lattice (phonon) temperature due quick weakening of the coupling between electrons and phonons at low temperatures. Already a small externally applied power $P_{\rm ext}$ is enough to heat the electrons to a significantly higher temperature. On the other hand, the weak coupling is a prerequisite for electronic refrigeration to work at low temperatures. With the exception of **XI**, in this work we neglect phonon cooling or heating [73, 74] by equating $T_{\rm ph} = T_{\rm bath}$. $T_{\rm bath}$ is the temperature of the sample holder phonons, well thermalized to the mixing chamber of the cryostat. This assumes a low Kapitza resistance between the island and the substrate, a justified assumption for the small islands at the low bath temperatures [73]. More generally, $T_{\rm ph}$ is determined by a balance of heat flow between the island and substrate phonons [62]. Finally, the constant term $P_0 \lesssim 1$ fW is a phenomenological leakage power due to connections to the

measurement electronics. It accounts for the typical saturation of the SINIS thermometer voltage $V_{\mathrm{th},0}$ as well as the saturation of $T_{\mathrm{N},0}$ in Fig. 2.6 (b) to around 100 mK even at $T_{\mathrm{bath}} \lesssim 50$ mK. In Eq. (2.36), direct Joule heating of the island due to a finite resistance of the N part is neglected, a valid approximation for N electrodes made out of Cu or other pure metals instead of resistive alloys. The thermometer bias current I_{th} is kept low enough to allow us to neglect the self-cooling of the island by the thermometer junctions. It is notable that the saturation of $T_{\mathrm{N},0}$ can in part be explained by the heating of the island by photon absorption from a 4.2 K environment due to imperfect shielding from microwaves: Setting $V = 0$ in Eq. (2.30) predicts a heating power of the correct order of magnitude, assuming a suitable RC environment [66].

2.4 Superconducting proximity effect

So far we have discussed only quasiparticle transport in general hybrid tunnel junctions, and the supercurrent in Josephson junctions. When a superconducting metal is placed into good contact with a normal-type conductor rather than through a tunnel barrier, superconducting pair correlations can penetrate into the normal metal. Close to the interface, the normal metal obtains properties reminiscent of a superconductor. This is the widely investigated superconducting proximity effect [1, 75–79]. As a typical consequence, the DoS in the normal metal is modified [80–84], and a (hard) minigap can open in the spectrum [82, 85, 86]. The resistance of an NS structure develops a non-monotonous temperature dependence [87, 88], and supercurrent can flow through an SNS weak link [89–91]. Especially in multiterminal structures several non-trivial effects are present [92–96], and the mesoscopic proximity effect remains the topic of active theoretical and experimental study.

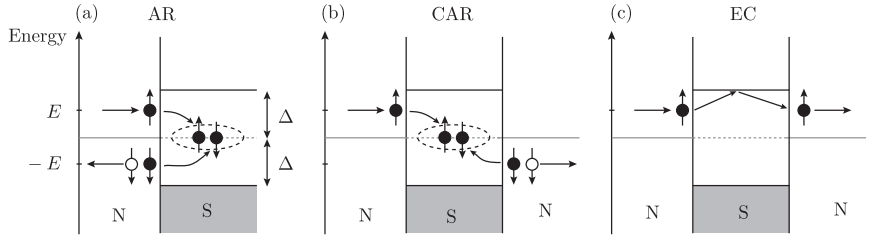

Figure 2.7: (a) Andreev reflection at a transparent NS contact: An electron (solid circle) with spin ↑ and energy E below Δ moving towards the superconductor is reflected as a hole (open circle) with spin ↓ and energy $-E$, moving into the normal metal. (b) Crossed Andreev reflection and (c) elastic cotunneling in a short NSN structure.

How is the quasiparticle current in the normal metal converted into a current of Cooper pairs, when there are no single particle states available below Δ? The mechanism was explained by Andreev in 1964 [97–99]: As illustrated in Fig. 2.7, an electron with energy $E < \Delta$ and spin ↑ impinges the S from the N side and pairs with another electron with

energy $-E$ and spin $\downarrow$. They cross into the S as a Cooper pair, so that effectively a hole with energy $-E$ and spin $\downarrow$ is retroreflected back into the normal metal, and a Cooper pair is transported into the superconductor. This is the process of Andreev reflection (AR). The hole and the electron move in a correlated fashion, showing how superconducting correlations can spread into the normal metal. Supercurrent transport through an SNS weak link can now also be understood in terms of Fig. 2.7 (a): An electron first undergoes AR at the left interface, travels across the N as a hole that is again reflected into an electron at the right interface. As a result, a Cooper pair has been transported through the structure. At certain energies (depending on the phase difference φ across the weak link), the phase-coherent hole and electron trajectories can interfere constructively, thus forming so-called Andreev bound states [90, 98] that carry the supercurrent. Such states can be conveniently used as the transmission channels in a scattering matrix description of the weak link [100].

In most thin metallic films the elastic mean free path l is generally much smaller than typical sample dimensions. The motion of the electrons through the structures is a random walk as they undergo multiple elastic collisions with impurities. In such a diffusive metal with the diffusion constant $D = v_\mathrm{F} l/3$ (v_F is the Fermi velocity of electrons), the coherence decays on the characteristic length scale set by the minimum of the phase-coherence length L_φ and the thermal coherence length $L_\mathrm{T} = \sqrt{\hbar D/(2\pi k_\mathrm{B} T)}$ [77]. Of these L_T in the range of hundreds of nanometers is usually smaller by at least an order of magnitude, setting for instance the maximum length of N for which a supercurrent is observed through an SNS junction.

Close to the NS interface also the S is modified on the scale of the superconducting coherence length $\xi_0 = \sqrt{\hbar D/\Delta}$, a phenomenon known as the *inverse* proximity effect [76, 101]: The energy gap is suppressed and the sub-gap density of states can be non-zero. In a short S wire of length $L \gtrsim \xi_0$ between two or more N terminals, additional effects arise. Figure 2.7 (b) illustrates the process of crossed Andreev reflection (CAR), where the hole is "reflected" into another N reservoir, i.e., electrons with opposite spins from two reservoirs combine into a Cooper pair [92, 102–107]. Yet another process in short S wires is the elastic cotunneling (EC) sketched in Fig. 2.7 (c), where an electron can tunnel from one N lead to the other, through a virtual state in the superconductor [92, 103]. In recent years, observation of these non-local processes have attracted a lot of interest, as they provide a solid-state source of entangled electrons needed for quantum computation [108–110].

Microscopically, the proximity effect can be described with the general theory of inhomogeneous, nonequilibrium superconductivity [111, 112], into which the properties of Andreev reflection are built-in. To be able to model mesoscopic structures with a large number of atoms, the equations are typically averaged on the scale of the Fermi wavelength, which often falls in the range of the atomic spacing for metals. The resulting quasiclassical Eilenberger equations [113] can be further simplified in the diffusive limit. For description of practical mesoscopic structures, this yields the tractable set of Usadel equations [114] for which boundary conditions for various types of interfaces have been derived [115, 116]. To obtain the equilibrium and linear response properties relevant for

this work, it is sufficient to solve the quasi-1D spectral equations [77, 117]

$$\begin{aligned}\hbar D\partial_x^2\theta &= -2iE\sinh(\theta) + \frac{\hbar D}{2}\left(\partial_x\chi\right)^2\sinh(2\theta) + 2i\Delta\cos(\phi-\chi)\cosh(\theta)\\ \hbar D\partial_x j_{\mathrm{E}} &= -2i\Delta\sin(\phi-\chi)\sinh(\theta), \quad j_{\mathrm{E}} = -\sinh^2(\theta)\partial_x\chi.\end{aligned} \tag{2.37}$$

In this parametrization of the Usadel equations, $\theta(x,E)$ and $\chi(x,E)$ are two complex valued functions that depend on the position x and the energy E. The superconducting order parameter is assumed to have the position-dependent form $\Delta e^{i\phi}$. In an S reservoir the functions θ and χ obtain the bulk values $\theta = \mathrm{artanh}(\Delta/E)$ and $\chi = \phi$, whereas in a normal reservoir $\theta(x,E) = 0$ and $\chi(x,E)$ is not defined. These equations can be straightforwardly generalized to include the effect of a small rate of inelastic or spin-flip scattering, as well as the influence (depairing) of magnetic field other than via flux quantization [14, 91, 117]. Under nonequilibrium conditions, Eq. (2.37) has to be supplemented. Then, also the electron and hole distribution functions need to be solved from a kinetic equation, requiring knowledge of the relaxation mechanisms [111, 117]. The energy gap is solved self-consistently from

$$\Delta e^{i\phi} = \frac{\lambda}{4}\int dE\,\mathrm{Re}[\sinh(\theta)e^{i\chi}]\tanh\left(\frac{E}{2k_{\mathrm{B}}T}\right), \tag{2.38}$$

where λ is a material constant characterizing the strength of superconductivity [75, 77] – in a normal metal $\lambda = 0$, and the order parameter goes abruptly to zero whereas the pair correlations implied by $\theta(x,E)$ are still finite.

Once $\theta(x)$ and $\chi(x)$ have been solved, observable properties of the structure can be calculated straightforwardly: The normalized single-particle DoS is given by $n(x,E) = \mathrm{Re}[\cosh\theta(x,E)]$, whereas the supercurrent reads

$$I_{\mathrm{S}}(\phi) = \frac{1}{2eR_{\mathrm{N}}}\int_{-\infty}^{\infty} dE\, j_{\mathrm{S}}(E,\phi) f_{\mathrm{L}}(E). \tag{2.39}$$

Here, ϕ is the order parameter phase difference, and R_{N} denotes the normal state resistance of the weak link with cross section A and length L. The quantity $j_{\mathrm{S}}(E,\phi) = \mathrm{Im}[j_{\mathrm{E}}]$ can be interpreted as a spectrum of the supercurrent-carrying states [77, 90, 118–120], and the distribution function $f_{\mathrm{L}}(E) = f(-E) - f(E) = \tanh(E/2k_{\mathrm{B}}T)$ describes their occupation.

For an SNS structure formed by a normal metal wire of length L between two S reservoirs, Eqs. (2.37) give the Thouless energy $E_{\mathrm{Th}} = \hbar D/L^2$ as the natural energy scale. It corresponds to the diffusion time across the junction. In a long diffusive SNS junction with $\Delta \gg E_{\mathrm{Th}}$, the critical current [maximum of $I_{\mathrm{S}}(\phi)$] can be approximated by the analytical expression [89, 121]

$$I_{\mathrm{c}} = \frac{64\pi}{3+2\sqrt{2}}\frac{k_{\mathrm{B}}T_{\mathrm{e}}}{eR_{\mathrm{N}}}\sqrt{\frac{2\pi k_{\mathrm{B}}T_{\mathrm{e}}}{E_{\mathrm{Th}}}}\exp\left[-\sqrt{\frac{2\pi k_{\mathrm{B}}T_{\mathrm{e}}}{E_{\mathrm{Th}}}}\right], \tag{2.40}$$

valid at $k_{\mathrm{B}}T_{\mathrm{e}} \gtrsim 3E_{\mathrm{Th}}$. According to the full numerical evaluation of I_{c}, in the limit of zero temperature it saturates to $I_{\mathrm{c}} = 10.82E_{\mathrm{Th}}/(eR_{\mathrm{N}})$. Here, $R_{\mathrm{N}} = L/(A\sigma_{\mathrm{N}})$ is the

normal state resistance of the weak link of length L, cross section A, and normal state conductivity σ_N. The diffusion constant D in the Thouless energy $E_\mathrm{Th} = \hbar D/L^2$ is related to the electrical conductivity via the Einstein relation $\sigma_\mathrm{N} = e^2\nu_\mathrm{F}D$ with ν_F denoting the normal state DoS at the Fermi energy. The exponential decay in Eq. (2.40) can be written as $\exp(-L/L_\mathrm{T})$, showing that the relevant length scale is the thermal coherence length. The form of Eq. (2.39) suggests several ways for controlling the observable supercurrent: Either the current-carrying states can be modified through $j_\mathrm{S}(E)$, or their occupation via the distribution function $f_L(E)$ [90, 120, 122, 123]. In this work, we control the electronic temperature T_e in the N part of a weak link by NIS refrigerators, thus realizing a cold-electron SNS transistor [124, 125].

Besides the supercurrent, another relevant quantity for this work is the thermal conductance of a piece of superconductor of length $l_\mathrm{S} = L_\mathrm{S}/\xi_0$ between two N reservoirs. It can be expressed in the general form [117, 126]

$$G_\mathrm{th} = \frac{G_\mathrm{N}}{2k_\mathrm{B}T^2e^2}\int_0^\infty dE E^2 M(E)\mathrm{sech}^2\left(\frac{E}{2k_\mathrm{B}T}\right), \tag{2.41}$$

valid for a general proximity circuit between the reservoirs. G_N denotes the normal-state electrical conductance, and the "heat transparency" $M(E) = l_\mathrm{S}^{-1}\int_0^{l_\mathrm{S}} dx\cos^{-2}[\mathrm{Im}\,\theta(x,E)]$ from the Usadel equations can be interpreted as a fraction of quasiparticles able to diffuse through the structure from one reservoir to the other, relative to the normal state. In a long superconducting wire with negligible inverse proximity effect, $M(E) = 0$ for $E < \Delta$ and $M(E) = 1$ for $E \gtrsim \Delta$. Equation (2.41) then simplifies to give the well-known exponential suppression of thermal conduction in superconductors [97, 127] relative to the normal-state Wiedemann-Franz value $G_\mathrm{th}^\mathrm{N} = \mathcal{L}_0 G_\mathrm{N} T$:

$$\gamma(T) = \frac{G_\mathrm{th}}{G_\mathrm{th}^\mathrm{N}} = \frac{3}{2\pi^2}\int_{\Delta/k_\mathrm{B}T}^\infty dx\frac{x^2}{\mathrm{sech}^2(x/2)} \simeq \frac{3}{2\pi^2}\left(8+8a+4a^2\right)e^{-a}. \tag{2.42}$$

Here, $\mathcal{L}_0 = \pi^2(k_\mathrm{B}/e)^2/3$ denotes the Lorenz number, $a = \Delta/k_\mathrm{B}T$, and the last approximation is valid for $a \gg 1$ (usable at $a \gtrsim 2$). Due to this strong violation of the Wiedemann-Franz law, transparent contacts to superconducting electrodes can thermally isolate a normal metal region or some other conductor to a very high degree, as long as the density of thermal quasiparticles is small, at $a \gg 1$.

Chapter 3

Experimental techniques

All the structures described in this work were fabricated by the standard micro- and nanofabrication methods of electron beam lithography (EBL) and shadow deposition of the thin metal films through a suspended resist mask [128] by electron-beam evaporation. They were subsequently electrically characterized at dilution refrigerator temperatures, typically in the range $50 - 500$ mK. In this chapter we briefly review the fabrication process and the measurement techniques.

3.1 Sample fabrication

The fabrication process is summarized in Fig. 3.1. The starting point is a 4 inch silicon (Si) [100] wafer, onto which a silicon oxide (SiO2) layer of typically 300 nm thickness has been grown by thermal oxidation. The suspended resist with the desired undercut profile is formed by utilizing two different polymers with differing sensitivities to high energy electrons in the beam of a scanning electron microscope. First, the wafer is covered by spin-coating it with a layer of copolymer (PMMA-MAA, polymethylmetacrylate-methacrylic acid) dissolved in ethyl lactate (EL) [129] (9-11%). In the end, the copolymer will act as a ballast or buffer layer. A spinning speed of $4000 - 6000$ RPM for $40 - 60$ s followed by baking on a hotplate at $170 - 180$ °C for 3 to 5 minutes typically results in a 500 nm thick layer. This is followed by applying in a similar manner at $2500 - 4000$ RPM a layer of PMMA (polymethylmethacrylate, also known as acrylic glass, of molecular weight 950000) in anisole (2-4%), with a resulting thickness of $100 - 150$ nm. Depending on the desired total thickness of the resist stack, the number of copolymer layers is typically varied from one to three. After the coating process, the wafer is diced into smaller chips, and a chip is loaded into the SEM for patterning by the tightly focused beam (typical diameter $1 - 2$ nm) of high energy electrons. For this purpose we utilized a Zeiss Supra 40 FE-SEM equipped with Raith GmbH Elphy Quantum lithography software and related beam blanker hardware, operating at acceleration voltages of $20 - 30$ kV. The beam is moved typically in steps of 10 nm (fine structures) to 200 nm (coarse structures, contact pads) across the chip, according to the desired pattern defined in a CAD file. The time spent at each spot is determined by the required exposure dose, usually $(1 - 6) \times 200\ \mu\mathrm{C/cm^2}$. The

high energy electrons break the long molecular chains in the (positive) polymer resists. As shown in Fig. 3.1 (b), the PMMA layer at the top is mainly sensitive to the incident electrons, resulting in a tightly defined pattern according to the design. On the other hand, the copolymer is more sensitive in itself, and also more sensitive to the slightly lower energy electrons backscattering from the substrate. As a result, the polymer chains are broken at large distances around the path where the beam was scanned. As indicated in Fig. 3.1 (c), the broken polymer chains can be selectively removed by utilizing a suitable solvent. For this development step, we employed a 1:3 weight mixture of MIBK:IPA (methyl isobutyl ketone : isopropanol), giving the suitable balance of sensitivity, speed and resolution. The chip is immersed into the developer for typically 20 s, followed by a rinse of 20 s in pure IPA and blow drying with nitrogen.

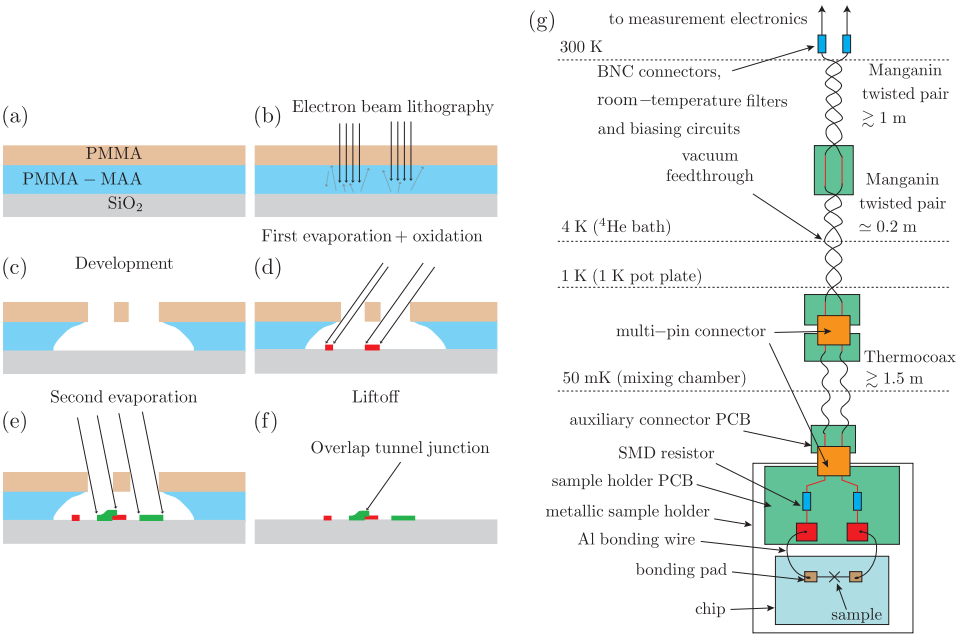

Figure 3.1: (a)–(f) Steps of the sample fabrication process based on a bilayer polymer resist, involving electron beam lithography and multi-angle shadow deposition of the metals. (g) Wiring scheme of the cryostat (not to scale). The green boxes with red lines represent PCBs.

The chip can then be loaded into the vacuum chamber of an (ultra) high-vacuum evaporator for the metallization step. This is based on heating a small, very pure metal target (typically 99.999% for Al and Cu) by a tight electron beam (acceleration voltage typically $4 - 10$ kV), to a high enough temperature for evaporation of the metal to occur. Depending on the material, this happens either after melting or directly by sublimation).

At typical base pressures of $10^{-6} - 10^{-8}$ mbar, the mean free path of the metal atoms is very long, and they can be thought in practise to travel to the chip in straight lines from the source, before sticking to the surface. This is illustrated in Fig. 3.1 (d). Note that if desired, the chip can be tilted to a large enough angle with respect to the evaporation source so that the metal ends up completely filling the narrow opening in the top PMMA layer, or hits only the side wall of the undercut 'cave' formed by the copolymer ballast layer. This provides additional control for the size of the resulting structures, and a means to avoid some of the many shadow copies if there are several angles.

The evaporated layers are typically $25 - 50$ nm thick. It is straightforward to modify the thickness in the range $10 - 200$ nm to obtain a conducting layer and have no trouble with the liftoff. Aluminum is used as the first layer in every tunnel junction, either of the NIS or SIS type, due to the easy formation of a high quality and stable surface oxide ($1 - 2$ nm thickness) layer by *in situ* thermal oxidation in the evaporator chamber: The barrier is created simply by exposing the chip to pure oxygen typically for $0.5 - 5$ min under a pressure of $0.5 - 10$ mbar. The T_C of our typical Al films is generally around 1.4 K, in contrast to the bulk value 1.2 K [3]. In very thin films, it can be increased close to 3 K [8].

After the Al has been oxidized, the desired counterelectrode (another Al layer for SIS; Cu, Ag, AuPd or similar normal metal for NIS junction) is deposited so that it partially overlaps the oxidized Al, as illustrated in Fig. 2.2. The junction overlap area is set by the desired normal state tunnel resistance R_T and the junction capacitance C. Depending on the oxidation pressure and time, the specific resistance for a good quality junction lies typically in the range $\mathcal{R}_0 \simeq 100\ \Omega\mu\text{m}^2 - 10\ \text{k}\Omega\mu\text{m}^2$. Below this, pinholes and other defects degrade the barrier quality. On the other hand, higher resistances require long oxidation times, high pressures and high temperatures. For AlOx as the dielectric, we have typically $C \simeq 50 - 100\ \text{fF}/\mu\text{m}^2$.

The multi-angle shadow evaporation combined with *in situ* oxidation has two very strong advantages which are utilized in the fabrication of almost all of the samples described in this work. First, all the critical structures are fabricated in a single vacuum cycle. Although this limits the shape and size of the electrodes and the choice of materials, the tunnel barriers will be of high quality with little contamination. Similarly, a clean, transparent contact between a normal and a superconducting metal with small interface resistance can be created by skipping the oxidation step, requiring no extra cleaning of the surfaces. This is important, for instance, for the observation of strong superconducting proximity effect in an N wire between two S reservoirs, central to publications **IV** and **VI** in this thesis. Moreover, different tunnel junctions and different kinds of direct metal-to-metal contacts can be combined to a single structure, allowing for example to utilize tunnel junctions to probe the proximity effect. A second advantage is the self-aligning nature of the shadow deposition process. The fabrication process is quick, as only one step of lithography is required. More importantly, small junction overlap areas with linear dimensions down to 20 nm (as well as gaps between metal layers evaporated at different angles) can be reliably created already with EBL of only moderate precision. This is because the evaporation angles and therefore the shifts between the various metal layers on the substrate can be adjusted accurately. The minimum reproducible overlap or gap size

is eventually limited by the grain size and uniformity of the evaporated films.

When all the required films have been deposited, the chip is unloaded from the evaporator. As the last step, the resist mask and the excess metal on top of it are removed in a lift-off process, with the result illustrated in Fig. 3.1 (f). The sample is immersed in a heated acetone bath (typically $50 - 60$ °C), to speed up the stripping away of the resist stack. Here, the undercut profile of the mask helps to create structures with clean edges: The metal film is broken between the substrate and the top of the resist, facilitating easy lift-off.

3.2 Low temperature electrical measurements

In this section we detail the general measurement procedure. All the measurements were performed at low temperatures in plastic $^3\mathrm{He}-^4\mathrm{He}$ dilution refrigerators [130] with a base temperature between $30-50$ mK [131]. The cryostats are operated in a 100 liter 4 inch neck liquid helium dewar, allowing for approximately 15 days of continuous stable operation. Samples can be rapidly characterized at millikelvin temperatures, as the time required from metal deposition to reaching the base temperature can be reduced to below eight hours. The cooling power at 100 mK is modest at approximately 50 μW, but adequate for low-frequency, low-power measurements.

After the fabrication process, the chip is diced into small enough pieces to be glued to a brass sample holder either by Dow Corning vacuum grease or GE varnish, to ensure good thermal contact while electrically insulating the substrate. The tunnel junctions or other structures are electrically connected by ultrasonic bonding with Al wire of 25 μm diameter (Delvotek 5332, deep-access wedge-wedge bonder). This makes a good contact between the bonding pads of typical diameter $150 - 250$ μm and the copper contacts on the sample holder printed circuit board (PCB). The holder has 12 pads which connect to 12 DC measurement lines in the cryostat. The cryostat wiring is illustrated in Fig. 3.1 (g). When a structure with the desired room temperature tunnel resistances has been located and bonded (verified by a digital multimeter), the sample holder is attached to the cryostat and enclosed within a threaded brass shield to reduce the influence of electrical noise at microwave frequencies from the 4.2 K environment. The holder is thermally anchored to the mixing chamber of the dilution refrigerator via a silver sinter and a silver rod, onto which it is tightly screwed and clamped. Temperature of the sample is measured by a ruthenium oxide resistor well thermalized with the sample stage assembly, connected to room temperature via four resistive leads formed by two twisted pairs. Its resistance varies exponentially from 1 kΩ at room temperature to approximately 50 kΩ at 50 mK. It is calibrated against a primary Coulomb Blockade Thermometer (CBT) [132], with the calibration accuracy of approximately 2%. The resistance was measured in a four point configuration either by a low frequency lock-in modulation technique, or by a separate resistance bridge. Temperature control of the sample holder (up to approximately 1 K, typically up to 500 mK) was achieved by applying a small current through a surface mount resistor glued to the sample stage assembly.

On the sample holder PCB, each measurement line contains a surface mount series

resistor of value $150 - 680\ \Omega$, typically $330\ \Omega$. These resistors, combined with the line and stray capacitance, form a low-pass RC filter for low-frequency inductively coupled noise. In contrast to NIS junctions, this is relevant for samples with fully superconducting Josephson junctions due to their low (zero) impedance at low frequencies in the supercurrent state. The sample holder is attached to the cryostat via a multi-pin connector. The lines continue as $1.5 - 2$ m long sections of Thermocoax coaxial cable up to the 1K plate in the cryostat (well thermalized to the small-volume pumped ^{4}He bath). These resistive (resistivity $\simeq 1\ \mu\Omega$m resulting in $\simeq 50\ \Omega$/m at room temperature, with NiCr inner wire, stainless steel outer conductor of 0.5 mm diameter, and magnesium oxide powder filling) coaxial cables act as efficient filters for high-frequency microwave noise [133], with more than 120 dB attenuation above $\gtrsim 1$ GHz. Approximately three quarters of the length of the Thermocoax wires is thermalized by silver epoxy to the mixing chamber of the dilution refrigerator, whereas the remaining quarter connects to the 1K plate via another multi-pin connector. From here the lines continue as resistive manganin twisted pairs out of the inner vacuum can (IVC) of the cryostat through a vacuum feedthrough into the main liquid helium bath at 4.2 K. After another connector PCB, the twisted pairs continue to a room temperature connector box with BNC connectors. Before connecting to the room temperature measurement electronics, additional low-pass filters were inserted at this stage when required. Due to the wiring capacitance, the measurement bandwidth of the lines is limited to approximately 10 kHz with high-impedance samples. With Josephson junctions, current pulses of length of a few hundred 100 μs with typically 10-20% rise times could be used without attenuation or distortion. In addition to being performed at low frequency, all the low-temperature measurements described in this work were done at low currents (typically below 10 μA), small enough not to cause heating in the resistive Thermocoax lines.

To DC voltage bias a structure with one or more junctions in series, we used either custom made, battery powered, floating voltage sources, Agilent 33220A function / arbitrary waveform generators, or Stanford Research Systems (SRS) SIM928 (with SIM900 mainframe) floating isolated voltage sources. To obtain the desired bias voltage $V \lesssim 1$ mV across the sample, these sources were combined with voltage dividers formed by resistive networks (typical division 1/1000). Constant current bias was obtained by replacing the voltage divider with a large room temperature bias (series) resistor $R_{\mathrm{bias}} \gg R_{\mathrm{S}}$, where R_{S} is the sample impedance at the desired current. In particular, the floating current bias of SINIS thermometers was formed by a battery (or a battery powered floating voltage source) connected to the sample via resistive voltage division and large series resistors.

Voltages across the samples were measured by room temperature, low-noise differential preamplifiers (HMS Elektronik Model 568, DL Instruments 1201, NF SA-400F3), and recorded by digital multimeters (Agilent 34410A and 34970A). The preamplified switching voltage pulses across Josephson junctions were either digitized at a sample rate of 50 kHz by a National Instruments PCI data-acquisition card, or counted by a Tektronix TDS3054B oscilloscope. Currents were measured by room temperature transimpedance preamplifiers (DL Instruments 1211, Femto LCA and DLPCA series). Between the battery-powered preamplifiers and recording devices, Burr-Brown 3650 isolation amplifiers were utilized to avoid galvanic coupling and therefore noise caused by ground

loops or originating from the measurement computers. Low-frequency lock-in measurements of mainly differential conductances were performed with SRS SR-830 DSP lock-in amplifiers. Data acquisition and instrument control were handled by a Matlab script over the GPIB IEEE-488 interface.

For applying a perpendicular magnetic field through the planar sample, a superconducting coil wound directly around the IVC or a separate coil was utilized, resulting at most to approximately 0.5 T/A. With maximum currents below 5 A, this is well sufficient to drive the thin Al films into normal state if required. In SQUID applications, the IVC and therefore the sample was enclosed by one to three magnetic shields made of mu-metal, reducing magnetic flux noise from external sources. Finally, application of a small parallel magnetic field was accomplished by a pair of room temperature Helmholtz coils around the dewar.

Chapter 4

Detecting non-Gaussian noise with a Josephson junction

In Sec. 2.2.2 we saw how the escape rate and the resulting escape probability of a hysteretic Josephson junction are very sensitive to changes in the bias current or the temperature, and that the junction dynamics are well understood. When the JJ is subjected to current fluctuations generated by another on-chip circuit element under study, one can envision to probe the fluctuations by monitoring their effect on the escape.

This chapter deals with the effects of shot noise on the escape rate of a hysteretic JJ, focusing on how the rate is affected by the non-Gaussian character of the noise, mainly a finite third moment. In **I** the problem was first theoretically analyzed assuming weak shot noise from a tunnel junction added to the bias current of the detector junction, so that it could be described in terms of an adiabatically averaged MQT escape rate. In **II** we report measurements at higher noise powers where an asymmetry of the escape rates was observed due to non-Gaussian noise. Further details are presented in **III**. Before summarizing the experiment, the following section is devoted to the characterization of possibly non-Gaussian electrical fluctuations in general.

4.1 Noise in mesoscopic physics

In all conductors, the current $I(t) = \langle I(t) \rangle + \delta I(t)$ always fluctuates in time even in a perfect experimental setup: random variations $\delta I(t)$ are present around the average value $\langle I(t) \rangle$ due to the discrete nature of the charge carriers and their thermal motion. Here and in the following the angle brackets denote statistical averaging. The fluctuations are completely characterized once the general time-dependent correlation functions

$$M_n(t_1, \ldots, t_n) = \left\langle \prod_{i=1,n} \delta I(t_i) \right\rangle \tag{4.1}$$

are known. We limit to stationary processes where the average current $\langle I \rangle$ does not change with time and the correlation functions do not depend on absolute time. These quantities

can then be expressed in terms of their Fourier transforms

$$\tilde{S}_I^{(n)}(\omega_1, \omega_2 \ldots, \omega_n) = \int_{-\infty}^{\infty} dt_1 \int_{-\infty}^{\infty} dt_2 \ldots \int_{-\infty}^{\infty} dt_n M_n(t_1, \ldots, t_n)$$
$$= 2\pi\delta(\omega_1 + \omega_2 + \ldots + \omega_n) S_I^{(n)}(\omega_1, \omega_2, \ldots, \omega_{n-1}), \qquad (4.2)$$

defining the frequency-dependent spectral densities $S_I^{(n)}$, the simplest of these being the 2nd order spectral density or noise power:

$$\langle \delta I(t_1)\delta I(t_2)\rangle = \int_{-\infty}^{\infty} \frac{d\omega}{2\pi} e^{-i\omega(t_1-t_2)} S_I^{(2)}(\omega), \quad \text{or} \quad S_I^{(2)}(\omega) = \int_{-\infty}^{\infty} dt e^{i\omega t} \langle \delta I(t)\delta I(0)\rangle. \qquad (4.3)$$

The above correlation functions can be generalized to hold for averages of quantum mechanical current operators, but then for $n \geq 2$ the correct ordering of the time instants t_1 depends on how the noise is measured [134]. The observable frequency dependence is affected by both the internal dynamics of the system (for instance on the scale of eV/h, or that set by a diffusion time through the system) as well as the circuit between the noise source and the detector (filter frequency response).

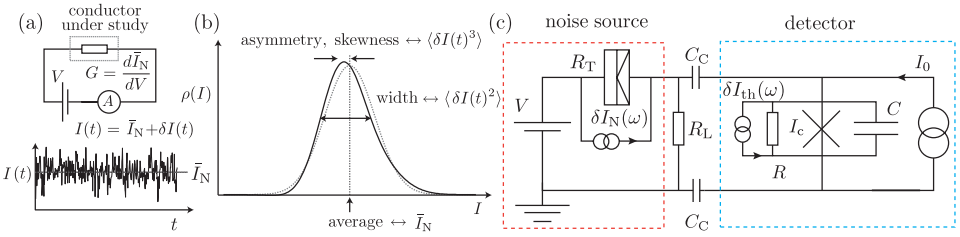

Figure 4.1: (a) In voltage-biased mesoscopic conductors the current fluctuates in time around the average current due to nonequilibrium shot noise. (b) The distribution of the fluctuations (black) can be characterized in terms of the central moments $\langle \delta I^n \rangle$. A finite third moment indicates an asymmetry around the mean value, in contrast to a Gaussian distribution (gray). For positive $\langle \delta I^3 \rangle$, the distribution is skewed towards values above the average. (c) Example of on-chip coupling of shot noise to a current-biased Josephson junction.

Substantial amount of information about the noise $\delta I(t)$ is contained in the equal-time central moments $\langle \delta I^n \rangle = \langle \delta I(t)^n \rangle$, which are defined in terms of the probability distribution $\rho(I)$ of the instantaneous current as $\langle \delta I^n \rangle = \int_{-\infty}^{\infty} dI (I - \langle I \rangle)^n \rho(I)$. Knowing all the moments specifies $\rho(I)$ uniquely. Alternatively, one can define the characteristic function $\phi(k)$ as the Fourier transform of $\rho(I)$ and its expansion in the cumulants C_n:

$$\phi(k) = \int_{-\infty}^{\infty} dI e^{ikI} \rho(I), \quad \ln \phi(k) = \sum_{n=1}^{\infty} \frac{(ik)^n}{n!} C_n, \qquad (4.4)$$

where the cumulants are related to the central moments as $C_1 = \langle I \rangle$, $C_2 = \langle \delta I^2 \rangle$, $C_3 = \langle \delta I^3 \rangle$, $C_4 = \langle \delta I^4 \rangle - 3\langle \delta I^2 \rangle^2$, $C_5 = \langle \delta I^5 \rangle - 10\langle \delta I^2 \rangle \langle \delta I^3 \rangle$, and so on. Figure 4.1 (b) sketches

how the shape of distribution $\rho(I)$ is determined not only by the variance $\langle \delta I^2 \rangle$, but also by the higher cumulants. A special case is a Gaussian distribution for which only the first two cumulants are non-zero, as can be seen from Eq. (4.4).

In the last two decades, study of noise properties of various conductors has been one of the most active branches of theoretical mesoscopic physics, in particular after the framework of full counting statistics (FCS) was established [135, 136]. It considers the probability distribution $P(N,t)$ for N charges having passed through the conductor during the counting time t. It allows in principle an exact calculation of the characteristic function and therefore all the cumulants of the charge number N, which are related to the zero-frequency limits of the current noise spectral densities in Eq. (4.2) for long t. The finite-frequency correlators can be calculated with extended FCS methods based on path integrals [137].

The interest in the noise statistics stems largely from the extra information about the charge transfer process contained in the full probability distribution. Considering the voltage-biased system of Fig. 4.1 (a), equilibrium current noise with the noise power $S^{(2)}_{\mathrm{I,eq}}(\omega) = \hbar\omega \mathrm{Re}[Y(\omega)][\coth(\hbar\omega/(2k_\mathrm{B}T)) + 1]$ is always present. Here, $Y(\omega) = Z^{-1}(\omega)$ is the frequency-dependent admittance of the conductor, which reduces to the constant $1/R$ for an ohmic resistor. However, at finite V another contribution appears in the total observable current noise: $S^{(2)}_{\mathrm{I,tot}}(\omega) = S^{(2)}_{\mathrm{I,eq}}(\omega) + S^{(2)}_{\mathrm{I,shot}}(\omega)$, where $S^{(2)}_{\mathrm{I,shot}}(\omega)$ describes the nonequilibrium *shot noise* in the system due to the discreteness of the charge carriers and their finite transmission probability through the system under study [4]. Besides the equilibrium and shot noise, in various systems yet another contribution is present, often dominating at low frequencies. However, the origin of this so-called $1/f$ noise with spectral density typically $\propto 1/\omega$ does not appear to be universal [6, 138, 139]. The on-chip noise detection scheme considered in this work is not sensitive to $1/f$ noise due to the high frequency scale set by the detector junction plasma frequency.

At $eV \gg k_\mathrm{B}T$, the shot noise power in the zero-frequency limit is simply proportional to the average current $\bar{I} = \langle I \rangle$ though the system: $S^{(2)}_{\mathrm{I,shot}}(0) = F_2 e|\bar{I}|$, where $F_2 = \sum_i T_i(1-T_i)/\sum_i T_i$ is the second-order Fano factor depending on the transmission probabilities T_i of the individual conduction channels of the system [4, 140]. The relevant third-order correlator has the universal form $S^{(3)}_{\mathrm{I,shot}}(0,0) = F_3 e^2 \bar{I}$ with $F_3 = \sum_i T_i(1-T_i)(1-2T_i)/\sum_i T_i$ and the higher-order ones can be expressed as $F_n e^{n-1}|\bar{I}|\mathrm{sign}(\bar{I})^n$. Notably, the odd cumulants change sign when $\bar{I}$ is inverted whereas the even-n quantities are symmetric in $\bar{I}$. The fingerprint of the underlying process of charge transfer is also evident in the Fano factors F_n. For example, in a tunnel junction all $T_i \ll 1$, and instants of the individual tunneling events are uncorrelated. The current noise then follows the Poisson distribution, and $F_n = 1$ for all n. In general, observability of the non-Gaussian, intrinsically nonequilibrium shot noise requires weak inelastic scattering of the charge carriers, explaining why it is present in mesoscopic systems but absent in macroscopic resistors.

Higher-order current statistics have been calculated for numerous systems such as tunnel junctions, diffusive wires, double-barrier junctions, and chaotic cavities, whereas the predictions have been so far tested only in a limited number of experiments and usually in the limit of low frequencies compared to the intrinsic time scales. This is in contrast

to various experiments probing the intrinsic frequency-dependence of the second-order spectral density, e.g., in a quantum point contact (QPC) [141].

In the first pioneering measurement the third moment of shot noise of a tunnel junction was measured using traditional microwave techniques [142], showing the strong influence of the circuit feedback effects on the observable higher-order correlators for matched sample and circuit impedances [143]. Consequently, the weak third-order effects have been probed in tunnel junctions with higher impedance [144] and in a QPC [145]. Measurements of this type are restricted to a relatively narrow band of frequencies, and require very long averaging times. Therefore, the recent tendency has been to look for well-characterized mesoscopic systems with an intrinsic amplification mechanism that could be used as on-chip, wide-band noise detectors: The shot noise produced by the conductor under study is coupled to a detector whose response is monitored. At low frequencies, the distribution function has been probed even beyond the fifth cumulant by direct counting of the tunneling electrons in a coupled system of a quantum dot noise source and a QPC detector. A promising approach at higher frequencies for probing the spectral densities even beyond the second-order noise power is to measure the induced transition rates in a two-level quantum system (qubit) [27, 146, 147]. The nonequilibrium noise has also been predicted [148, 149] and demonstrated [150, 151] to affect the qp- or supercurrent in tunnel junctions.

In line with these developments, the switching rate of a Josephson threshold detector was considered as a probe of the full characteristic function [152], or limiting to the third cumulant [153]. The measurement principle is sketched in Fig. 4.1 (c): The noise source is a tunnel junction with resistance R_{T}, biased by the voltage V. The current fluctuations δI_{N} can couple to the bias current I_0 of the JJ detector, and the escape rate is probed as discussed in Sec. 2.2.3. The average current $\bar{I} = V/R_{\mathrm{T}}$ in the noise source flows through the resistance R_{L} instead of passing to the detector, so that the DC biasing of the source and the detector can be controlled independently. Finite odd cumulants of δI cause a difference in the escape rates when V is inverted.

For hysteretic JJs in the quantum limit $\hbar\omega_{\mathrm{p}} \gg k_{\mathrm{B}}T$, the sensitivity to the second moment of shot noise from another tunnel junction was demonstrated in [54]. The escape is described in terms of thermal activation at an effective temperature T_{eff}, which can exceed even T_{C}. In the subsequent experiments an escape rate asymmetry due to the non-Gaussian nature of the noise was observed (see **II** and **III**). Importantly, the same features have been observed also for junctions in the classical regime $\hbar\omega_{\mathrm{p}} \ll k_{\mathrm{B}}T$ [154–156]. In this limit, a detailed theory for the third-order rate asymmetry due to shot noise has been developed [157–159]. It is valid for all strengths of the dissipation Q [157], and has been extended to include circuit feedback effects [160]. The problem of escape in a JJ subjected to non-Gaussian fluctuations was considered also in [161, 162]. The decay of metastable states induced by non-Gaussian noise has been recently analyzed in other settings as well, not limited to JJ detection [163, 164].

4.2 Escape rate in the presence of shot noise

With the TA and MQT escape rates of Sec. 2.2.2 at hand, how can the influence of added non-Gaussian noise on the escape be understood in qualitative terms? This "external" noise corresponds to the random force term $\eta(t)$ in Eq. (2.7). For an alternative view, one can define a time-dependent effective potential $U_{\rm eff}(\varphi,t) = U(\varphi) - \varphi\eta(t)$ [158]. The effect of the added noise depends on the range of frequencies f involved. The most relevant frequency scales of the problem are shown in Fig. 4.2. As indicated on the left side, for $\Delta t^{-1} \lesssim f \lesssim \omega_{\rm p}/(2\pi)$ the potential varies quasi-stationarily (compared to the phase dynamics at $\omega_{\rm p}$) the tilt of the potential around the average tilt set by I_0. The observable escape rate during a pulse of length Δt in Eq. (2.17) is then the "intrinsic" rate (MQT or TA), averaged over the distribution $\rho(I)$ of the shot noise [53]: $P = 1 - \exp(-\langle\Gamma\rangle\Delta t)$. Neglecting the I_0-dependence of the prefactor A to the MQT or TA rate $\Gamma(I) = A\exp(-B)$, the rate at the instantaneous current $I_0 + \delta I$ can be approximated by $\Gamma(I_0 + \delta I) \simeq \Gamma(I_0)\exp[-(\partial B/\partial I)\delta I]$. Here, the derivative of the exponential activation factor B is evaluated at I_0. Making a cumulant expansion up to the third order, the averaged rate can be approximated by (see **I**)

$$\langle\Gamma\rangle \simeq \Gamma(I_0)\exp\left[\frac{1}{2}\left(\frac{\partial B}{\partial I}\right)^2\langle\delta I^2\rangle - \frac{1}{6}\left(\frac{\partial B}{\partial I}\right)^3\langle\delta I^3\rangle\right]. \tag{4.5}$$

Here, $\langle\delta I^2\rangle \simeq (\Delta\omega_2/2\pi)eF_2|\bar{I}_{\rm N}|$ and $\langle\delta I^3\rangle \simeq (\Delta\omega_3/2\pi)^2e^2F_3\bar{I}_{\rm N}$ are the second and third moment of the added shot noise with the effective bandwidths $(\Delta\omega_2/2\pi)$ and $(\Delta\omega_3/2\pi)$. To quantify the rate difference for opposite signs of the third moment we consider the quantities $\langle\Gamma^{\pm}\rangle$, obtained from Eq. (4.5) with positive or negative $\langle\delta I^3\rangle$. The difference in the rates $\langle\Gamma^{\pm}\rangle$ due to the third cumulant can then be measured by monitoring the shift in the $I_{0.5}$-point upon inverting $\bar{I}_{\rm N}$, or as a change in the escape probability at fixed I_0.

In the classical limit $\hbar\omega_{\rm p} \ll k_{\rm B}T$ the added noise at higher frequencies $f \gg \omega_{\rm p}/(2\pi)$ appears white on the scale of $\omega_{\rm p}$, so that the detector junction probes the low-frequency limit of the spectral densities in an effective, averaged potential. This time scale separation forms the starting point of the classical models [157–159]. The second moment gives rise to an effective escape temperature, and the third moment causes an asymmetry of the rate depending on its sign. The rate can be obtained from the FPE in Eq. (2.10) after averaging over the fluctuations and making a cumulant expansion [158], or using path integral methods [157, 159].

On the other hand, the classical models are not rigorously applicable for small-capacitance detector junctions with $\hbar\omega_{\rm p} \gg k_{\rm B}T$, studied in [54] as well as **II** and **III**. A full theory describing the transition from MQT to classical escape in the presence of nonequilibrium noise has not yet been developed, as already a description of thermally assisted quantum tunneling is difficult. In a first approximation, in the low-T limit shot noise affects the transition rate $\gamma_{m,n}$ from level n at E_n to level m at E_m in the metastable well, and therefore also the escape rate. Treating the current fluctuation δI in Eq. (2.13) as a small perturbation, in second-order perturbation theory the rates are approximated by [165]

$$\gamma_{m,n} = |M_{m,n}|^2 S_{\rm I,tot}(\omega_{m,n}) \tag{4.6}$$

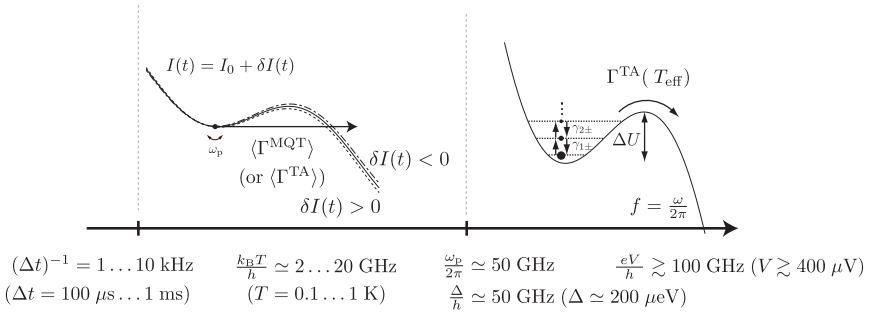

Figure 4.2: Characteristic frequencies for the detection of noise with a JJ. The intrinsic high-frequency cutoff of the shot noise from a voltage-biased tunnel junction occurs at eV/h. Weak fluctuations in the frequency range $\Delta t^{-1} \lesssim f \lesssim \omega_p/(2\pi)$ lead to quasi-stationary tilting of the potential around the average tilt, leading to an averaged, enhanced escape rate out of the well by MQT or by TA. Stronger noise at $f \simeq \omega_p/(2\pi)$ affects the transition rates between the metastable energy levels in the well. The escape happens by TA at an effective temperature T_{eff} that depends mainly on the second moment of the fluctuations. Effect of the non-Gaussian character of the noise on the transition rates is predicted to be small at these frequencies.

with the level spacing $\omega_{m,n} = (E_m - E_n)/\hbar$. $M_{m,n} = \langle m| - \hbar\hat{\varphi}/(2e)|n\rangle$ is the matrix element of the $\hat{\varphi}$-operator coupling to the current noise with the total spectral density $S_{I,tot}(\omega) = S_{I,env}(\omega) + S_{I,shot}(\omega)$. Here, $S_{I,env}(\omega)$ is the equilibrium current noise spectral density, and $S_{I,shot}(\omega) = eF_2^{eff}|\bar{I}_N|$ describes the shot noise contribution. The effective second-order Fano-factor $F_2^{eff} = F_2 G(\omega)G(-\omega)$ includes the factor $G(\omega)$ that relates the intrinsic fluctuation $\delta I_N(\omega)$ at the noise source to $\delta I(\omega) = G(\omega)\delta I_N(\omega)$ at the detector. Equation (4.6) shows how relaxation is determined by the spectral density at positive and excitation at negative frequencies, respectively. As shown in [54], the shot noise contribution to the level dynamics can be described in terms of an effective temperature

$$T_{eff} \simeq \hbar\omega_p/2\mathrm{arcoth}\left[1 + \frac{QF_2^{eff}e|\bar{I}_N|}{\hbar\omega_p^2 C}\right] = \hbar\omega_p/2k_B\mathrm{arcoth}\left[1 + \frac{QF_2^{eff}|\bar{I}_N|}{2I_c[1-(I_0/I_c)^2]^{1/2}}\right], \quad (4.7)$$

and for $T_{eff} \gg T_{cr}$ the escape rate with shot noise is approximated simply by Eq. (2.12) with $T = T_{eff}$. The dominant transitions occur between neighboring levels, and the potential was approximated by a harmonic well. In Eq. (4.7), the quality factor is given by $Q = \omega_p C/\mathrm{Re}[Y(\omega_p)]$. At large currents $|\bar{I}_N| \gg \hbar\omega_p^2 C/(eQF_2^{eff})$ the result reduces to $k_B T_{eff} \simeq e|\bar{I}_N|RF_2^{eff}/2$ with $R = \mathrm{Re}[Y(\omega_p)]^{-1}$, coinciding with the classical escape temperature with $T = 0$.

To include the effect of the higher moments of shot noise, the perturbation theory leading to Eq. (4.6) can be carried further to higher orders [147, 166]. However, the third-cumulant-induced corrections to the transition rates vanish in a harmonic potential and in case of frequency-independent third-order spectral densities. We therefore include the

effect of the third cumulant on the escape rate only in terms of the averaging via Eq. (4.5): The dominant effect of the shot noise is the strongly enhanced escape temperature $T_{\rm eff} \gg T$, included in the TA rate $\Gamma(I_0)$ with the exponential activation factor $B = \Delta U/(k_{\rm B}T_{\rm eff})$. The lower-frequency third-order fluctuations then lead to a slow modulation of this rate, described by Eq (4.5). Notably, the third-order asymmetry can be distinguished upon inverting the direction of $\bar{I}_{\rm N}$, whereas the low-frequency second-order contribution cannot typically be reliably separated due to uncertainty in the junction parameters. In summary, within this hybrid description of the second and third order effects, the observable rate $\langle\Gamma\rangle$ is given by Eq. (4.5) with $B = \Delta U/(k_{\rm B}T_{\rm eff})$.

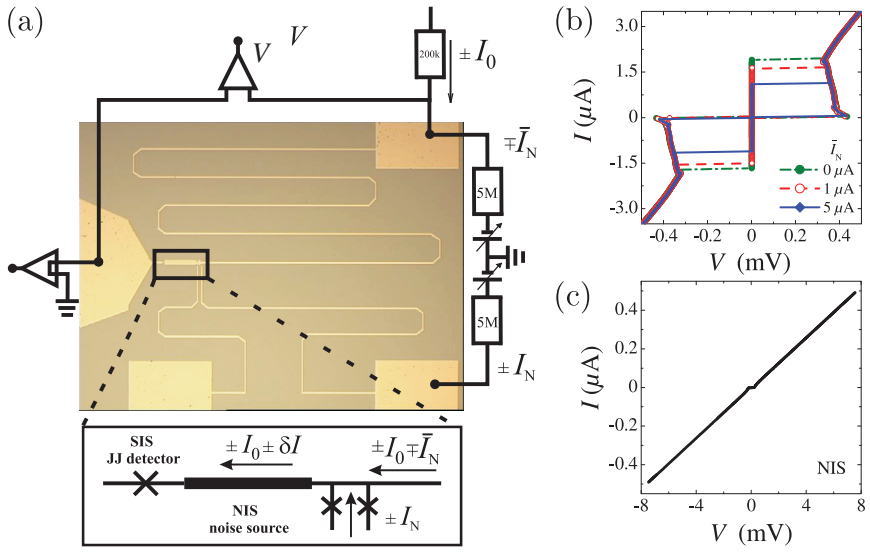

Figure 4.3: (a) Optical microscope image of one of the studied samples, together with the measurement scheme. The shot noise of a voltage biased NIS junction is coupled to the detector JJ separated from the noise source physically by $\gtrsim 100$ μm. The average current $\bar{I}_{\rm N}$ through the NIS junction is accurately balanced through an additional superconducting line, so that relative polarities of the detector and source currents I_0 and $\bar{I}_{\rm N}$ can be changed independently. This sample contained two NIS junctions, with only one of them connected to the biasing circuit at all times. (b),(c) IV characteristics of the detector and source junctions. The detector IVs are shown at various values of $\bar{I}_{\rm N}$ through the noise source.

4.3 Measurement of the escape rate asymmetry

Figure 4.3 (a) displays an optical microscope image of one of the measured samples analyzed in **II** and **III**. The structure contains an SIS detector junction coupled to an on-chip NIS noise source approximately 100 μm apart. Instead of the capacitive coupling scheme

of Fig. 4.1 (c), the detector and the shot noise source are coupled directly by the superconducting line. Both junctions can then be fabricated in a one-step process, but the DC component $\bar{I}_N$ of current through the noise source has to be accurately balanced via an additional superconducting line. The high frequency noise δI passes preferably through the detector JJ due to the $\gtrsim 10$ μm wide contact lead and the large shunt capacitance to ground, whereas the long and narrow ($\simeq 2$ μm) biasing lines present a higher impedance. IV characteristics of the detector and the source are shown in Fig. 4.3 (b) and (c), respectively. The NIS source is operated deep in the linear regime. The suppression of the switching current with increasing $\bar{I}_N$ can be distinguished already in the detector IVs, but the third-order asymmetry is visible only in the escape probability histograms. Importantly, no gap suppression in the detector is observed, indicating no excessive direct Joule heating by the large current $\bar{I}_N$. The escape in the detector at each I_0 and $\bar{I}_N$ is probed by sending typically $10^3 - 10^4$ current pulses and counting the arising voltage pulses. As indicated in Fig. 4.3 (a), the polarities of the detector bias current I_0 and the average current $\bar{I}_N$ through the noise source can be varied independently. When they are both positive or negative ($++$, $--$), the asymmetric shot noise with positive third cumulant is expected to "add" to the detector bias current thus increasing the escape rate. In the two remaining cases ($+-$, $-+$) the rate is correspondingly reduced compared to the case of Gaussian noise.

A set of measured histograms at different magnitudes of $\bar{I}_N$ and different bias current polarity combinations is shown in Fig. 4.4 (a). The second moment effect dominates through the increased T_{eff}, resulting in a considerable shift of the position $I_{0.5}$. However, also a small shift between the two non-equivalent sets of polarity combinations appears at finite $\bar{I}_N$ due to the third moment. The extracted histogram positions, widths, and the asymmetry are shown in Fig. 4.4 (b), (c), and (d), respectively, together with a fit from the effective temperature model with $I_c = 2.83$ μA, $C = 90$ fF, $RF_2^{\mathrm{eff}} = 75$ Ω, and $\Delta\omega_3 = 0.83\omega_p$. The agreement is satisfactory considering the crudeness of the model, and the bandwidth $\Delta\omega_3$ obtains a reasonable value.

In summary, we have observed that the lifetime of the supercurrent state in an underdamped JJ is sensitive to shot noise added to the average bias current. The main effect is described by an elevated escape temperature due to the second moment. An escape rate asymmetry develops due to finite odd moments of the fluctuations, which was detected by reversing the relative polarities of the detector and source biases. Besides showing the feasibility of on-chip detection of fluctuations, the experiments and theoretical modeling with non-Gaussian noise result in a deeper understanding and further validation of the basic models of junction dynamics.

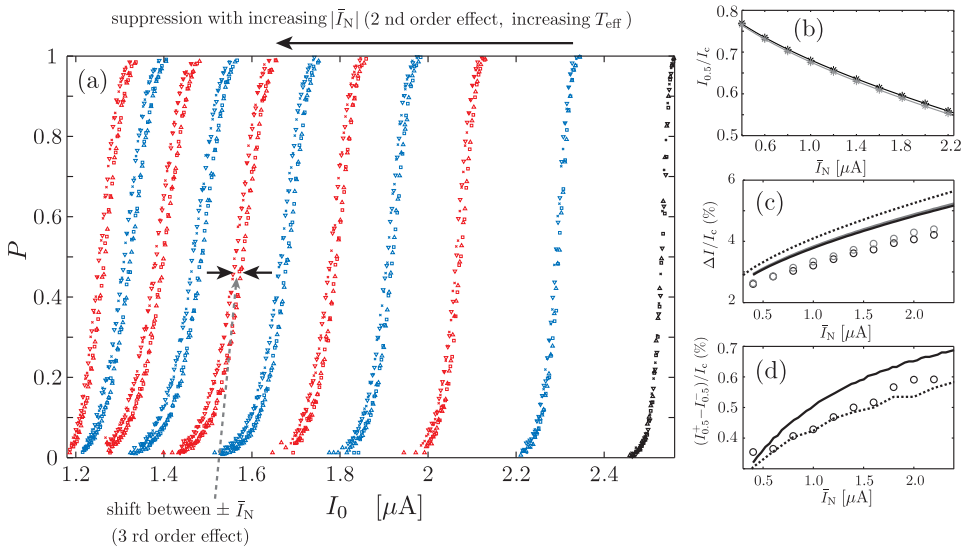

Figure 4.4: (a) Set of measured histograms in the presence of shot noise. The down triangle and cross correspond to the equivalent polarity combinations ++ and −−, whereas the up triangle and the square represent +−, −+. (b)–(d) Histogram positions, widths, and asymmetries at $P = 0.5$ as a function of the magnitude of $\bar{I}_N$ (symbols), compared to Eq. (4.5) with $B = \Delta U/(k_B T_{eff})$ (solid lines). The dotted lines from **II** use T_{eff} extracted from the measurement. The measured quantities are averaged over the two equivalent polarity combinations.

Chapter 5

Origin of hysteresis in a weak SNS link

This chapter deals with the experiments on Superconductor – Normal metal – Superconductor (SNS) Josephson junctions reported in **IV** and **V**. As discussed in Sec. 2.2.1, the dynamics of several types of weak links between two superconducting electrodes can be described in terms of the RCSJ model. In overlap-type SIS tunnel junctions, such as the detector JJ in the sample of Fig. 4.3 (a), the quality factor $Q \geq 1/\sqrt{2}$ due to the large junction capacitance C. The IV characteristic is hysteretic because of the underdamped phase dynamics: after switching to the resistive state upon an increase of the bias current above a certain value $I_{\rm sw} \lesssim I_{\rm c}$, the junction returns to the supercurrent state only when the bias is reduced past a retrapping current $I_{\rm r} \ll I_{\rm switch}$. In lateral weak links, such as metallic proximity SNS junctions, the geometric capacitance between the junction electrodes is small, and $Q \ll 1$ and a nonhysteretic IV characteristic similar to Fig. 2.3 (b) are expected. Somewhat surprisingly, hysteretic behavior is routinely observed in various kinds of lateral weak links between two S electrodes, including normal metals [167], superconducting [168] and semiconducting nanowires [169, 170], carbon nanotubes [171, 172], and graphene [173]. Initially, hysteresis was observed in superconducting microbridges and constriction-type junctions [174], and explained in terms of heating by formation of local hot spots within the link [175]. Alternatively, the observations have been explained in terms of replacing C by an effective capacitance $C_{\rm eff}$, giving $Q > 1$. For a diffusive weak link of normal state resistance $R_{\rm N}$, capacitance C, diffusion constant D, and length L, the damping time $R_{\rm N}C$ has been proposed to be replaced by a time scale $\hbar/\Delta$ related to the superconductor energy gap Δ [176], or to the electron diffusion time $\tau_{\rm D} = \hbar/E_{\rm Th} = L^2/D$ across the junction [167].

5.1 Thermal balance of an SNS junction

In **IV**, we show the hysteresis in metallic SNS junctions to be related to the overheating of the normal metal electrons once the junction switches to the resistive state. Direct evidence of the overheating is provided by integrating a SINIS thermometer to the N

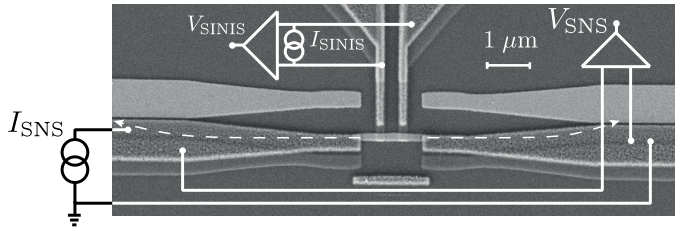

Figure 5.1: SNS weak link (horizontal) with two superconducting probes weakly tunnel coupled to the N island (from the top). When operated as a SINIS thermometer, the two tunnel junctions are series biased by a small constant current $I_{\mathrm{SINIS}} \ll \Delta/(eR_{\mathrm{T}})$ provided by a floating battery powered current source. I_{SINIS} is chosen to be higher than the small supercurrent through the SINIS junction due to the proximity effect on the N island. The voltage V_{SINIS} is a sensitive probe of the electronic temperature of the N electrode after calibration against the bath (phonon) temperature T_{bath}, and reflects strongly any heating caused by the Joule power $P_{\mathrm{SNS}} = I_{\mathrm{SNS}}V_{\mathrm{SNS}}$ deposited in the SNS junction. In comparison, the voltage drop due to the bias current I_{SNS} and the finite normal state resistance $\simeq 2\ \Omega$ of the part of the N island between the NIS probes is orders of magnitude smaller. The dashed arrows indicate the path of heat conduction from the N island to the normal metal shadow copies partially overlapping the S electrodes. Quasiparticle heat conduction from the island to these N reservoirs is the dominating channel in determining the rise of the island temperature in response to an injected power P_{SNS}.

island of the weak link. A typical structure fabricated by three-angle shadow evaporation is shown in Fig. 5.1, together with the measurement scheme. A Cu island of thickness $d_{\mathrm{N}} \simeq 30$ nm and of the indicated non-overlapped length $L \simeq 1.5\ \mu$m is contacted by two transparent metal-to metal NS contacts to two superconducting Al electrodes of thickness $d_{\mathrm{S}} \simeq 70$ nm. Between the transparent NS contacts, the N island contacted via opaque AlOx tunnel barriers to two additional Al electrodes. The V_{SNS} vs. I_{SNS} -characteristic of the SNS junction with $R_{\mathrm{N}} \lesssim 10\ \Omega$ is measured in a four-point configuration, and the two NIS tunnel junctions with total normal state tunneling resistance $R_{\mathrm{T}} \gtrsim 20\ \mathrm{k}\Omega$ in the middle are operated as a current biased thermometer as discussed in Sec. 2.3. Several structures of varying L were measured, with data from three samples included in **IV**.

The main result of the experiment is summarized in Fig. 5.2, displaying the simultaneously measured $I_{\mathrm{SNS}}V_{\mathrm{SNS}}$ -characteristic and the electron temperature T_{e} from the SINIS thermometer voltage V_{SINIS} of sample 2 of **IV**at four values of T_{bath}. As expected, the $I_{\mathrm{SNS}}V_{\mathrm{SNS}}$ -characteristic is asymmetric in I_{SNS}, whereas the thermometer signal is symmetric. The arrows indicate the direction of the switching and retrapping events upon increasing or decreasing of the bias current I_{SNS}. As I_{SNS} is increased from zero, the junction remains initially in the dissipationless state, and $T_{\mathrm{e}} \simeq T_{\mathrm{bath}}$. However, at $I_{\mathrm{SNS}} = I_{\mathrm{switch}} \lesssim I_{\mathrm{c}}$, it switches abruptly to a resistive state with T_{e} saturating around 400 mK for this sample. When I_{SNS} is again decreased, T_{e} decreases slowly until a certain retrapping current I_{r}, when the system returns to the supercurrent state.

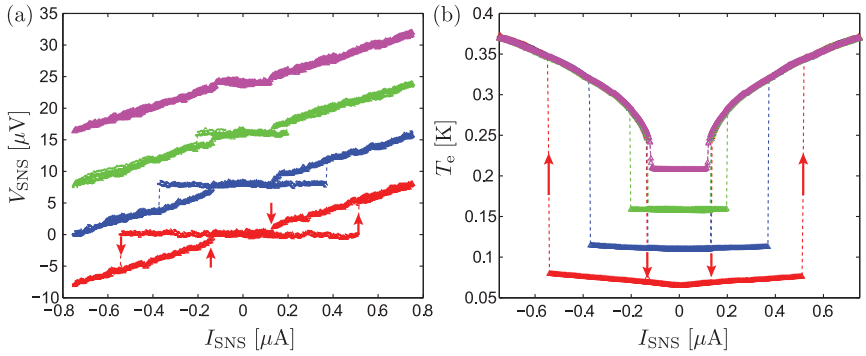

Figure 5.2: (a) Simultaneously measured $I_{SNS}V_{SNS}$ characteristic and (b) the N island temperature T_e inferred from the SINIS thermometer voltage V_{SINIS}, as a function of the bias current I_{SNS}. The data are from sample 2 of **IV**, with $L \simeq 1.5$ μm and $R_N \simeq 10\,\Omega$. The different curves correspond to four different bath temperatures T_{bath}, with the curves in (a) shifted vertically by 8 μV for clarity. The arrows indicate the switching and retrapping currents I_{switch} and I_r at the lowest T_{bath}, observed as discontinuous jumps. The T_e-signal displays corresponding discontinuities.

Figures 5.3 (a) and (b) show the T_{bath}- and T_e-dependence of the measured switching and retrapping currents for the same sample. I_{switch} follows the the exponential decrease described by Eq. (2.40). Notably, the saturation of I_r at low T_{bath} in the hysteretic regime corresponds to a saturation of T_e at the point of retrapping: the I_r-line in Fig. 5.3 (a) collapses close to a single point in (b). The onset of saturation in I_{switch} in some of the other samples [see Fig. 5.6] is similarly caused by leveling out of T_e. In the nonhysteretic regime, thermal smearing complicates the experimental determination of the true I_c, as the ratio $E_J(T_e)/(k_B T_{bath})$ becomes smaller. The solid line in Fig. 5.3 (b) is obtained from Eq. (2.40) with $R_N = 10\ \Omega$ and $E_{Th} = 2.1$ μeV. These values are in reasonable agreement with the geometry of the sample and the estimated normal state resistivity. However, the result has to be multiplied by a phenomenological reduction factor α, with typical values close to 0.5 for our structures. This constant can differ from unity, e.g., because the overlap geometry deviates from an ideal 1D junction, and because the switching occurs before the critical current is reached. The retrapping current at low T_{bath} is close to (but slightly above) I_{switch} at the value of T_e at $I_{SNS} = I_r$, indicating that a quasiequilibrium description in terms of an electronic temperature is valid at the small voltages involved. Finite-voltage behavior and nonequilibrium effects in SNS and SNS-NIS structures have been analyzed in [96, 177, 178].

In the simplest picture, the value of T_e after the switching is determined by the balance of the Joule heating power $P_{SNS} = I_{SNS}V_{SNS}$ and the power flow $P_{e-ph} = \Sigma_N\Omega_N(T_e^5 - T_{bath}^5) \simeq \Sigma_N\Omega_N T_e^5$ from the N island electrons to N phonons at T_{bath}. In Fig. 5.3 (c), the symbols show the measured power P_{SNS} at $T_{bath} = 50$ mK against the inverse of the measured T_e. The dotted lines indicate $T_e = (P_{SNS}/\Sigma_N\Omega_N)^{1/5}$ taking into account

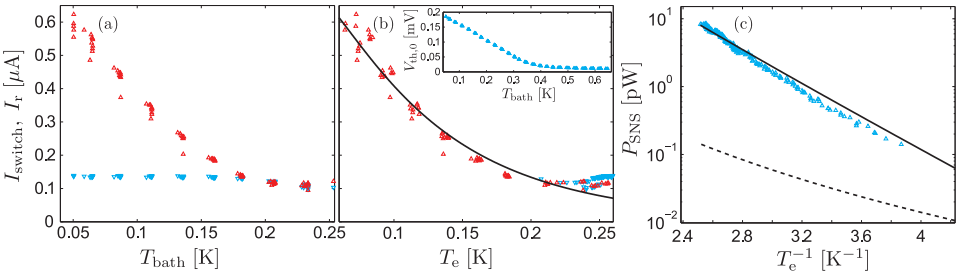

Figure 5.3: Measured switching (red symbols) and retrapping (blue symbols) currents of sample 2 as a function of $T_{\rm bath}$ and $T_{\rm e}$ in (a) and (b), respectively. The black line in (b) shows the prediction of Eq. (2.40). Inset: calibration of the SINIS thermometer voltage against the bath temperature. (c) Injected power $P_{\rm SNS} = I_{\rm SNS}V_{\rm SNS}$ vs. the inverse of the measured $T_{\rm e}$ along the retrapping branch [see Fig. 5.2], at $T_{\rm bath} \simeq 50$ mK. The dashed line shows the predicted temperature rise for a given power, assuming it is determined only by the electron-phonon coupling in the N island. The solid line shows an estimate based on the quasiparticle heat conduction to the normal metal shadow along the paths indicated in Fig. 5.1.

the actual island volume $\Omega_{\rm N}$, predicting a significantly higher $T_{\rm e}$ (lower $T_{\rm e}^{-1}$) at a given $P_{\rm SNS}$. This estimate neglects any quasiparticle heat conduction through the clean NS contacts: they are assumed to function as perfect Andreev mirrors. However, with Al as the superconductor the picture valid at $\Delta \gg k_{\rm B}T_{\rm e}$ starts to break down at the relatively high values of $T_{\rm e} \gtrsim 300$ mK involved [179].

In our samples similar to Fig. 5.1, the relevant path for qp heat conduction is directed to the Cu shadow copies of the S leads, located a few μm away from each NS contact. At low temperatures T, the thermal conductance $G_{\rm th}$ of the piece of superconductor is suppressed below the normal state, Wiedemann-Franz value $G_{\rm th}^{\rm N} = \mathcal{L}_0 G_{\rm N}^{\rm sc} T$ according to Eq. (2.42). Neglecting electron-phonon coupling along the S section, the power $P_{\rm qp}$ can then be integrated as

$$P_{\rm qp}(T_{\rm e}) = \mathcal{L}_0 G_{\rm N}^{\rm sc} \int_{T_{\rm bath}}^{T_{\rm e}} dT \gamma(T) T. \tag{5.1}$$

Assuming a realistic value $G_{\rm N}^{\rm sc}$ for the relevant normal state electrical conductance, the solid line in Fig. 5.3 (c) shows the result of solving $P_{\rm SNS} = P_{\rm qp}$ for $T_{\rm e}$, assuming $\Delta = 215$ μeV and $G_{\rm N}^{\rm sc} = (4\ \Omega)^{-1}$.

To analyze the thermal balance of the system in more detail, including the hysteresis, we consider the steady-state power balance $P_{\rm SNS} = P_{\rm e-ph} + P_{\rm qp}$. We assume temperature-dependent $I_{\rm c}(T_{\rm e})$ given by Eq. (2.40) with the parameters of Fig. 5.3. Calculating the voltage $V_{\rm SNS}$ from the simple RSJ model of Eq. (2.6) (with $T_{\rm e}$ being the relevant temperature), Fig. 5.4 (a) shows a contour plot of $\Delta P = P_{\rm SNS} - P_{\rm e-ph} - P_{\rm qp}$ at $T_{\rm bath} = 150$ mK as a function of $T_{\rm e}$ and $I_{\rm SNS}$. The behavior of the system is determined by the zero contour. At low $T_{\rm bath}$, the hysteresis as a function of $I_{\rm SNS}$ follows from the backbending in a certain

range of I_{SNS}. The resulting V_{SNS} and T_{e} vs. I_{SNS} -characteristics agree qualitatively with the measurements, provided for the uncertainty in α and $G_{\mathrm{N}}^{\mathrm{sc}}$. However, the model is oversimplified as it neglects the non-sinusoidal current-phase relation in the SNS junction, and assumes that in the RSJ model of Eq. (2.6) T_{e} is the only temperature determining the IV characteristic of the junction.

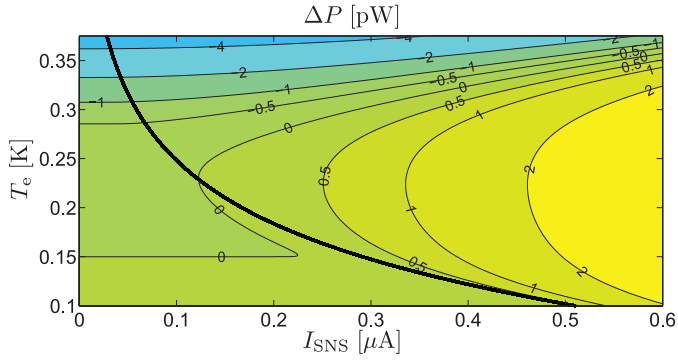

Figure 5.4: Contour plot of the function ΔP determining the power balance of the N island as a function of T_{e} and I_{SNS}. Parameters in the calculation correspond to Fig. 5.3, except $\alpha = 0.6$ instead of 0.5. The thick black line shows I_{c} vs. T_{e}. As I_{SNS} is increased close to or past I_{c}, the N island heats up and the junction transits to the resistive state. For large I_{SNS}, this high-T_{e} state is the only stable configuration. Similarly, for $I_{\mathrm{SNS}} < I_{\mathrm{r}}$, only a low-$T_{\mathrm{e}}$ supercurrent state is possible. For $I_{\mathrm{r}} < I_{\mathrm{SNS}} < I_{\mathrm{switch}}$, a third unstable state exists, but cannot be observed in a current-biased setup. Notably, as evident in from the switching currents in Fig. 5.3 (b), the intrinsic critical current I_{c} at the temperature T_{e} corresponding to retrapping is slightly below the retrapping current I_{r}.

To summarize, we have shown the hysteresis in metallic SNS junctions to be of thermal origin, suggesting that electron overheating can play a significant role also in several types of more exotic lateral weak links, such as with graphene [173] or carbon nanotubes [172].

5.2 SNS junction as a cold-electron transistor

SNS-SINIS structures similar to the one in Fig. 5.1 can be operated in several alternative ways. In Sec. 5, the NIS probes biased by a low current were utilized as electron thermometers. Alternatively, the NIS junctions can be voltage biased and utilized for electronic cooling as discussed in Sec. 2.3, in which case the exponential T_{e}-dependence of I_{switch} provides the thermometer [62, 180]. This is an advantage of the SNS thermometer against standard NIS thermometry, which loses sensitivity towards the lowest T_{e} [see Fig. 2.6]. Also, the ideally zero dissipation before the switch to the resistive state favors SNS thermometry at low temperatures.

In **V** we discuss using the strong I_{SNS}-dependence of V_{SINIS} evident in Fig. 5.2 (b) as a

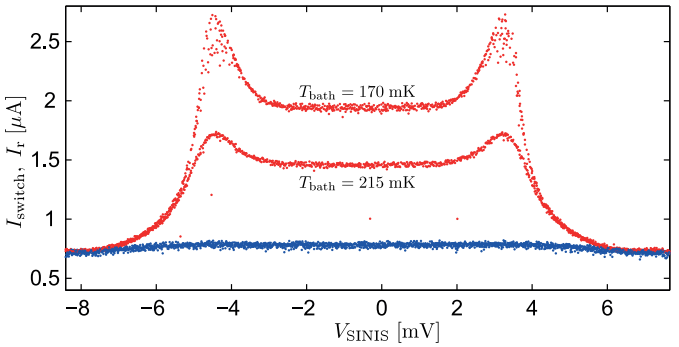

Figure 5.5: Red symbols: $I_{\rm switch}$ vs. $V_{\rm SINIS}$ -characteristics measured at two bath temperatures $T_{\rm bath}$, demonstrating the operation of an SNS-SINIS structure as a cold-electron Josephson transistor. Blue symbols indicate the retrapping current. $I_{\rm switch}$ increases sharply when the SINIS cooler is biased close to the optimum at $eV_{\rm SINIS} \lesssim 2\Delta$ and the island cools to a temperature $T_{\rm e}$ below $T_{\rm bath}$. The decrease in temperature can be read out using the SNS junction critical current as a thermometer.

more sensitive method for determining the switching current $I_{\rm sw}$ compared to measuring the voltage $V_{\rm SNS}$ across the SNS junction. In the nonhysteretic regime, a suitably defined extension of $I_{\rm switch}$ such as the value of $I_{\rm SNS}$ at which the differential temperature change $dT_{\rm e}/dI_{\rm SNS}$ reaches its maximum value remains useful. In addition, we demonstrate operation of the structure as a Josephson transistor [124, 125]: As shown in Fig. 5.5 at two bath temperatures, the switching current is considerably enhanced close to the optimum bias $eV_{\rm SINIS} \simeq 2\Delta$ of the cooler, reflecting the cooling of the island below $T_{\rm bath}$. Supercurrent enhancement by a large factor is evident also in Fig. 5.6. However, when trying to reach as low $T_{\rm e}$ as possible with NIS coolers, extrapolating the minimum temperature proves difficult.

The SNS-SINIS structures provide a class of tunable Josephson junctions. SNS junctions with a short normal metal control channel instead of tunnel junctions have been widely studied [122, 123, 181–186], as the appearance of a π-state (oscillatory decay of $I_{\rm c}$ vs. $T_{\rm bath}$, supercurrent flowing opposite to the phase gradient) is a signature of a nonequilibrium electron energy distribution in the N wire. In an SNS-SINIS structure, interestingly both supercurrent enhancement and a π-state have been predicted to be observable if electron-electron interaction is sufficiently weak [187, 188]. This is difficult to realize with Cu as the normal metal, in which quasiequilibrium is generally reached. On the other hand, with a short, thin and narrow Ag wire contacted by a single NIS probe, an effective temperature may no longer be a valid description [119], opening the way to extend the study of nonequilibrium effects in NIS junctions [65]. A detailed analysis of overheating in the S electrode of the NIS junction is required, as qp backtunneling at voltages $eV \gtrsim \Delta$ quickly diminishes the observable signatures [119].

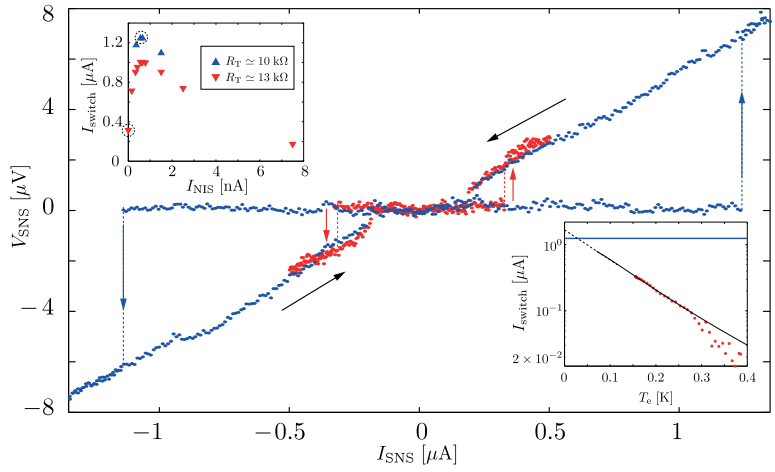

Figure 5.6: Probing the electronic refrigeration by NIS junctions using an SNS thermometer. Biasing an NIS junction close to the optimum voltage (corresponding here to bias currents $I_{NIS} \simeq 1$ nA for junctions with $R_T \simeq 10$ kΩ and $R_T \simeq 13$ kΩ, respectively) leads to a significant increase in the switching current as T_e decreases below T_{bath}. The red symbols show the equilibrium $I_{SNS}V_{SNS}$ characteristic ($I_{NIS} = 0$), whereas the blue curve is measured close to the optimum cooling at $I_{NIS} = 1$ nA through the NIS junction with $R_T \simeq 10$ kΩ. The two cases are indicated by the black dotted circles in the left inset, displaying a coarse I_{switch} vs. I_{NIS} -characteristic. As in Fig. 2.6, cooling at the optimum point is followed by strong heating at higher I_{NIS}. The thick blue line in the right inset shows the measured maximum switching current, together with the I_{switch} vs. T_{bath} calibration and linear fit on the semilogarithmic scale. Determination of the minimum T_e reached at the optimum I_{NIS} is somewhat uncertain because of the required extrapolation. Depending on the range used for the linear fit, we approximate in this case $T_{e,min} = 25 \pm 15$ mK.

Chapter 6

Probing the phase-dependent density of states of an SNS junction

In an SNS structure, the density of states $n_{\mathrm{N}}(E, x, \phi)$ in the proximized normal metal depends on the position along the N wire as well as phase difference ϕ between the S electrodes [cf. Eq. (2.37)], the latter of which can be changed by an external magnetic field. When probed by measuring the IV characteristic of an NIS junction, this allows to create a sensitive interferometer for the detection of small magnetic fields. In **VI** and **VII** we report the realization and subsequent optimization of such a device, named the SQUIPT (Superconducting Quantum Interference Proximity Transistor), in analog to a SQUID [24]. Recently, the energy, position, and phase dependence of DoS along the N wire in an SNS junction has been accurately measured by low temperature AFM-STM techniques [82], confirming the validity of describing proximity circuits in terms of the diffusive Usadel equations.

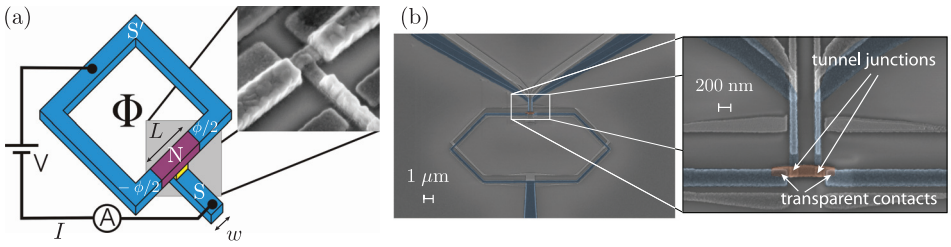

Figure 6.1: (a) Operation principle of the SQUIPT interferometer. A superconducting loop is interrupted by a short normal metal section. The magnetic flux Φ modifies the DoS of the N wire, which is measured by tunnel spectroscopy with the embedded NIS tunnel junction. (b) Electron micrograph of a structure with an N wire of length $L \simeq 1.5$ μm, contacted by two NIS junctions.

Figure 6.1 (a) displays a schematic of a SQUIPT structure: A superconducting fork-shaped electrode S' (blue, bulk energy gap Δ_1, thickness d_1, width w_1) is contacted via direct metal-to metal NS contacts to a normal metal wire of length L (red), forming a superconducting loop interrupted by an SNS weak link. Similarly to the structures in Sec. 5.1, the N wire is contacted by one or several superconducting electrodes S (blue, bulk energy gap Δ_0, thickness d, width w) via a tunnel barrier (yellow). Neglecting self-inductance of the S loop, the phase difference ϕ is fixed by an external magnetic flux Φ threading the loop according to $\phi = 2\pi\Phi/\Phi_0$. The shorter the N wire, the stronger the proximity effect modifies the N DoS, and the larger flux modulation of the DoS will result. As illustrated in Fig. 6.1, these changes can be probed by measuring the current I through the NIS junction of resistance R_T, biased at a constant voltage V. The current I is obtained from Eq. (2.27) with $n_1(E) = n_\mathrm{N}(E, x, \Phi)$, $n_2(E) = n_\mathrm{S}(E)$, and $P(E) = \delta(E)$ as

$$I = \frac{1}{eR_\mathrm{T}} \int_{-\infty}^{\infty} dE n_\mathrm{N}(E, \Phi) n_\mathrm{S}(E - eV) \left[f_\mathrm{S}(E - eV) - f_\mathrm{N}(E) \right], \tag{6.1}$$

where in the simplest approximations the N DoS $n_\mathrm{N}(E, \Phi)$ can be evaluated at a single point along the tunnel junction overlap, or it can be averaged across the width w. For a more quantitative description of the IV characteristics, the energy exchange with the electrical environment of the junction can be included in terms of the $P(E)$-theory [56] (see **VII**), utilized and discussed in Ch. 8 in more detail.

Figure 6.1 (b) shows a colored SEM micrograph of a device similar to the ones investigated in **VI**. All the studied structures had two tunnel junctions contacting the N island, therefore limiting the minimum length $L \gtrsim 1$ μm, whereas half of them did not include the common loop electrode. The voltages or currents were measured either via a single junction and the loop electrode, or in a two junction SINIS configuration. Besides the simple voltage- or current biased readout, a major advantage of the structures is the low dissipation $\sim 1 - 100$ fW, typically at least three orders of magnitude less than in a conventional DC-SQUID operated above its critical current [24]. This is a direct consequence of the high impedance of the NIS junction, and the small currents and voltages required to reach the sensitive working point. Also, the tunnel junction properties can be adjusted to a large extent independently from the SNS weak link that determines the size of the minigap and therefore the maximum voltage modulation.

The DoS in the middle of an SNS junction with $\Delta/E_\mathrm{Th} = (L/\xi_0)^2 = 30$ calculated according to Eqs. (2.37) is illustrated in Fig. 6.2 (a). The various curves correspond to different fluxes Φ through the loop. The most characteristic feature of the DoS is the appearance of a phase-dependent minigap E_g [85, 86], which obtains its maximum value at $\Phi = 0$ and closes at $\Phi = \Phi_0/2$. The size of the E_g remains constant throughout the N wire, whereas the above-E_g structure varies with position as well as Φ, as demonstrated by STM measurements [82]. Figure 6.2 (b) shows the corresponding IV characteristics of the embedded tunnel junction based on Eq. (6.1). δV denotes the amplitude of the voltage modulation $V(\Phi)$ at a constant current bias.

In Fig. 6.3 (a) we show a set of measured Φ_0-periodic voltage modulations at various I of a sample with $L \simeq 1$ μm, similar to that in Fig. 6.1 (b). Furthermore, Fig. 6.3 (b) indicates how $V(\Phi)$ at a constant I evolves as temperature is increased. Due

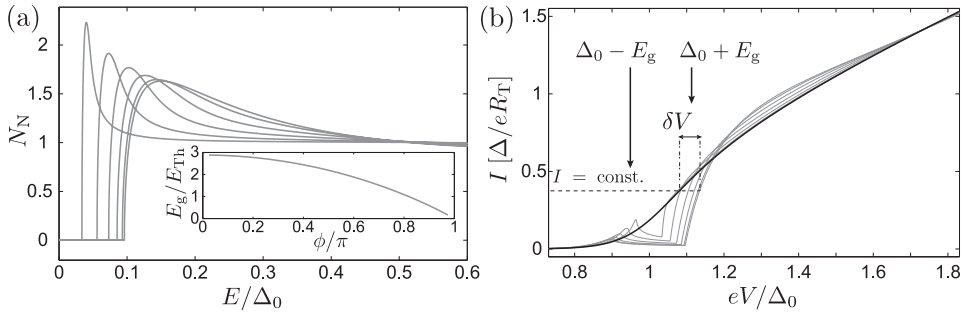

Figure 6.2: (a) Normalized DoS in the middle of the N wire in an SNS junction with $\Delta/E_{\rm Th} = 30$ for selected ϕ between 0.025π and 0.82π, showing the reduction of the minigap $E_{\rm g}$ as well changes in the above-$E_{\rm g}$ structure. Inset: ϕ-dependence of the minigap. For $\Delta/E_{\rm Th} \gg 1$, $E_{\rm g}/E_{\rm Th}$ behaves as $C_2(1 - C_1\phi^2)$ at $\phi \ll \pi$, and as $\pi^2(\pi - \phi)/4$ for $\pi - \phi \ll \pi$ [85, 86]. The numerical constants have the values $C_1 \simeq 0.0921$ and $C_2 \simeq 3.122$. (b) Current I through an NIS junction with the N DoS from (a). Features at $|\Delta_0 \pm E_{\rm g}|$ are evident, similar to an SIS junction. δV denotes the magnitude of the voltage modulation at a constant I. Phase modulation of the current at $eV > \Delta_0 + E_{\rm g}$ is evident, and the characteristics calculated with various ϕ are crossing each other in a certain range of voltages V. A similar crossing as a function of temperature takes place also in a regular NIS junction where one of the electrodes is fully normal [cf. Fig. 2.6].

to the crossing of the characteristics in Fig. 6.2, the maximum derivative $\mathrm{Max}|\partial V/\partial\Phi|$ at a constant temperature is a nonmonotonous function of the bias current. A similar change of concavity happens at a constant current but as a function of temperature. Under current bias, the initial sample design of Fig. 6.1 (b) achieved the maximum voltage modulation $\delta V \simeq 12\ \mu$V and the maximum transfer function $|\partial V/\partial\Phi| \simeq 60\ \mu\mathrm{V}/\Phi_0$ when biased through both NIS junctions in series. Measuring across the loop electrode and only one junction, the values were reduced to 7 μV and 30 $\mu\mathrm{V}/\Phi_0$, respectively. On the other hand, the short-junction samples in **VII** reached $|\partial V/\partial\Phi| \simeq 1.5$ mV/Φ_0 and $|\partial I/\partial\Phi| \simeq 3$ nA/Φ_0 even at the elevated temperature $T_0 \simeq 585$ mK. The noise performance of the structures can be characterized in terms of the noise-equivalent flux (flux sensitivity) $NEF = \langle V_{\rm N}^2\rangle^{1/2}/|\partial V/\partial\Phi|\delta f^{1/2}$, which represents the input-referred voltage noise in the system in the frequency band δf. Here, $\langle V_{\rm N}^2\rangle^{1/2}$ is the RMS voltage noise of the system [2, 24]. In the measurements done with room temperature preamplifiers, the sensitivity was limited by the amplifier noise $\langle V_{\rm N}^2\rangle^{1/2} \gtrsim 1\ \mathrm{nVHz}^{-1/2}$. However, even in the non-optimized samples of **VI**, $NEF \simeq 2 \times 10^{-5}\Phi_0\mathrm{Hz}^{-1/2}$ was achieved, comparable to a regular SQUID [24]. The shorter samples with larger $|\partial V/\partial\Phi|$ yielded $\lesssim 6\times10^{-6}\Phi_0\mathrm{Hz}^{-1/2}$, and the preamplifier contribution to NEF can be made negligible by further optimization. Study of the intrinsic noise mechanisms becomes then necessary.

The observed amplitude of the voltage modulation is $30 - 50\%$ smaller than the prediction based on Eq. (6.1). In part, this can be attributed to uncertainty in determining

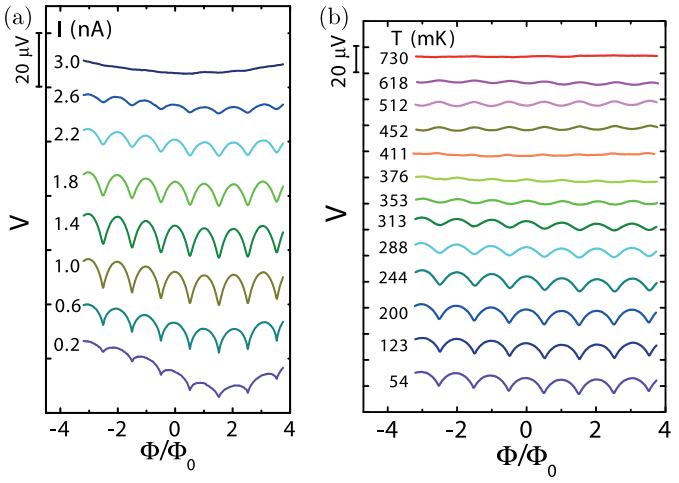

Figure 6.3: (a) Measured flux dependence of the voltage modulation at various constant bias currents at $T \simeq 50$ mK in a SINIS configuration. The curves are vertically offset for clarity. The large-scale field dependence can be due to other effects caused by the field besides the phase-dependent DoS, predicted to occur in SNS proximity structures [167, 189]. In high fields, also depairing in the S electrodes is expected [14]. (b) Temperature dependence of the voltage modulation at the constant bias current $I = 1$ nA.

E_{Th}, the finite width of the tunnel probe, and the neglect of electron cooling or heating in the N wire. The modulation is also reduced by imperfect phase biasing of the SNS junction, which may prevent the full closure of the minigap, too. For ideal phase biasing, all the phase should drop across the N wire. However, in practise there is a finite phase gradient also in the superconductor due to its finite kinetic inductance $L_{\mathrm{K}}^{\mathrm{S}} = R_{\mathrm{N}}^{\mathrm{S}}\hbar/\pi\Delta_1$, where $R_{\mathrm{N}}^{\mathrm{S}}$ is the normal state resistance of the S wire. Similarly, for the proximized N wire the inductance is approximately $L_{\mathrm{K}}^{\mathrm{N}} \simeq R_{\mathrm{N}}^{\mathrm{N}}\hbar/E_{\mathrm{g}}$. For the structures in **VI**, we estimate the ratio $L_{\mathrm{K}}^{\mathrm{S}}/L_{\mathrm{K}}^{\mathrm{N}} \simeq 0.3 - 0.5$, which determines the fraction of phase dropped across the superconductor. Secondly, due to the finite geometric inductance L_{G} of the loop, the actual flux Φ through the loop is the applied flux Φ_{ext} screened by the flux produced by the circulating supercurrent $I_{\mathrm{S}}(\phi)$. The relation $\phi = 2\pi\Phi/\Phi_0 \pmod{2\pi}$ still holds, but Φ has to be solved self-consistently from [3] $\Phi = \Phi_{\mathrm{ext}} - L_{\mathrm{G}} I_{\mathrm{S}}(2\pi\Phi/\Phi_0)$. Assuming a sinusoidal current-phase relation $I_{\mathrm{S}} = I_{\mathrm{c}} \sin(2\pi\Phi/\Phi_0)$, one finds that for $2\pi L_{\mathrm{G}} I_{\mathrm{c}} \gtrsim \Phi_0$ the resulting Φ vs. Φ_{ext} -characteristic is hysteretic, as observed in the short junctions in **VII**. The hysteresis in Φ_{ext} can be avoided by reducing I_{c} of the junction either via controlling the temperature, geometry, or material parameters, or by reducing the inductance $L_{\mathrm{G}} \sim \mu_0 l$, where l is an effective radius of the loop [3].

Discussion

The normal metal weak link can be replaced, e.g, by a sheet of graphene or a carbon nanotube. In [190] a SQUIPT interferometer structure with a nanotube weak link allowed to study the Andreev Bound states in the proximized nanotube in detail.

In the short junction limit $L \ll \xi_0$, i.e., $E_{\rm Th} \gg \Delta_1$, proximity effect in the N wire is strong and the Usadel equations allow for an analytic solution for θ and χ [90]. The structures with a single tunnel junction investigated in **VII** had $L \simeq 2\xi_0$, or $E_{\rm Th} \simeq 4\Delta_1$, and the limit can be approached with a further reduction of L. Under this assumption, the potential and optimization of the SQUIPT has been further analyzed in [191]. Alternatively, depending on the desired temperature range, the sensitivity can be increased by replacing the Al loop by a superconductor with higher energy gap Δ_1, e.g, vanadium with $\Delta_1 \simeq 0.4$ meV [192], or niobium with $\Delta_1 \simeq 1$ meV.

Because of the phase dependence of $n_{\rm N}(E, \Phi)$, the probe junction voltage in the SNS-SINIS structures of Sec. 5.1 varies in principle with $I_{\rm SNS}$ even at constant temperature. However, in an externally current-biased setup without a superconducting loop, the SNS junction is not perfectly phase biased. The thermometer is also biased at such a low current in the sub-gap regime that the phase modulation of the DoS has a very small effect. However, this sensitivity to a supercurrent could possibly allow the SQUIPT to replace SIS junction threshold detection to probe the small pumped currents in coherent Cooper pair pumping [193].

As discussed at the end of Sec. 5.1, the samples with relatively short L in **VII** could be suited for the study of nonequilibrium effects in superconducting proximity structures. This would require using Ag as the N wire material, as well additional contacts for measuring the SNS critical current. Moreover, the N wire cross section would have to be reduced to diminish $I_{\rm c}$ so that overheating effects can be avoided.

Modification of the electron-phonon coupling by the proximity effect is another fundamental property that can be studied in the SNS loop structure. At low temperatures $k_{\rm B}T \lesssim E_{\rm Th}$, the power flow $P_{\rm e-ph}$ to the phonons has been predicted to be suppressed by a factor $e^{-3.7E_{\rm Th}/k_{\rm B}T}$ at $\Phi = 0$ relative to the usual normal state value $P^{\rm N}_{\rm e-ph} = \Sigma_{\rm N}\Omega_{\rm N}(T^5 - T_0^5)$ [194]. In addition, the heat flux now depends on Φ, similar to the DoS. This phase dependence of $P_{\rm e-ph}$ can then in principle be used to distinguish the effect using NIS junctions for thermometry and heating or cooling. However, even if the thermometers are calibrated separately at each Φ, also the cooling power changes with the flux because of its dependence on $n_{\rm N}(E, \phi)$. Finally, heat conduction through the NS contacts cannot be neglected, complicating the direct measurement of $P_{\rm e-ph}$.

Chapter 7

Thermal conductance of NSN proximity structures

Electric transport in proximity structures has been studied in considerably more detail [77] compared to thermal phenomena, in part because of the limited possibilities for local thermometry at low temperatures. Notable recent exceptions include the measurement and analysis of the thermal conductance $G_{\rm th}$ of Andreev interferometers [195–198], formed by an N wire between two N reservoirs that is contacted in addition to one or more S electrodes in the middle. Temperatures were probed locally based on the temperature-dependent resistance of a long SNS structure [199, 200]. In an Andreev interferometer structure, the thermal conductance and thermopower can be made to depend on the phase difference between the S electrodes, manifesting long-range coherence in the normal part. The electric and thermal transport in this kind of multiterminal structures are intricately connected, leading to non-trivial thermoelectric effects in general [117, 126, 201].

As a part of the early experimental studies of the proximity effect, $G_{\rm th}$ of large-area stacked NSN sandwiches was measured in a temperature range close to $T_{\rm C}$. The measurement of $G_{\rm th}$ in a controlled lateral geometry at low temperatures has been missing, motivating our study in **VIII**. This is of relevance also for the better control and estimation of heat flows in applications combining proximity structures and NIS junction refrigeration: In **IV** the temperature rise on the island was determined by qp heat conduction to the N reservoir via the short S section. The model based on BCS $G_{\rm th}$ gave the correct order of magnitude of the heat flow, but led to an overestimation of $G_{\rm th}$ because of the uncertainty in determining the relevant normal state electrical resistance.

7.1 Heat transport in a short 1D NSN structure

We studied a series of structures similar to the one in Fig. 7.1 (a), consisting of an S wire of the indicated, non-overlapping length $L_{\rm S}$ contacted to two N islands via clean overlap-type contacts of length $L_0 \simeq 200$ nm. A cross section of such a lateral NSN wire is included in Fig. 7.1 (b). $L_{\rm S}$ was varied from sample to sample in the range 400 nm $-$ 4 μm, comparable to the coherence length $\xi_0 = \sqrt{\hbar D_{\rm S}/\Delta_0} \simeq 100 - 150$ nm. The N islands 1 and

2 are assumed to act as reservoirs, with the electronic temperatures T_1 and T_2 probed by current biased SINIS thermometers. To probe $G_{\rm th}$, a temperature difference $\Delta T = T_2 - T_1$ is imposed by heating or cooling island 1 (the local island) by a SINIS cooler. Both T_1 and T_2 are measured. Defining $T = (T_1 + T_2)/2$, $G_{\rm th}(T) = P_{\rm S}(T)/\Delta T$ can then be inferred from a thermal model of the system in terms of the power flow $P_{\rm S}(T)$ between the islands, in the limit of small ΔT [see Fig. 7.3 (d)]. This requires that on island 2 (the remote island), the heat flow from electrons to phonons is known so that the qp heat flow through the S wire is the only unknown channel of heat conduction.

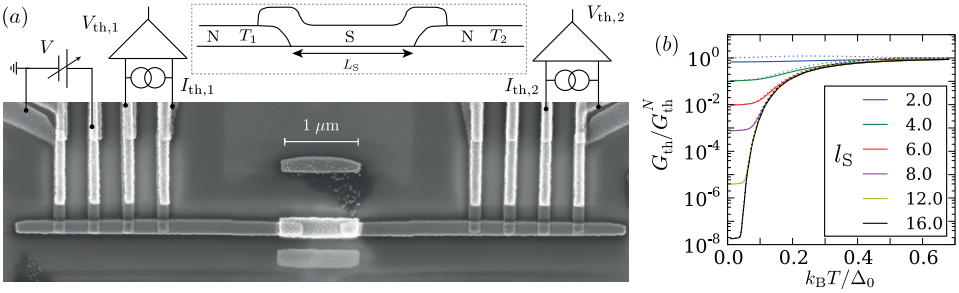

Figure 7.1: (a) SEM micrograph of a sample for measuring the thermal conductance $G_{\rm th}$ of an NSN structure, together with the measurement scheme. A short Al wire is contacted to two Cu islands via direct NS contacts. Each island contains four probe junctions. Top: Sketch of the cross section of the structure. (b) Predicted suppression of the $G_{\rm th}$ for NSN structures with varying S lengths $l_{\rm S} = L_{\rm S}/\xi_0$.

As noted in Sec. 2.4, for an S wire with $L_{\rm S} \gtrsim \xi_0$, $G_{\rm th}$ is expected to be enhanced beyond the BCS value of Eq. (2.42) due to the inverse proximity effect. Besides the suppression of the energy gap, sub-gap heat transport can take place due to the mechanisms of crossed Andreev reflection and elastic cotunneling [92, 202, 203]: a qp at sub-gap energy can penetrate from one N lead to the other similar to an evanescent wave, resulting in a finite $M(E)$ in Eq. (2.41) at $E < \Delta$. Figure 7.1 (b) shows the resulting $G_{\rm th}$, based on an analytic approximation for θ valid at $L_{\rm S} \gtrsim 2$. This basic model neglects the suppression of Δ, the overlap regions, as well as the proximity effect in the N reservoirs, assumed to have much larger cross section than the middle S section. As discussed in the supplementary information to **VIII**, these corrections can be included in a more accurate self-consistent numerical quasi-1D model of the structure. The qualitative behavior is, however, captured by Fig. 7.1 (b): Towards shorter $L_{\rm S}$, $G_{\rm th}$ at low temperatures is no longer exponentially suppressed relative to the normal state value $G_{\rm th}^{\rm N}$. Instead, it saturates to a constant value, followed by a power-law increase with temperature.

Figure 7.2 displays the local and remote electronic temperatures T_1 and T_2 as a function of the cooler bias V at certain constant bath temperatures T_0 for four representative samples with different $L_{\rm S}$. At the highest T_0 shown, the two temperatures follow closely each other for all the samples. In contrast, towards lower T_0, a notable difference develops: For the shorter samples, only a small difference is seen, corresponding to a strong thermal

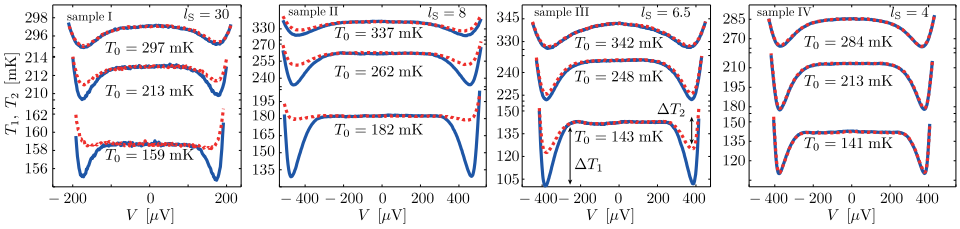

Figure 7.2: Electronic temperatures of the local (T_1, solid blue) and remote islands (T_2, dashed red) as a function of the cooler bias voltage V. Each panel corresponds to the indicated length l_S, and shows data from three selected bath temperatures.

link between the islands. On the other hand, for the largest L_S, T_2 remains constant until the onset of the strong heating at $|eV| > 2\Delta$, indicating effective thermal isolation of the N islands.

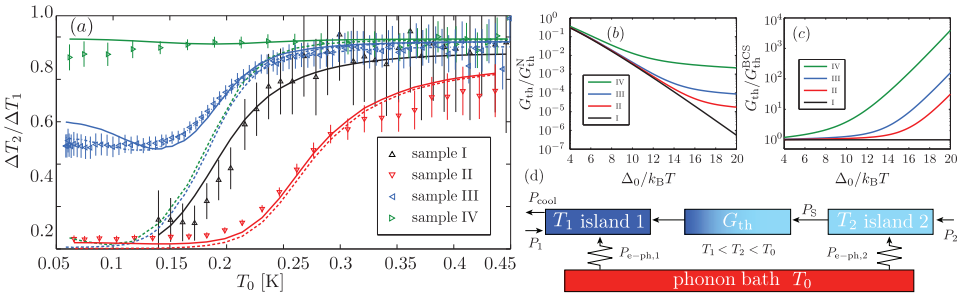

Figure 7.3: (a) Symbols: Measured T_0-dependence of the maximum temperature drop $\Delta T_2/\Delta T_1$ for the four samples. Dashed lines: Predicted behavior including only the above-gap contributions to the thermal conductance. Solid lines: Basic thermal model including the sub-gap transport. Dash-dotted line for sample III: Full self-consistent model including the overlap regions. (b),(c) Normalized thermal conductance G_{th} for each sample, corresponding to the solid lines in (a). (d) Thermal diagram of the NSN structure. Electron-phonon coupling along the short superconducting wire is neglected, as well as cooling or heating of the N island phonons. The latter can open an indirect heat conduction channel parallel to G_{th}, but becomes relevant only for longer S wires or higher power levels.

To characterize the coupling between the reservoirs, i.e., the qp thermal conductance G_{th} through the S wire, we consider the ratio $\Delta T_2/\Delta T_1$ of the temperature drops $\Delta T_i(V) = T_i(V) - T_i(V=0)$, $i = 1, 2$ at the optimum cooler bias, $eV = eV_{opt} \lesssim 2\Delta$. This quantity is plotted in Fig. 7.3 (a) for the samples of Fig. 7.2, making more evident the difference in the low temperature behavior between the long and the short S wires. We focus on the quantity $\Delta T_2/\Delta T_1$ as it emphasizes the thermal coupling between the islands, and has

ideally no dependence on the absolute cooling power of the refrigerating SINIS structure, allowing a more direct comparison between different samples. To model the behavior of $\Delta T_2/\Delta T_1$, we assume the thermal model of Fig. 7.3 (d) and solve the steady state heat balance equations $P_{\rm cool} - P_{\rm S} - P_{\rm e-ph,1} - P_1 = 0$ and $P_{\rm S} - P_{\rm e-ph,2} - P_2 = 0$ for island 1 and 2, respectively. Here, $P_{\rm cool}$ is the cooling power of the SINIS refrigerator, $P_{\rm S}$ is the qp heat flow from island 2 to island 1, integrated from $G_{\rm e-ph,2}(T)$. $P_{{\rm e-ph},i} = \Sigma_{\rm N}\mathcal{V}_i(T_0^5 - T_i^5)$ denotes the electron-phonon heat flow on island i, and P_i is a residual constant power. With a given $G_{\rm th}(T)$, both temperatures T_1 and T_2 can be solved if $P_{\rm cool}$ is known accurately. To reasonably fit the temperature of island 1, the powers from Eq. (2.33) have to be reduced by $\beta\dot{Q}_{\rm S}$ with the phenomenological parameter $\beta \lesssim 0.1$ to account for backflow of heat due to the overheating of the cooler S electrodes [71, 204]. In a consistent model, temperature profile of the S electrodes has to be solved from a diffusion equation describing the relaxation of the excess quasiparticles [205], see **XI**. Since we are focusing on $G_{\rm th}$, we solve only the equation for island 2, taking the measured temperature of island 1 as an input to the model. To see the connection between $\Delta T_2/\Delta T_1$ and $G_{\rm th}$, for small ΔT this remaining equation can be linearized to yield $\Delta T_2/\Delta T_1 \simeq G_{\rm th}/(G_{\rm th} + G_{\rm e-ph,2})$ with $G_{\rm e-ph,2} = 5\Sigma\mathcal{V}_2 T_0^4$.

Predictions of the BCS above-gap thermal conductance are shown as the dashed lines using realistic values for the wire length and normal state resistance. $\Delta T_2/\Delta T_1$ of the two longest samples can be reasonably explained in terms of the exponentially suppressed $G_{\rm th}$. For the shorter wires there is a crossover to sub-gap dominated conduction at low T_0. The solid lines show the non-self-consistent model where this effect is included. $\Delta T_2/\Delta T_1$ at the lowest T_0 is sensitive to $l_{\rm S} \lesssim 10$. For sample II this is in part counteracted by the larger Δ_0 and higher normal state resistivity. In case of sample III, the dash-dotted line shows $\Delta T_2/\Delta T_1$ based on the self-consistent numerical calculation of $G_{\rm th}$. Such evaluation for sample IV yields a value very close to unity and the non-self-consistent result, due to the domination of $G_{\rm th}$ over $G_{\rm e-ph,2}$ irrespective of the exact parameters. $G_{\rm th}$ at the lowest temperatures in the short wires is enhanced by $2-4$ orders of magnitude compared to the BCS value while remaining considerably below $G_{\rm th}^{\rm N}$. Similarly to earlier measurements with Al wires [179], at $T_0 \gtrsim 0.3$ K the qp heat conduction is dominating the electron-phonon coupling in all the samples, and the S wires can no longer be considered as thermal isolators.

To summarize, we have probed heat transport through NSN structures. Thermal conductance calculated from the Usadel equations accounts for the measurements, provided for the uncertainty in transforming the structure into an effective 1D circuit. With the thermal conduction measured in a well-defined lateral geometry, heat flows can be better controlled for example in hybrid structures similar to those in Ch. 5. The same setup utilizing NIS junctions for local thermometry and temperature control can be applied to other mesoscopic structures, provided their $G_{\rm th}$ is close to $G_{\rm e-ph,2}$ [179].

7.2 Tunnel junctions based on the inverse proximity effect

From the self-consistent analysis of the thermal conductance of an NSN structure, it follows that $T_C = 0$ in a 1D S wire of length shorter than the critical length $L_{cr} = \pi\xi_0$ [206–208]. This assumes perfect NS contacts and neglects any proximity effect in the infinite N reservoirs. For a short S island contacted to a single N reservoir, symmetry dictates that $L_{cr} = \pi\xi_0/2$. Non-ideal interfaces and finite N cross section reduce the length L_{cr}, but it may remain long enough to fabricate NS structures where superconductivity is effectively suppressed at relevant experimental temperatures. As demonstrated in **IX** and illustrated in Fig. 7.4, applying this to suppress superconductivity in aluminum opens up the possibility for shadow-evaporation-based fabrication of hybrid NIS junctions with other superconductors besides the standard choice Al, or utilizing fully normal NIN junctions without applying any magnetic fields. In addition, both such pseudo-NIN and regular NIS junctions can be reliably fabricated in a single vacuum cycle onto a single chip, allowing for example to study heat transport in the presence of Coulomb blockade in a fully normal metallic single-electron transistor [209]. Suppressing the superconductivity with a lateral contact to a normal reservoir is an alternative to evaporating a thin layer of Al on top of a thicker normal metal [81].

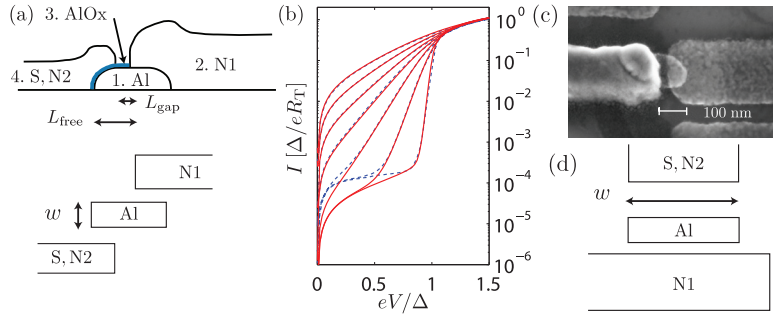

Figure 7.4: (a) Schematic of the cross section of a tunnel junction based on the suppression of superconductivity in a short Al island. The numbers indicate deposition order of the layers. The mask for shadow evaporation is shown at the bottom. (c) Micrograph of an Cu-Al-AlOx-Al NIS junction with the total non-overlapped Al length $L_{free} \simeq 100$ nm, fabricated according to the principle of (a). (b) Measured IV characteristics (dashed lines) of the structure in (c) compared to the current expected from Eq. (2.31) (solid lines) at various bath temperatures. (d) A design with less constrained junction width w, where the shift due to angle evaporation takes place perpendicular to w.

Figure 7.4 (a) sketches the cross section along an AlOx-based tunnel junction utilizing the lateral suppression of superconductivity in a small Al island. A possible shadow mask design is shown at the bottom. The junction is formed by oxidizing the non-overlapped part of the island and subsequent deposition of a counterelectrode. A non-overlapping area of length L_{gap} remains between this electrode and the thick N. The variant in (d) does

not limit the junction width and allows for accurate adjustment of L_{gap} by varying the tilt angles of the metal depositions. In this manner, Cu-Al-AlOx-Al NIS junctions with a thick superconducting Al electrode can be fabricated, important for reaching the optimal cooling power in SINIS refrigerators [see Ch. 9].

As an example, Fig. 7.4 (b) shows the qp IV characteristic at several bath temperatures for the single NIS junction depicted in (c). At all but the lowest temperatures, the measured currents are in good agreement with Eq. (2.31) assuming a smeared BCS DoS with $\Gamma \simeq 1 \times 10^{-4}\Delta$, demonstrating that the Al island can be driven normal to a degree sufficient for applications. Besides the NIS test junctions, similar conclusions can be drawn for the normal-state single-electron transistors described in **IX**.

Chapter 8

Brownian refrigeration in an NIS junction

In Sec. 2.3 we considered the electronic cooling in a voltage biased NIS junction in a low-impedance environment, where only elastic quasiparticle tunneling is possible. Notably, under proper conditions cooling is possible also in the absence of the bias voltage, only due to voltage fluctuations generated in the electrical environment of the junction. Due to the superconductor energy gap, an NIS junction can extract useful work out of the fluctuations and to generate a net cooling effect of the normal metal electrode, constituting the principle of Brownian refrigeration. The system acts as a heat rectifier resembling a Maxwell's demon, allowing only the most energetic qps to tunnel from the normal metal. However, the entropy of the complete system consisting of the junction and its environment is always increasing, and the system follows the second law of thermodynamics. The effect was initially proposed in Ref. [210] in the context of NIS junctions. The influence of the electrical environment of a tunnel junction on the heat transport by quasiparticle tunneling has received little attention. On the other hand, environmental effects of the electrical transport have been studied extensively [56, 211].

To see how the cooling effect due to environmental fluctuations arises in an NIS junction (tunnel resistance $R_{\rm T}$, capacitance C, electrode temperatures $T_{\rm N}$ and $T_{\rm S}$) coupled to a resistance R heated to $k_{\rm B}T_{\rm R} \gg \hbar/(RC)$, let us first consider a classical averaging of the cooling power $\dot{Q}_{\rm N}$, valid for low frequency fluctuations (small $E_{\rm C}$, low circuit cut-off frequency). The system is illustrated in Fig. 8.1 (a). Similar to the expression for the current in Eq. (2.32), the cooling power $\dot{Q}_{\rm N}$ from Eq (2.33) can be approximated at $k_{\rm B}T_{\rm N} \ll \Delta$ by

$$\dot{Q}_{\rm N} \simeq \frac{\Delta^2}{e^2 R_{\rm T}} \sqrt{\frac{\pi}{2}} \left[\frac{\Delta}{k_{\rm B}T_{\rm N}} - \frac{|eV|}{k_{\rm B}T_{\rm N}} \right] \left(\frac{k_{\rm B}T_{\rm N}}{\Delta} \right)^{3/2} \exp\left[- \left(\frac{\Delta}{k_{\rm B}T_{\rm N}} - \frac{|eV|}{k_{\rm B}T_{\rm N}} \right) \right], \tag{8.1}$$

where we neglected the influence of finite $T_{\rm S}$. Then, in the presence of a fluctuating voltage $\delta V(t)$, the average cooling power during a period of time Δt reads

$$\frac{1}{\Delta t} \int_0^{\Delta t} dt\, \dot{Q}_{\rm N}(\delta V(t)) = \langle \dot{Q}_{\rm N}(\delta V) \rangle = \int_{-\infty}^{\infty} d(eV) p(eV) \dot{Q}_{\rm N}(eV), \tag{8.2}$$

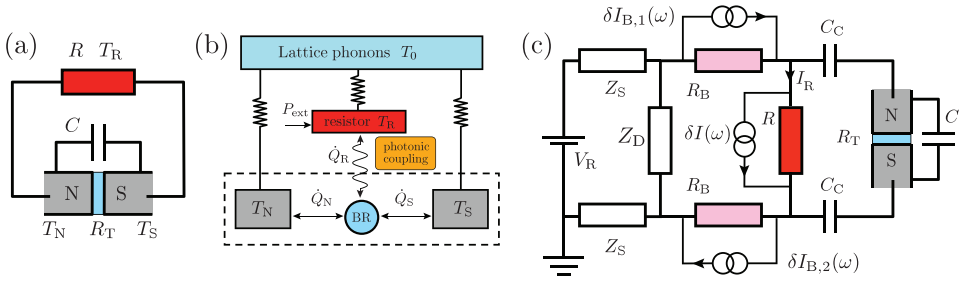

Figure 8.1: (a) Principle of Brownian refrigeration. Fluctuations generated in a resistor coupled to an NIS junction can result in net heat flows $\dot{Q}_\mathrm{N}$ and $\dot{Q}_\mathrm{S}$ into or out from the N and S electrode, even under zero voltage bias across the junction and at $T_\mathrm{N} = T_\mathrm{S}$. The probability for a quasiparticle to absorb energy $E' - E > 0$ is described by the function $P(E - E')$. Under suitable conditions, it has such a form that the noise from a hot resistor ($T_\mathrm{R} > T_\mathrm{N}, T_\mathrm{S}$) results in cooling of the N electrode, $\dot{Q}_\mathrm{N} > 0$, in a wide range of resistor temperatures T_R. (b) Heat flows in the system, related to the environment-assisted qp tunneling. The NIS junctions acts as a Brownian refrigerator (BR) between the N and S electrodes. (c) Practical coupling scheme for the noise-generating resistor and the NIS junction. The resistor is heated to T_R by voltage biasing it with a voltage V_R, resulting in an average current I_R. Current fluctuations $\delta I(\omega)$ are coupled to the junction via capacitors C_C while blocking I_R. The additional on-chip resistors R_B prevent the fluctuations from being shunted in the biasing circuit, represented by the lead impedances Z_S and the shunting impedance Z_D.

where the replacement of the time average by a statistical average (denoted by the angle brackets) follows from an ergodicity assumption. The quantity $p(eV)$ is the Gaussian probability density for the voltage fluctuation V across the junction. For $R_\mathrm{T} \gg R$ the junction noise can be neglected, and the spectral density of voltage fluctuations due to the resistor is $S_\mathrm{V}(\omega) \simeq 4k_\mathrm{B}T_\mathrm{R}R/(1 + \omega^2R^2C^2)$ yielding the RMS value $\langle V^2\rangle^{1/2} \simeq k_\mathrm{B}T_\mathrm{R}/C$, whence $p(eV) = \exp\left[-(eV)^2/(2\sigma)\right]/\sqrt{2\pi\sigma}$ with $\sigma = s^2 = 2k_\mathrm{B}T_\mathrm{R}E_\mathrm{C}$. Assuming $s \gg k_\mathrm{B}T_\mathrm{N}$, the averaging can be performed with the result

$$\langle \dot{Q}_\mathrm{N}\rangle \simeq \frac{\Delta^2}{e^2R_\mathrm{T}}\sqrt{\frac{2\pi k_\mathrm{B}T_\mathrm{N}}{\Delta}}e^{-\frac{\Delta}{k_\mathrm{B}T_\mathrm{N}}}\left\{\frac{-1}{\sqrt{\pi}}\sqrt{\frac{k_\mathrm{B}T_\mathrm{R}}{\Delta}}\sqrt{\frac{E_\mathrm{C}}{\Delta}}+e^{\left(\frac{T_\mathrm{R}}{T_\mathrm{N}}\right)\left(\frac{E_\mathrm{C}}{k_\mathrm{B}T_\mathrm{N}}\right)}\left[1-2\left(\frac{T_\mathrm{R}}{T_\mathrm{N}}\right)\left(\frac{E_\mathrm{C}}{\Delta}\right)\right]\right\}. \tag{8.3}$$

At a fixed T_N, E_C, and Δ, Eq. (8.3) indeed predicts a net heat flow out of the N electrode for a range of resistor temperatures T_R. This result, however, neglects for example the backflow of heat from the resistor to the quasiparticles. To analyze the effect more quantitatively, we use the $P(E)$-theory introduced in Sec. 2.3 for describing the qp tunneling in a general hybrid junction in an environment. Importantly for the Brownian refrigeration at $V = 0$, the net heat flow out of electrode i, given by Eq. (2.30), simplifies to [210]

$$\dot{Q}_i = \frac{2}{e^2R_\mathrm{T}}\int_{-\infty}^{\infty}\int_{-\infty}^{\infty} dEdE' n_1(E)n_2(E')E_i f_1(E)\left[1 - f_2(E')\right]P(E - E'), \tag{8.4}$$

where $E_1 = E$ and $E_2 = -E'$. At $V = 0$, the heat transport is only due to fluctuations in the environment if $T_1 = T_2$. On the other hand, $E_i = E' - E$ for heat extracted from the environment, manifesting the conservation of energy. An important special case is the NIS junction, with a BCS DoS with energy gap Δ in S and approximately constant DoS in N near E_F.

For a junction in an ohmic environment, the total impedance reads $Z_t(\omega) = R/(1 + i\omega RC)$. The capacitance C contains ideally only the junction capacitance, but any shunt capacitance parallel to the junction and the resistor adds to it. For this $Z_t(\omega)$, the integral in Eq. (2.24) defining the correlation function $J(t)$ can be performed [212]:

$$\begin{aligned} J(t) =& \frac{2}{R_K}\int_0^\infty \frac{d\omega}{\omega}\frac{R}{1+(\omega/\omega_R)^2}\left\{\coth\left(\beta_R\hbar\omega/2\right)\left[\cos\omega t - 1\right] - i\sin\omega t\right\} \\ =& \frac{\rho}{2}\left[\cot(B)(1-e^{-|\tau|}) - \frac{|\tau|}{B} - 2\sum_{n=1}^{\infty}\frac{1-e^{-n\pi|\tau|/B}}{n\pi\left[1-(n\pi/B)^2\right]} - i\,\mathrm{sign}(\tau)(1-e^{-|\tau|})\right]. \quad (8.5) \end{aligned}$$

Here $\omega_R = 1/(RC)$, $\rho = R/R_Q$ with $R_Q = \hbar/e^2 = R_K/(2\pi)$, $\tau = \omega_R t$, and $B = \beta_R\hbar\omega_R/2$. In the calculation of $P(E)$ we rely mainly on numerical methods. However, for large values of R with $\rho/2 \gg \beta_R E_C$, where $E_C \equiv e^2/(2C)$ is the elementary charging energy of the junction, a simple expression is available [56]: $P(E) = \exp[-(E-E_C)^2/(2\sigma)]/\sqrt{2\pi\sigma}$ with $\sigma = s^2 = 2E_C k_B T_R$. Lowering R transforms $P(E)$ from such a Gaussian around $E = E_C$ towards a delta-function at $E = 0$.

In **X**, $\dot{Q}_N$ in various environments and possibilities for its experimental observation are analyzed in detail, extending the analysis of Ref. [210]. Also the entropy production in the system of the NIS junction and the resistor (neglecting couplings to phonons) is considered. As summarized below, we find that the noise-induced Brownian refrigeration effect is predicted to occur both in a single NIS junction and a two-junction SET configuration. In the latter case, charging effects become relevant as well. It can be realized in a standard on-chip configuration. We have performed preliminary experiments to observe the effect, but further optimization of the circuit and junction parameters is required.

8.1 Results for an NIS junction

In Fig. 8.2 (a) we compare the numerically calculated cooling powers $\dot{Q}_N$ for $R = 10R_K$ and $R = 0.5R_K$ as a function of T_R/T_N at various charging energies $E_C = e^2/(2C)$. The temperatures are fixed to $k_B T_N = k_B T_S = 0.1\Delta$. We find $\dot{Q}_N > 0$ in a large temperature range $T_N < T_R < T_R^{max}$, indicating refrigeration of the normal metal. The maximum cooling power, $\dot{Q}_N^{opt}$, depends on the resistance in a somewhat peculiar way, whereas the corresponding optimum resistor temperature $T_R^{opt}/T_N \simeq \Delta/E_C$ is sensitive mainly to the capacitance. For $\Delta > E_C$ better cooling power is obtained with large environmental resistances whereas for $\Delta \lesssim E_C$ the larger cooling power is found with $R = 0.5R_K$. Above a certain circuit-dependent temperature where $T_R > T_R^{max}$ the N island tends to heat up [$\dot{Q}_N < 0$], which happens non-trivially also in the regime $T_R < T_N$, i.e., heat flows into the "hot" normal metal island. Moreover, Fig. 8.2 (b) shows the heat flow $\dot{Q}_S$ out of the

S electrode under conditions similar to Fig. 8.2 (a). This time, the superconductor cools [$\dot{Q}_S > 0$] when also the resistor is cooled [$T_R < T_N, T_S$], for example by voltage-biased NIS junctions. The S cooling might be easier to observe experimentally when it comes to problems caused when the resistor is heated to a high temperature $T_R \simeq T_C \gg T_N$, required to obtain a large heat extraction $\dot{Q}_N$ out of the N island. On the other hand, probing the S temperature is more complicated, and the electrode has to be kept small and thermally isolated. In addition, the powers $\dot{Q}_S$ are generally smaller than $\dot{Q}_N$, and the S cooling might be hard to distinguish from direct photonic cooling [179] in response to cooling the resistor.

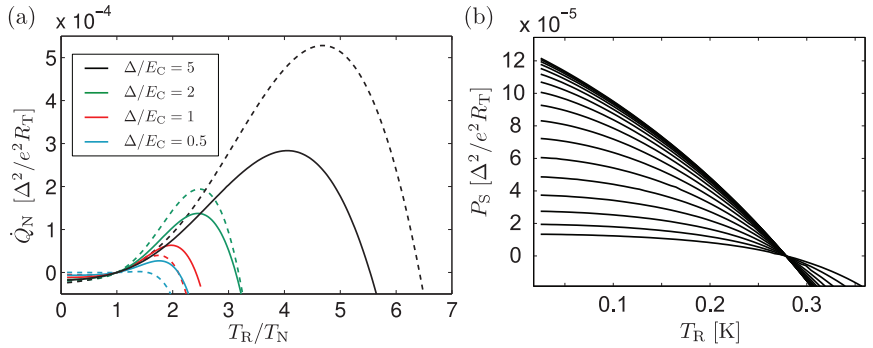

Figure 8.2: (a) Cooling power $\dot{Q}_N$ for $R = 10R_K$ (dashed lines) and $R = 0.5R_K$ (solid) at various values of Δ/E_C. (b) The heat flow $\dot{Q}_S$ out of the S electrode as a function of T_R, at $k_B T_N = k_B T_S = 0.12\Delta$ and $\Delta/E_C = 10$ for R/R_K ranging from 10 (top) to 0.01 (bottom).

In Fig. 8.3 (a) we plot the maximum cooling power and the corresponding resistor temperature as a function of the circuit parameters R and C. As evident also in Fig. 8.2 (a), for small junctions with $\Delta \lesssim E_C$ the cooling power is maximized at finite values of R. T_R^{opt} increases approximately linearly with Δ/E_C. Figure 8.3 (b) shows further how $\dot{Q}_N^{opt}$ depends strongly on $k_B T_N/\Delta$, which was kept fixed in panel (a).

8.2 Noise cooling in two junction SINIS with Coulomb interaction

Instead of a single NIS junction, in this section we analyze the refrigeration effect in a two junction SINIS configuration, i.e., a hybrid single electron transistor with a small N island connected to superconducting leads via two tunnel junctions of the NIS type. Figure 8.4 (a) shows such a structure coupled to a general environment and the various tunneling rates in the system. The two junctions have resistances $R_{T,i}$ and capacitances C_i ($i = 1, 2$). We calculate numerically the total heat flux out of the island and take into account the non-zero charging energy of the system, leading to the quantization of the

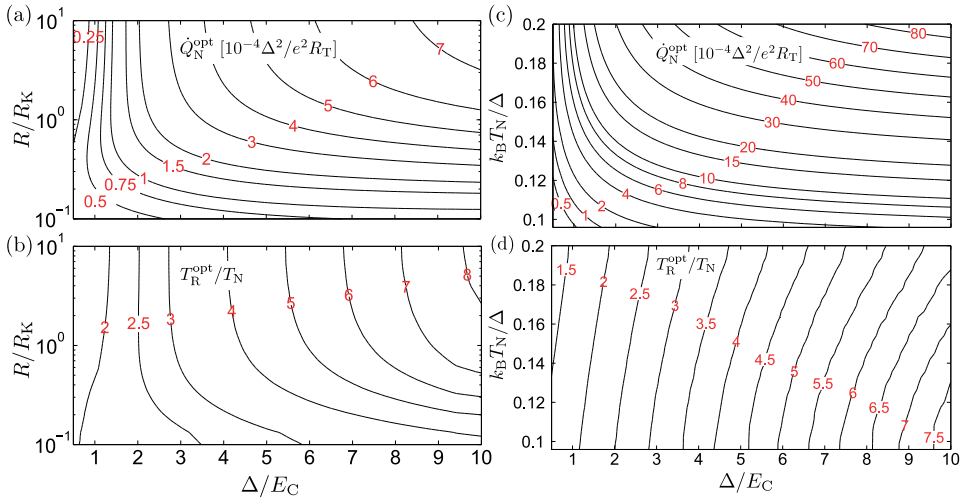

Figure 8.3: (a) Maximum cooling power $\dot{Q}_N^{opt}$ and (b) the corresponding optimum resistor temperature T_R^{opt} (bottom) as a function of R and E_C at $k_BT_N = k_BT_S = 0.1\Delta$. T_R^{opt} increases approximately linearly as a function of Δ/E_C, and starts to become independent of R at $R \gtrsim R_K$. (c),(d) Same as (a),(b), but at a fixed $R = R_K$ as a function of T_N and E_C (assuming $T_N = T_S$).

island charge. We assume charge equilibrium to be reached before each tunneling event, so that the state of the system can be characterized by n, the number of excess electrons on the island. The favored n can be controlled by the gate voltage V_g coupled capacitively to the island via C_g. We assume the gate capacitance C_g to be much smaller than the junction capacitances but the voltage V_g to be large enough so that the only effect of the gate is an offset $n_g = C_gV_g/e$ to the island charge.

Starting from the total Hamiltonian, tunneling rates for the full two junction system can be calculated systematically in second order perturbation theory [56]. However, to make use of the results for a single junction in a general environment, we follow Refs. [56] and [211] and utilize circuit theory to transform the two junction circuit of Fig. 8.4 (a) into an effective single junction circuit. In the following we neglect cotunneling effects and assume the tunneling events to be uncorrelated, so that the other junction can be viewed simply as a series capacitor. Concentrating on tunneling in junction 1, the upper half of Fig. 8.4 (b) displays the circuit of Fig. 8.4 (a) as seen from junction 1. The result of applying Norton and Thevenin network transformations [56] to this circuit is shown in the lower half: Firstly, it consists of an effective impedance $\kappa_1^2 Z_t(\omega)$ where $Z_t(\omega)$ is as in Eq. (2.24), but in terms of the series capacitance $\tilde{C} = C_1C_2/(C_1 + C_2)$, i.e., $Z_t(\omega) = 1/(i\omega\tilde{C}+Z^{-1}(\omega))$. The reduction factors $\kappa_i = \tilde{C}/C_i < 1$, $(i = 1, 2)$ clearly demonstrate the weakened effect of the external impedance $Z(\omega)$ due to shielding by the second junction capacitance. In addition, the transformed circuit contains a capacitance $C_1 + C_2$ and

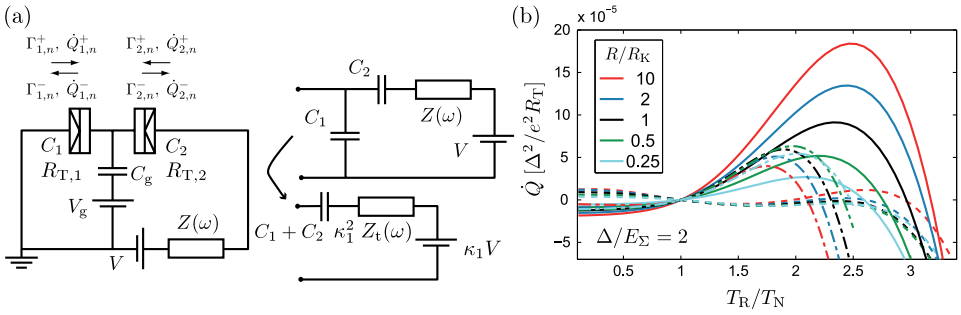

Figure 8.4: (a) Left: Hybrid single electron transistor in the presence of an environment, modeled as an impedance $Z(\omega)$ in series with the bias voltage source V. A gate voltage V_g is coupled capacitively to the N island via C_g. The arrows define tunneling rates and heat fluxes for each of the two NIS junctions. Right: Transformation of the environment seen from junction 1 into an effective single junction circuit. (b) Noise-induced cooling power $\dot{Q}$ in a hybrid SET structure with $\Delta/E_\Sigma = 2$ for different environment impedances R/R_K. Solid lines correspond to $n_g = 0.5$ ("gate open") and dashed lines to $n_g = 0$ ("gate closed"). Dash-dotted lines show the cooling power of a single NIS junction.

a voltage source with voltage $\kappa_1 V$ in series with the impedance $\kappa_1^2 Z_t(\omega)$. The series capacitance does not influence the real part of the total external impedance, and for Brownian refrigeration also the voltage can be set to zero in the end. The effective circuit for junction 2 is identical, except κ_1 is replaced by κ_2 and the voltage V is inverted.

In terms of the effective circuit, one can write down the tunneling rates $\Gamma^\pm_{i,n}$ for the process + (−) of tunneling from (into) the S electrode into (out of) the N island through junction $i = 1, 2$ with the island in charge state n. We have

$$\Gamma^+_{i,n} = \frac{1}{e^2 R_{T,i}} \int_{-\infty}^{\infty}\int_{-\infty}^{\infty} dE' dE n_S(E') f_S(E')[1 - f_N(E)] P(\kappa_i, E' - E - \delta E^+_{i,n}) \qquad (8.6)$$

and

$$\Gamma^-_{i,n} = \frac{1}{e^2 R_{T,i}} \int_{-\infty}^{\infty}\int_{-\infty}^{\infty} dE' dE n_S(E) f_N(E')[1 - f_S(E)] P(\kappa_i, E' - E - \delta E^-_{i,n}). \qquad (8.7)$$

Here, the function $P(\kappa_i, E)$ is defined by

$$P(\kappa_i, E) = \frac{1}{2\pi\hbar} \int_{-\infty}^{\infty} dt \exp\left[\kappa_i^2 J(t) + iEt/\hbar\right], \qquad (8.8)$$

taking into account the reduced environmental coupling in the two junction system. $J(t)$ in Eq. (8.8) is identical to the single junction case, expect the capacitance in $Z_t(\omega)$ is now $\tilde{C}$. Moreover, in Eqs. (8.6) and (8.7) the charging energy penalties for tunneling read

$$\delta E^\pm_{i,n} = \pm 2E_\Sigma(n - n_g \pm 1/2) \pm eV_i \qquad (8.9)$$

with the charging energy $E_\Sigma \equiv e^2/2C_\Sigma$ and $C_\Sigma = C_1 + C_2$ denoting the total capacitance of the island. Finally, V_i is the effective voltage across junction i, i.e., $V_1 = \kappa_1 V$, and $V_2 = -\kappa_2 V$. The first term in Eq. (8.9) originates from the difference in the electrostatic charging energies of the capacitors before and after the tunneling event, whereas the latter term is the work done by the effective voltage sources in transferring the charge. In the zero temperature limit in a low impedance environment, the energy difference has to be negative for the particular rate to be finite. It is notable that neglecting charging effects (or at $n_g = 1/2$), in the important special case of $Z(\omega) = R$ and identical junctions ($R_{T,1} = R_{T,2} = R_T$, $C_1 = C_2 = C$), we can directly apply the analysis of Ch. 2.3 to the double junction rates if the resistance is replaced with $R^* = R/4$ and the capacitance with $C^* = 2C$.

Analogously to the rates $\Gamma^{\pm}_{i,n}$ we introduce the heat fluxes

$$\dot{Q}^+_{i,n} = \frac{1}{e^2 R_{T,i}} \int_{-\infty}^{\infty}\int_{-\infty}^{\infty} dE' dE E n_S(E') f_S(E')[1 - f_N(E)] P(E' - E - \delta E^+_{i,n}) \tag{8.10}$$

$$\dot{Q}^-_{i,n} = \frac{1}{e^2 R_{T,i}} \int_{-\infty}^{\infty}\int_{-\infty}^{\infty} dE' dE E' n_S(E) f_N(E')[1 - f_S(E)] P(E' - E - \delta E^-_{i,n}). \tag{8.11}$$

The total heat flux out from the island by all the tunneling processes is then given by

$$\dot{Q} = \sum_{i=1}^{2} \sum_{n=-\infty}^{\infty} p(n)(\dot{Q}^-_{i,n} - \dot{Q}^+_{i,n}), \tag{8.12}$$

where $p(n)$ denote the probabilities of having n extra electrons on the island. They are determined by the master equation

$$\dot{p}(n) = p(n+1)(\Gamma^-_{1,n+1} + \Gamma^-_{2,n+1}) + p(n-1) \times (\Gamma^+_{1,n-1} + \Gamma^+_{2,n-1}) - p(n)(\Gamma^+_{1,n} + \Gamma^+_{2,n} + \Gamma^-_{1,n} + \Gamma^-_{2,n}). \tag{8.13}$$

We are interested only in the steady state behavior, in which case the probabilities obey the detailed balance condition $p(n)(\Gamma^+_{1,n} + \Gamma^+_{2,n}) = p(n+1)(\Gamma^-_{1,n+1} + \Gamma^-_{2,n+1})$. The probabilities $p(n)$ for $|n| > 0$, in terms of $p(0)$, can be determined numerically by simple up or down iteration of this formula, followed by the normalization $\sum_{n=-\infty}^{\infty} p(n) = 1$.

Figure 8.4 (b) displays the total cooling power $\dot{Q}$ out of the N island as a function of T_R/T_N for various values of the resistance R/R_K and the gate charge n_g, at a fixed charging energy E_Σ. We assume a symmetric SET with $R_{T,1} = R_{T,2} = R_T$ and $C_1 = C_2 = C$. As expected, in a SINIS with large junctions ($\Delta/E_\Sigma \gtrsim 5$) the charging effects have only a small effect on the cooling power, becoming negligible for $\Delta/E_\Sigma \gtrsim 10$. In contrast, with small junctions ($\Delta/E_\Sigma \lesssim 2$) the cooling power is strongly modulated by the gate. The modulation is periodic with the period of $1e$, and the curves are symmetric around $n_g = 0.5$. As a consequence of rescaling the circuit parameters ($R^* = R/4, C^* = 2C$) in the SINIS configuration, better cooling power per junction is achieved, in general, with a single NIS junction when compared to SINIS with two junctions of the same size. High charging energies $\Delta/E_\Sigma \lesssim 2$ pose an exception to this principle: greater cooling power per junction can be reached in a SINIS circuit. In the "gate closed" position ($n_g = 0$,

maximum Coulomb blockade in a voltage biased SET) we find nontrivial solutions for the heat fluxes for small junctions. In the SINIS with $\Delta/E_\Sigma = 2$, the gate voltage can reverse the heat fluxes instead of only suppressing them close to zero in the "gate closed" position.

Discussion

In **X** we calculate the cooling power in various environments in the NIS and SINIS configurations. In addition, we extend the analysis of [210] of the coupling and heat balance for an experimental observation of the cooling effect. Taking into account for example direct photonic coupling between the heated resistor and the N island, the effect remains feasible to detect with standard NIS thermometry. With realistic circuit parameters, temperature drops in excess of 10 mK due to the noise cooling are predicted. According to our preliminary measurements and in agreement with earlier experiments [213, 214], a heating power $P_{\rm ext} \simeq 100$ pW $-$ 1 nW applied to an on-chip thin film resistor can result in overheating of the island to an extent clearly exceeding any heat extraction $\dot{Q}_{\rm N}$. Minimizing the resistor volume while retaining $R \gtrsim R_{\rm K}$, and a capacitive coupling between the resistor and the junction are likely required to reduce the power $P_{\rm ext}$ and qp heat conduction along the superconducting lines.

Chapter 9

Magnetic-field enhancement of quasiparticle relaxation

In Sec. 2.3 we considered the electronic cooling in an SINIS structure by qp tunneling. In Sec. 7.1 it became evident that the observed cooling powers $\dot{Q}_{\rm N}$ were considerably smaller than the basic prediction of Eq. (2.33). This demonstrates how the performance of practical SINIS refrigerators depends crucially on the relaxation of the qps that are injected into the S electrode [71, 215]. The superconductor overheating diminishes the cooling power at the junction because of enhanced qp backtunneling and heating from recombination phonons. The excess qp density close to the junction can be reduced by fabricating the S electrodes very thick [71] and minimizing the resistivity. This is, however, difficult to achieve with shadow-evaporated junctions. Alternatively the S leads can be covered partially by a layer of normal metal that acts as a qp trap [216]. The qp population¡ is typically modeled in terms of a diffusion equation, describing their recombination and other loss mechanisms [205, 217, 218]. Converting the excess density into an effective qp temperature $T(x)$, one finds that at phonon temperatures $k_{\rm B}T \ll \Delta$ the S leads can be overheated on a length scale of at least tens of microns, as the electron-phonon relaxation and electronic heat conduction are exponentially suppressed compared to their normal state values [127, 219].

In **XI** we report an initially counterintuitive observation: the cooling power of an SINIS structure increases in small applied perpendicular magnetic fields $B_\perp \simeq 100\ \mu{\rm T} = 1$ G. The improvement is unexpected, as in general the effect of a magnetic field is to suppress superconductivity, e.g., via increased pair breaking. We explain it in terms of faster qp relaxation within the S electrodes as a result of enhanced inelastic qp scattering in regions where the energy gap is suppressed in magnetic vortices. We measured several structures similar to the one in Fig. 9.1 (a), and the same qualitative behavior was observed in all structures with the same geometry. Here we show data from three samples, fabricated at different times. A Cu island of area $\mathcal{A}_{\rm N}$ and thickness $d_{\rm N}$ is contacted by four overlap-type Al/AlOx/Cu NIS junctions to the Al leads of thickness $d_{\rm S}$. The two large junctions (each with resistance $R_{\rm T}$) at the ends of the island are utilized as a voltage-biased SINIS refrigerator, whereas the two smaller junctions in the middle function as thermometers.

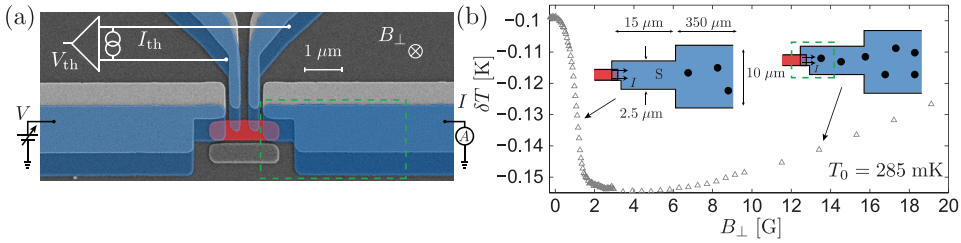

Figure 9.1: (a) SEM micrograph of a typical structure, together with the measurement scheme. A Cu island (red) is contacted to four superconducting Al electrodes (blue) via Al oxide tunnel barriers for thermometry and temperature control. (b) Maximum temperature drop δT in the optimally voltage biased SINIS cooler (sample III) in a perpendicular magnetic field $B_\perp$, at the bath temperature $T_0 = 285$ mK. The sketches show the S electrode geometry and qualitative vortex configurations at $B_\perp \lesssim 2$G and at a value of $B_\perp$ beyond the optimum point. The area inside the green dashed rectangle corresponds to that in the micrograph to the left.

Cu replicas of the Al leads form large area tunnel junctions by partly covering the Al layer, serving as qp traps [216]. I vs. V and $V_{\rm th}$ vs. V -characteristics are measured for a range of bath temperatures T_0 and perpendicular magnetic fields $B_\perp$.

Figure 9.1 (b) shows a typical measured field dependence of the maximum electronic temperature drop δT, relative to a starting bath temperature $T_0 = 285$ mK (sample III). The corresponding optimum cooler bias $V_{\rm opt}$ is plotted below in Fig. 9.2 (c). The cooling enhancement is symmetric in the applied field. The largest δT is reached in a certain field when vortices penetrate into the S electrodes, but not in the immediate vicinity of the junction overlap area. The creation of magnetic vortices [220] has been shown to enhance qp relaxation in superconducting aluminum, as the qps become trapped and thermalize in the regions of reduced energy gap [221]. In **XI** we demonstrate how this additional relaxation channel improves the electronic cooling in NIS junctions. As sketched in Fig. 9.1 (b), in higher fields the vortices move closer to the junction, and the cooling power deteriorates.

The solid lines in Fig. 9.2 (a) show the measured $T_{\rm N}$ of sample III as a function of V at representative bath temperatures T_0 between 0.1 and 0.5 K, in zero field (red) and at $B_\perp = 3$ G (blue). The strong influence of small $B_\perp$ on the cooling is evident: At $eV \simeq 2\Delta$ the maximum cooling $\delta T = T_{\rm N,min} - T_0$ at each T_0 increases by several tens of percents, along with a considerable increase of the optimum bias voltage $V_{\rm opt}$ ("effective gap") and diminished heating at $V > V_{\rm opt}$. This behavior is directly reflected by the cooler IV characteristic in Fig. 9.2 (b). In Ref. [221] with large area NIS junctions, the increased sub-gap conductance at small $B_\perp$ could be directly associated with the fraction of vortices in the junction area. In contrast, we do not observe an increase in the cooler junction sub-gap current in the small fields. The thermometer junctions with narrower S electrodes are not considerably affected in fields $B_\perp \lesssim 10$ G even at bias voltages close to

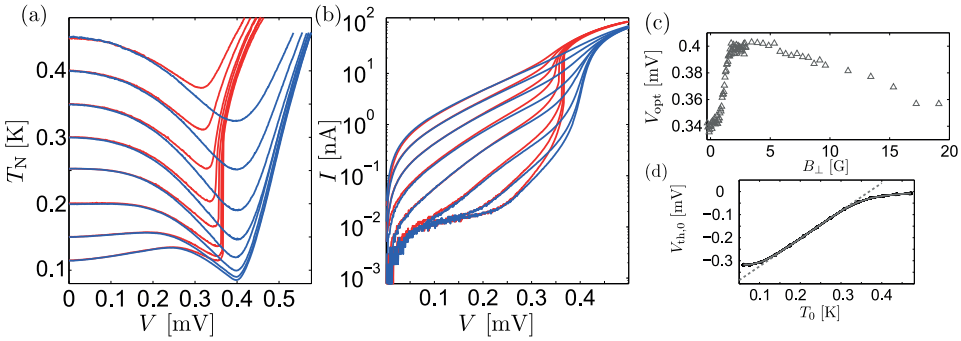

Figure 9.2: (a) Temperature T_N of the N island and (b) cooler SINIS IV characteristic at several bath temperatures T_0 as functions of the cooler bias V, in zero field (red) and $B_\perp = 3$G (blue) for sample III, i.e., the one in Fig. 9.1. (c) Field-dependence of the optimum cooler bias voltage V_{opt} corresponding to δT in Fig. 9.1 (b). (d) Typical calibration of the SINIS thermometer voltage $V_{th,0}$, i.e., V_{th} at $V = 0$ in the absence of electronic cooling, against T_0 (sample II). The black symbols connected by black lines plot the calibration at various values of $B_\perp$ between 0 and 10 G, displaying negligible difference. The gray solid line shows the average behavior, and the gray dashed line a linear approximation for intermediate T_0. T_N saturates below $T_0 \simeq 100$ mK due to parasitic heating.

2Δ, indicating that vortices exist only further away from these junctions. This is evident in the thermometer calibration curves in Fig. 9.2 (d), measured at several fields between 0 and 10 G.

The improved refrigeration is summarized in Fig. 9.3 (a), where we plot the T_0-dependent relative minimum temperature in zero field and close to optimum $B_\perp$ for the three samples. Sample I with the largest R_T performs best in the absence of external fields, and shows the least improvement in the optimum $B_\perp$. Sample II displays the strongest enhancement in the optimum field, whereas sample III with the smallest R_T has the largest cooling effect at $T_0 \gtrsim 0.3$ K. The lines in Fig. 9.3 (b) follow the thermal model discussed below and in **XI**, based on calculating an effective superconductor temperature $T_S = T(0)$ at the junction from a solution of the diffusion equation for the excess qp density.

The thin-film Al leads behave as a type II superconductor, so that $B_\perp$ penetrates in the form of vortices [3]. As shown partially in Fig. 9.1 (a) and sketched in Fig. 9.1 (b), the S leads of the cooler junctions have an initial width of approximately 1 μm. At a distance of 1 μm away from the island, they widen to 2.5 μm width and continue for 15 μm before again widening to 10 μm width and connecting to large-area bonding pads further 350 μm away. Similarly, the thermometer junction leads start at $200 - 400$ nm wide for the first 2 μm, and continue at 1.5 μm over the following 25 μm. The first critical field in the thin film leads is considerably reduced compared to the value $H_{c1} \lesssim 100$ G for bulk Al. Taking an approximate demagnetization factor into account, we can conclude that the initial drop

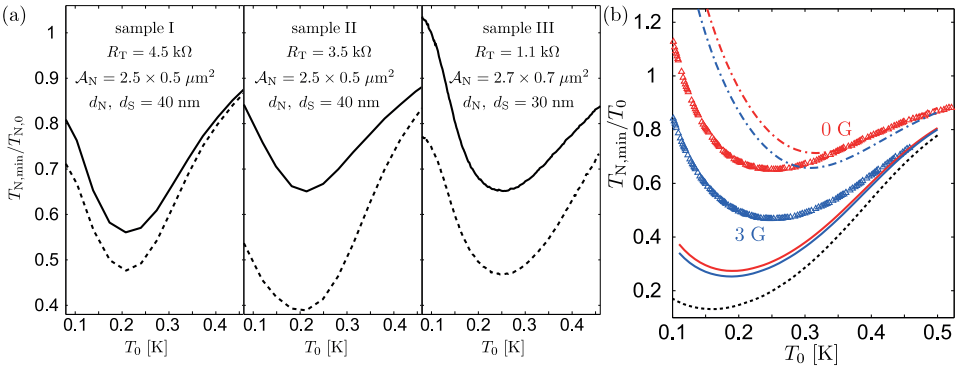

Figure 9.3: (a) Relative minimum temperature in zero field (solid lines) and at $B_\perp \simeq 3$ G close to the optimum field (dashed lines) for samples I-III. (b) $T_{N,min}/T_0$ for sample III in zero field (red symbols) and at $B_\perp \simeq 3$ G (blue symbols), but now including lines showing the calculated temperature reduction assuming different degrees of thermalization of the qps in the S electrodes, and the N island phonons.

in δT in Fig. 9.1 (a) observed below 1 G is consistent with a rough estimate for the field at which vortex penetration begins in the 2.5 μm wide Al section.

In a range of $B_\perp$ between the red and the blue curves in Fig. 9.2 (a), the cooling curves exhibit hysteretic behavior in the bias voltage V, and a third branch develops at $V > V_{opt}$. In Fig. 9.4 we plot in detail how the T_N vs. V characteristic of sample III changes at $T_0 \simeq 175$ mK as $B_\perp$ is stepped up from zero, clarifying this transition. The same feature occurs when the cooler is current biased. At a fixed $B_\perp$, the switchings in T_e (and simultaneously in I) happen randomly around certain values of V. The origin of this effect is not clear, but it can be related to a combination of overheating effects not captured by our simple thermal model, and asymmetry of the two junctions in the SINIS. Similar to Ref. [222], magnetic hysteresis appears as well, when $B_\perp$ is stepped to high enough values, typically above 10 G for the geometry of Fig. 9.1. Figure 9.4 (d) shows the effect as the field is stepped further (gray lines), and then reduced back (red): In decreasing field $B_\perp \simeq 10$ G, the cooling disappears completely and also the thermometer junctions are affected. When $B \simeq 5$ G, the improved cooling is abruptly restored. We observed the cooling enhancement also with Ag as the normal metal, in the two-island structures of Sec. 7.1, in single NIS junctions with various gradually widening lead geometries close to the junction, and in a parallel field. In the last case, the required fields were larger by an order of magnitude and dependent on the field orientation in the sample plane.

In our thermal model for the improved cooling **XI**, we assume quasiequilibrium conditions and solve for the temperature profile in the S leads simultaneously with T_N. The nonequilibrium regime has been analyzed, e.g., in [223]. As the relevant thermalization mechanism in the leads we consider the heat flow into the large-area NIS trap junction. The vortices are included as a normal fraction r beyond 15 μm away from the junction,

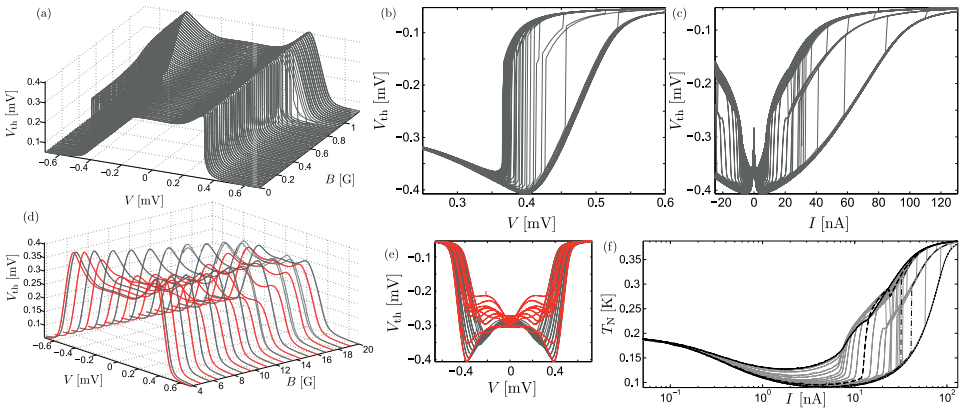

Figure 9.4: Detailed evolution of the electronic cooling in sample III at a fixed T_0. The cooler bias was swept back and forth while the magnetic field was changed in steps. (a) Thermometer voltage $V_{\rm th}$ as a function of the cooler bias voltage V and the magnetic field $B_\perp$, in low fields. (b) Selected $V_{\rm th}$ vs. V curves from (a) in 2D. (c) Similar to (b), but for the cooler operated under current bias I. (d) $V_{\rm th}$ as a function of V and $B_\perp$ in larger fields, for increasing field magnitude (gray lines) and decreasing field (red lines). (e) The curves of (d) in 2D. (f) Some of the curves of (c) converted to electron temperature and plotted on a semilogarithmic scale. In increasing field, the zero-field behavior (solid black line) changes via the dashed and dash-dotted curves to the black dotted curve, measured slightly past the optimum field.

giving an exponentially larger contribution to the heat flow. In Fig. 9.3 (b) we plot the calculated maximum cooling in the two extreme cases of $r = 0$ and $r = 1$ as the red and blue solid lines, with realistic values $\rho = 3.5$ $\mu\Omega$cm for the Al resistivity and $R_0 = 1$ k$\Omega(\mu$m$)^2$ for the trap specific resistance. An order of magnitude change in these values would be required to change considerably the predicted cooling. A finite normal fraction is seen to improve the cooling, but the difference is small and the starting level at $r = 0$ is much closer to the ideal limit $T_{\rm S} = T_0$ than in the measurement. We attribute the difference to the neglect of phonon overheating in the N island. The dash-dotted lines show the worst-case scenario $T_{\rm ph} = T_{\rm S}$. The observed cooling can be explained if $T_{\rm ph}$ overheats from approximately 80% of $T_{\rm S}$ at $T_0 = 0.1$ K and to $\gtrsim 95\%$ at $T_0 = 0.5$ K, approaching T_0 as T_0 increases. At the relatively large powers $\simeq 100$ pW at the optimum bias due to low $R_{\rm T}$, phonon overheating is relevant especially as large part of the island is located on top of the overheated S leads [214]. Notably, the large field-induced improvement evident in Figs. 9.1 and Fig. 9.2 is observed because of the considerable S electrode overheating in zero field. It explains also the significant increase in $V_{\rm opt}$ as $B_\perp$ is increased from zero: $V_{\rm opt}$ is close to the ideal value $2(\Delta - 0.66 k_{\rm B} T_{\rm N})/e$ only at optimum $B_\perp$. In terms of a phenomenological parameter $\beta \ll 1$ [71, 204], assuming $T_{\rm S} = T_0$ but reducing the cooling power per junction by $-\beta \dot{Q}_{\rm S}$, an agreement within 10% for $T_0 \geq 0.1$ K can be reached

with $\beta = 0.08$ in zero field and $\beta = 0.04$ in the optimum field.

To confirm the role of the S electrode geometry we performed additional experiments on parallel SINIS coolers. As shown in Fig. 3 of **XI**, in a sample with initially wide leads, vortices form first close to the junctions, and applying $B_\perp$ monotonously weakens the cooling. In contrast, with narrow leads close to the junctions, similar to Fig. 9.1 (a), the cooling is optimized at a finite $B_\perp$. To utilize the increased scattering at the vortices, several relatively narrow junctions with gradually widening leads would therefore seem preferable to a single large-area junction with a wide S electrode. As a by-product, this results in increased field tolerance and less sensitivity to flux noise from vortex motion.

Chapter 10

Conclusions

In this thesis various hybrid circuits were investigated in the temperature range 50 – 500 mK. Tunnel junctions with highly nonlinear electrical characteristics were used as threshold detectors of current, probes of the quasiparticle density of states, or as electron thermometers and refrigerators. The experiments demonstrate the strong influence of electrical fluctuations on mesoscopic devices, and the intricate connection between charge and heat transport.

A hysteretic Josephson junction was shown to be sensitive to the non-Gaussian current noise generated by another on-chip tunnel junction, probing the fluctuations over a large bandwidth determined by the plasma frequency. The dominant effect is due to the second moment of the shot noise, described by an increased effective temperature for escape by thermal activation. A finite third moment leads to a small asymmetry of the detector escape rates for opposing polarities of the noise source bias. With a suitable design of the on-chip electromagnetic environment [154], the Josephson threshold detection described in terms of the classical theory [157] is a viable method for quantitatively probing the second and third order fluctuations in a range of mesoscopic conductors once calibrated against the shot noise from a tunnel junction. Further progress can be envisioned, as a full theoretical model for the low temperature quantum limit and the crossover region has not yet been developed. Moreover, the method is yet to be demonstrated for example in detecting the noise of a quantum point contact or an atomic point contact junction, or to probe finite-frequency higher order effects.

Electron overheating in the normal metal turned out to be a significant cause of hysteretic behavior in proximity Josephson junctions, as shown by local electronic thermometry. At low temperatures the effect is expected to be relevant also in weak links formed from various other materials. In a closely related loop geometry, magnetic field sensing was demonstrated based on tunnel probing the flux-dependent density of states of the proximity wire. The SQUIPT-interferometer combines the low dissipation of the NIS junctions with the tunability of proximity structures. With low-temperature readout electronics, the intrinsic flux sensitivity is expected to be suitable for the detection of small magnetic moments, ultimately just a few electron spins [26].

Thermal conductance of short superconducting wires with the length of the order of the

coherence length was measured to be strongly enhanced compared to longer wires where the inverse proximity effect is negligible. A low-temperature crossover from above-gap to sub-gap heat conduction was observed, in agreement with the quasiclassical theory in the diffusive limit. The measurement setup can be used to study thermoelectric phenomena also in other mesoscopic systems, e.g., to investigate the thermopower and thermal conductance of a metallic single-electron transistor [209]. Fully normal and hybrid tunnel junctions can be reliably combined onto a single circuit with the introduced fabrication technique, based on the lateral suppression of superconductivity. Another task is to test recent predictions of nonequilibrium heat exchange between a normal tunnel junction and its electrical environment [224], relevant also for the realization of a Brownian refrigerator. Theoretical analysis shows Brownian refrigeration by hybrid tunnel junctions to be experimentally feasible, based on NIS junctions as well-characterized building blocks. Coupling of off-chip electromagnetic radiation to the junction is to be reduced in further experiments. Similarly, strongly coupled environments or junctions with lower resistance deserve more study as the perturbative theory no longer holds.

Finally, vortex formation in small magnetic fields was shown to significantly enhance quasiparticle relaxation in a nonequilibrium superconductor, improving the achievable temperature reduction in an NIS cooler. Better understanding of the relaxation mechanisms is important towards the long-term goal of realizing a general solid-state cooling platform [215, 225, 226] for detector applications with optimum performance.

Bibliography

[1] P. G. de Gennes, *Superconductivity of metals and alloys* (W. A. Benjamin, 1966).

[2] K. K. Likharev, *Dynamics of Josephson Junctions and Circuits*, 1st ed. (Gordon and Breach, 1996).

[3] M. Tinkham, *Introduction to Superconductivity*, 2nd ed. (McGraw-Hill, 1996).

[4] Y. M. Blanter and M. Büttiker, Phys. Rep. **336**, 1 (2000).

[5] Y. V. Nazarov, *Quantum Noise in Mesoscopic Physics*, *NATO Science Series in Mathematics*, 1st ed. (Kluwer, 2003).

[6] S. Kogan, *Electronic Noise and Fluctuations in Solids*, 1st ed. (Cambridge University Press, 1996).

[7] H. K. Onnes, Leiden Comm. **120b, 122b, 124c**, (1911).

[8] P. W. Adams, Phys. Rev. Lett. **92**, 067003 (2004).

[9] J. Bardeen, L. N. Cooper, and J. R. Schrieffer, Phys. Rev. **108**, 1175 (1957).

[10] J. Bardeen, L. N. Cooper, and J. R. Schrieffer, Phys. Rev. **106**, 162 (1957).

[11] L. N. Cooper, Phys. Rev. **104**, 1189 (1956).

[12] E. Maxwell, Phys. Rev. **78**, 477 (1950).

[13] C. A. Reynolds, B. Serin, W. H. Wright, and L. B. Nesbitt, Phys. Rev. **78**, 487 (1950).

[14] A. Anthore, H. Pothier, and D. Esteve, Phys. Rev. Lett. **90**, 127001 (2003).

[15] K. K. Likharev, Rev. Mod. Phys. **51**, 101 (1979).

[16] T. V. Duzer and C. W. Turner, *Principles of Superconductive Devices and Circuits*, 2nd ed. (Prentice-Hall, 1999).

[17] A. Barone and G. Paterno, *Physics and Applications of the Josephson Effect*, 1st ed. (Wiley, 1982).

[18] B. D. Josephson, Phys. Lett. **1**, 251 (1962).

[19] P. W. Anderson and J. M. Rowell, Phys. Rev. Lett. **10**, 230 (1963).

[20] V. Ambegaokar and A. Baratoff, Phys. Rev. Lett. **10**, 486 (1963).

[21] S. Shapiro, Phys. Rev. Lett. **11**, 80 (1963).

[22] C. A. Hamilton, Rev. Sci. Instr. **71**, 3611 (2000).

[23] J. Kohlmann, R. Behr, and T. Funck, Meas. Sci. Tech. **14**, 1216 (2003).

[24] J. Clarke and A. Braginski, *The SQUID handbook: Applications of SQUIDs and SQUID systems* (Wiley-VCH, 2006), No. v. 1.

[25] R. C. Jaklevic, J. Lambe, A. H. Silver, and J. E. Mercereau, Phys. Rev. Lett. **12**, 159 (1964).

[26] C. P. Foley and H. Hilgenkamp, Supercond. Sci. Technol. **22**, 064001 (2009).

[27] Y. Makhlin, G. Schön, and A. Shnirman, Rev. Mod. Phys. **73**, 357 (2001).

[28] W. C. Stewart, Appl. Phys. Lett. **12**, 277 (1968).

[29] D. E. McCumber, J. Appl. Phys. **39**, 3113 (1968).

[30] R. L. Kautz and J. M. Martinis, Phys. Rev. B **42**, 9903 (1990).

[31] P. Hänggi and G.-L. Ingold, Chaos **15**, 026105 (2005).

[32] H. Grabert, P. Schramm, and G.-L. Ingold, Phys. Rep. **168**, 115 (1988).

[33] H. Grabert, Chem. Phys. **322**, 160 (2006).

[34] P. Hänggi, P. Talkner, and M. Borkovec, Rev. Mod. Phys. **62**, 251 (1990).

[35] E. Pollak and P. Talkner, Chaos **15**, 026116 (2005).

[36] H. Risken, *The Fokker-Planck Equation. Methods of Solution and Applications. Springer Series in Synergetics Vol. 18*, 1st ed. (Springer-Verlag, 1984).

[37] S. Chandrasekhar, Rev. Mod. Phys. **15**, 1 (1943).

[38] U. Weiss, *Quantum Dissipative Systems*, 2nd ed. (World Scientific, 1999).

[39] H. A. Kramers, Physica (Utrecht) **7**, 284 (1940).

[40] A. Larkin and Y. Ovchinnikov, Zh. Eksp. Teor. Fiz. **91**, 318 (1986).

[41] J. M. Kivioja *et al.*, Phys. Rev. Lett. **94**, 247002 (2005).

[42] A. O. Caldeira and A. J. Leggett, Phys. Rev. Lett. **46**, 211 (1981).

[43] A. O. Caldeira and A. J. Leggett, Ann. Phys. **149**, 374 (1983).

[44] H. Grabert, U. Weiss, and P. Hänggi, Phys. Rev. Lett. **52**, 2193 (1984).

[45] H. Grabert, P. Olschowski, and U. Weiss, Phys. Rev. B **36**, 1931 (1987).

[46] W. den Boer and R. de Bruyn Ouboter, Physica (Utrecht) B/C **98**, 185 (1980).

[47] R. J. Prance *et al.*, Nature (London) **289**, 543 (1981).

[48] R. F. Voss and R. A. Webb, Phys. Rev. Lett. **47**, 265 (1981).

[49] L. D. Jackel *et al.*, Phys. Rev. Lett. **47**, 697 (1981).

[50] S. Washburn, R. A. Webb, R. F. Voss, and S. M. Faris, Phys. Rev. Lett. **54**, 2712 (1985).

[51] D. B. Schwartz, B. Sen, C. N. Archie, and J. E. Lukens, Phys. Rev. Lett. **55**, 1547 (1985).

[52] M. H. Devoret, J. M. Martinis, and J. Clarke, Phys. Rev. Lett. **55**, 1908 (1985).

[53] J. M. Martinis, M. H. Devoret, and J. Clarke, Phys. Rev. B **35**, 4682 (1987).

[54] J. P. Pekola *et al.*, Phys. Rev. Lett. **95**, 197004 (2005).

[55] F. Taddei and F. W. J. Hekking, Europhys. Lett. **83**, 47009 (2008).

[56] G.-L. Ingold and Y. V. Nazarov, in *Single Charge Tunneling*, Vol. 294 of *NATO ASI Series B*, eds. H. Grabert and M. Devoret (Plenum Press, 1992), pp. 21–107.

[57] H. Grabert and H. Horner, Z. Phys. B **85**, 317 (1991).

[58] Y. V. Nazarov, Zh. Eksp Teor. Fiz. **95**, 975 (1989), [Sov. Phys. JETP 68, 561 (1989)].

[59] M. H. Devoret *et al.*, Phys. Rev. Lett. **64**, 1824 (1990).

[60] S. M. Girvin *et al.*, Phys. Rev. Lett. **64**, 3183 (1990).

[61] P. Joyez, D. Esteve, and M. H. Devoret, Phys. Rev. Lett. **80**, 1956 (1998).

[62] F. Giazotto *et al.*, Rev. Mod. Phys. **78**, 217 (2006).

[63] J. M. Martinis and M. Nahum, Phys. Rev. B **48**, 18316 (1993).

[64] R. C. Dynes, J. P. Garno, G. B. Hertel, and T. P. Orlando, Phys. Rev. Lett. **53**, 2437 (1984).

[65] J. P. Pekola *et al.*, Phys. Rev. Lett. **92**, 056804 (2004).

[66] J. P. Pekola *et al.*, Phys. Rev. Lett. **105**, 026803 (2010).

[67] J. M. Rowell and D. C. Tsui, Phys. Rev. B **14**, 2456 (1976).

[68] E. L. Wolf, *Principles of Electron Tunneling Spectroscopy* (Oxford University Press, 1985).

[69] M. Nahum, T. M. Eiles, and J. M. Martinis, Appl. Phys. Lett. **65**, 3123 (1994).

[70] M. M. Leivo, J. P. Pekola, and D. V. Averin, Appl. Phys. Lett. **68**, 1996 (1996).

[71] A. M. Clark *et al.*, Appl. Phys. Lett. **84**, 625 (2004).

[72] S. Chaudhuri and I. J. Maasilta, preprint (2011).

[73] F. C. Wellstood, C. Urbina, and J. Clarke, Phys. Rev. B **49**, 5942 (1994).

[74] S. Rajauria *et al.*, Phys. Rev. Lett. **99**, 047004 (2007).

[75] P. G. de Gennes, Rev. Mod. Phys. **36**, 225 (1964).

[76] A. I. Buzdin, Rev. Mod. Phys. **77**, 935 (2005).

[77] W. Belzig *et al.*, Superlattices and Microstructures **25**, 1251 (1999).

[78] C. J. Lambert and R. Raimondi, Journal of Physics: Condensed Matter **10**, 901 (1998).

[79] B. Pannetier and H. Courtois, J. Low Temp. Phys. **118**, 599 (2000).

[80] W. Belzig, C. Bruder, and G. Schön, Phys. Rev. B **54**, 9443 (1996).

[81] S. Guéron *et al.*, Phys. Rev. Lett. **77**, 3025 (1996).

[82] H. le Sueur *et al.*, Phys. Rev. Lett. **100**, 197002 (2008).

[83] N. Moussy, H. Courtois, and B. Pannetier, Europhys. Lett. **55**, 861 (2001).

[84] M. Vinet, C. Chapelier, and F. Lefloch, Phys. Rev. B **63**, 165420 (2001).

[85] F. Zhou, P. Charlat, B. Spivak, and B. Pannetier, J. Low Temp. Phys. **110**, 841 (1998).

[86] D. A. Ivanov, R. von Roten, and G. Blatter, Phys. Rev. B **66**, 052507 (2002).

[87] P. Charlat *et al.*, Phys. Rev. Lett. **77**, 4950 (1996).

[88] H. Courtois *et al.*, J. Low Temp. Phys. **116**, 187 (1999).

[89] P. Dubos *et al.*, Phys. Rev. B **63**, 064502 (2001).

[90] T. T. Heikkilä, J. Särkkä, and F. K. Wilhelm, Phys. Rev. B **66**, 184513 (2002).

[91] J. C. Hammer, J. C. Cuevas, F. S. Bergeret, and W. Belzig, Phys. Rev. B **76**, 064514 (2007).

[92] P. Cadden-Zimansky and V. Chandrasekhar, Phys. Rev. Lett. **97**, 237003 (2006).

[93] S. G. den Hartog *et al.*, Phys. Rev. Lett. **77**, 4954 (1996).

[94] H. Courtois, P. Gandit, D. Mailly, and B. Pannetier, Phys. Rev. Lett. **76**, 130 (1996).

[95] P. Virtanen *et al.*, Phys. Rev. Lett. **99**, 217003 (2007).

[96] P. Dubos, H. Courtois, O. Buisson, and B. Pannetier, Phys. Rev. Lett. **87**, 206801 (2001).

[97] A. F. Andreev, Zh. Eksp. Teor. Fiz. **46**, 1823 (1964), [Sov. Phys. JETP 19, 1228].

[98] P. de Gennes and D. Saint-James, Phys. Lett. **4**, 151 (1963).

[99] G. E. Blonder, M. Tinkham, and T. M. Klapwijk, Phys. Rev. B **25**, 4515 (1982).

[100] C. W. J. Beenakker, Phys. Rev. Lett. **67**, 3836 (1991).

[101] M. A. Sillanpää, T. T. Heikkilä, R. K. Lindell, and P. J. Hakonen, Europhys. Lett. **56**, 590 (2001).

[102] G. Bignon, M. Houzet, F. Pistolesi, and F. W. J. Hekking, Europhys. Lett. **67**, 110 (2004).

[103] G. Falci, D. Feinberg, and F. W. J. Hekking, Europhys. Lett. **54**, 255 (2001).

[104] D. S. Golubev, M. S. Kalenkov, and A. D. Zaikin, Phys. Rev. Lett. **103**, 067006 (2009).

[105] S. Russo, M. Kroug, T. M. Klapwijk, and A. F. Morpurgo, Phys. Rev. Lett. **95**, 027002 (2005).

[106] P. Cadden-Zimansky, Z. Jiang, and V. Chandrasekhar, New Journal of Physics **9**, 116 (2007).

[107] J. Brauer *et al.*, Phys. Rev. B **81**, 024515 (2010).

[108] A. Levy-Yeati, F. S. Bergeret, A. Martin-Rodero, and T. M. Klapwijk, Nature Physics **3**, 455 (2007).

[109] L. Hofstetter, S. Csonka, J. Nygård, and C. Schönenberger, Nature (London) **461**, 960 (2009).

[110] L. G. Herrmann *et al.*, Phys. Rev. Lett. **104**, 026801 (2010).

[111] N. B. Kopnin, *Theory of Nonequilibrium Superconductivity*, 1st ed. (Oxford University Press, 2001).

[112] D. Langenberg and A. Larkin, *Nonequilibrium superconductivity*, *Modern problems in condensed matter sciences* (North-Holland, 1986).

[113] G. Eilenberger, Z. Phys. **214**, 195 (1968).

[114] K. D. Usadel, Phys. Rev. Lett. **25**, 507 (1970).

[115] Y. V. Nazarov, Phys. Rev. Lett. **73**, 1420 (1994).

[116] M. Y. Kuprianov and V. F. Lukichev, Sov. Phys. JETP **67**, 1163 (1988).

[117] P. Virtanen and T. Heikkilä, Appl. Phys. A **89**, 625 (2007).

[118] S.-K. Yip, Phys. Rev. B **58**, 5803 (1998).

[119] J. J. A. Baselmans, Ph.D. thesis, University of Groningen, The Netherlands, 2002.

[120] F. K. Wilhelm, G. Schön, and A. D. Zaikin, Phys. Rev. Lett. **81**, 1682 (1998).

[121] F. Wilhelm, A. Zaikin, and G. Schön, J. Low Temp. Phys. **106**, 305 (1997).

[122] J. J. A. Baselmans, A. F. Morpurgo, B. J. van Wees, and T. M. Klapwijk, Nature (London) **397**, 43 (1999).

[123] J. J. A. Baselmans, T. T. Heikkilä, B. J. van Wees, and T. M. Klapwijk, Phys. Rev. Lett. **89**, 207002 (2002).

[124] A. M. Savin *et al.*, Appl. Phys. Lett. **84**, 4179 (2004).

[125] F. Giazotto *et al.*, Appl. Phys. Lett. **83**, 2877 (2003).

[126] E. V. Bezuglyi and V. Vinokur, Phys. Rev. Lett. **91**, 137002 (2003).

[127] J. Bardeen, G. Rickayzen, and L. Tewordt, Phys. Rev. **113**, 982 (1959).

[128] G. J. Dolan, Appl. Phys. Lett. **31**, 337 (1977).

[129] MicroChem Corp., NANO PMMA and Copolymer, www.microchem.com.

[130] F. Pobell, *Matter and Methods at Low Temperatures*, 3rd ed. (Springer, 2007).

[131] J. Pekola and J. Kauppinen, Cryogenics **34**, 843 (1994).

[132] J. P. Pekola, K. P. Hirvi, J. P. Kauppinen, and M. A. Paalanen, Phys. Rev. Lett. **73**, 2903 (1994).

[133] A. B. Zorin, Rev. Sci. Instr. **66**, 4296 (1995).

[134] J. Salo, F. W. J. Hekking, and J. P. Pekola, Phys. Rev. B **74**, 125427 (2006).

[135] L. S. Levitov and G. B. Lesovik, JETP Lett. **58**, 230 (1993).

[136] L. S. Levitov, H. Lee, and G. B. Lesovik, J. Math. Phys. **37**, 4845 (1996).

[137] Yu.V. Nazarov and M. Kindermann, Eur. Phys. J. B **35**, 413 (2003).

[138] P. Dutta and P. M. Horn, Rev. Mod. Phys. **53**, 497 (1981).

[139] M. B. Weissman, Rev. Mod. Phys. **60**, 537 (1988).

[140] S. Datta, *Electronic Transport in Mesoscopic Systems*, 1st ed. (Cambridge University Press, 1995).

[141] E. Zakka-Bajjani *et al.*, Phys. Rev. Lett. **99**, 236803 (2007).

[142] B. Reulet, J. Senzier, and D. E. Prober, Phys. Rev. Lett. **91**, 196601 (2003).

[143] C. W. J. Beenakker, M. Kindermann, and Y. V. Nazarov, Phys. Rev. Lett. **90**, 176802 (2003).

[144] Y. Bomze *et al.*, Phys. Rev. Lett. **95**, 176601 (2005).

[145] G. Gershon, Y. Bomze, E. V. Sukhorukov, and M. Reznikov, Phys. Rev. Lett. **101**, 016803 (2008).

[146] V. Brosco, R. Fazio, F. W. J. Hekking, and J. P. Pekola, Phys. Rev. B **74**, 024524 (2006).

[147] T. T. Heikkilä and T. Ojanen, Phys. Rev. B **75**, 035335 (2007).

[148] R. Aguado and L. P. Kouwenhoven, Phys. Rev. Lett. **84**, 1986 (2000).

[149] T. T. Heikkilä, P. Virtanen, G. Johansson, and F. K. Wilhelm, Phys. Rev. Lett. **93**, 247005 (2004).

[150] R. K. Lindell *et al.*, Phys. Rev. Lett. **93**, 197002 (2004).

[151] P.-M. Billangeon, F. Pierre, H. Bouchiat, and R. Deblock, Phys. Rev. Lett. **96**, 136804 (2006).

[152] J. Tobiska and Y. V. Nazarov, Phys. Rev. Lett. **93**, 106801 (2004).

[153] J. P. Pekola, Phys. Rev. Lett. **93**, 206601 (2004).

[154] Q. Le Masne *et al.*, Phys. Rev. Lett. **102**, 067002 (2009).

[155] B. Huard, Ann. Phys. (France) **31**, 1 (2006).

[156] B. Huard *et al.*, Annalen der Physik **16**, 736 (2007).

[157] H. Grabert, Phys. Rev. B **77**, 205315 (2008).

[158] J. Ankerhold, Phys. Rev. Lett. **98**, 036601 (2007).

[159] E. V. Sukhorukov and A. N. Jordan, Phys. Rev. Lett. **98**, 136803 (2007).

[160] D. F. Urban and H. Grabert, Phys. Rev. B **79**, 113102 (2009).

[161] T. Novotný, J. Stat. Mech.: Theory and Experiment **2009**, P01050 (2009).

[162] E. V. Sukhorukov and A. N. Jordan, Phys. Rev. Lett. **102**, 086806 (2009).

[163] L. Billings, M. I. Dykman, and I. B. Schwartz, Phys. Rev. E **78**, 051122 (2008).

[164] M. I. Dykman, Phys. Rev. E **81**, 051124 (2010).

[165] A. A. Clerk *et al.*, Rev. Mod. Phys. **82**, 1155 (2010).

[166] T. Ojanen and T. T. Heikkilä, Phys. Rev. B **73**, 020501 (2006).

[167] L. Angers *et al.*, Phys. Rev. B **77**, 165408 (2008).

[168] A. Rogachev, A. T. Bollinger, and A. Bezryadin, Phys. Rev. Lett. **94**, 017004 (2005).

[169] Y.-J. Doh *et al.*, Science **309**, 272 (2005).

[170] P. Spathis *et al.*, Nanotechnology **22**, 105201 (2011).

[171] J. A. v. D. P. Jarillo-Herrero and L. P. Kouwenhoven, Nature (London) **439**, 953 (2005).

[172] J.-P. Cleuziou *et al.*, Nature Nanotech. **1**, 53 (2006).

[173] H. B. Heersche *et al.*, Nature (London) **446**, 56 (2007).

[174] T. A. Fulton and L. N. Dunkleberger, J. Appl. Phys. **45**, 2283 (1974).

[175] W. J. Skocpol, M. R. Beasley, and M. Tinkham, J. Appl. Phys. **45**, 4054 (1974).

[176] Y. Song, J. Appl. Phys. **47**, 2651 (1976).

[177] J. C. Cuevas *et al.*, Phys. Rev. B **73**, 184505 (2006).

[178] J. C. Cuevas and H. Pothier, Phys. Rev. B **75**, 174513 (2007).

[179] A. V. Timofeev *et al.*, Phys. Rev. Lett. **102**, 200801 (2009).

[180] F. Giazotto *et al.*, Appl. Phys. Lett. **92**, 162507 (2008).

[181] J. J. A. Baselmans, B. J. van Wees, and T. M. Klapwijk, Appl. Phys. Lett. **79**, 2940 (2001).

[182] J. J. A. Baselmans, B. J. van Wees, and T. M. Klapwijk, Phys. Rev. B **63**, 094504 (2001).

[183] A. F. Morpurgo, T. M. Klapwijk, and B. J. van Wees, Appl. Phys. Lett. **72**, 966 (1998).

[184] J. Huang *et al.*, Phys. Rev. B **66**, 020507 (2002).

[185] M. S. Crosser, P. Virtanen, T. T. Heikkilä, and N. O. Birge, Phys. Rev. Lett. **96**, 167004 (2006).

[186] M. S. Crosser *et al.*, Phys. Rev. B **77**, 014528 (2008).

[187] F. Giazotto *et al.*, Phys. Rev. Lett. **92**, 137001 (2004).

[188] F. Giazotto *et al.*, J. Low Temp. Phys. **136**, 435 (2004).

[189] J. C. Cuevas and F. S. Bergeret, Phys. Rev. Lett. **99**, 217002 (2007).

[190] J.-D. Pillet *et al.*, Nature Physics **6**, 965 (2010).

[191] F. Giazotto and F. Taddei, arXiv:1103.3598 (2011).

[192] O. Quaranta, P. Spathis, F. Beltram, and F. Giazotto, Appl. Phys. Lett. **98**, 032501 (2011).

[193] M. Möttönen, J. J. Vartiainen, and J. P. Pekola, Phys. Rev. Lett. **100**, 177201 (2008).

[194] T. T. Heikkilä and F. Giazotto, Phys. Rev. B **79**, 094514 (2009).

[195] V. Chandrasekhar, Supercond. Sci. Technol. **22**, 083001 (2009).

[196] D. A. Dikin, S. Jung, and V. Chandrasekhar, Phys. Rev. B **65**, 012511 (2001).

[197] Z. Jiang and V. Chandrasekhar, Phys. Rev. B **72**, 020502 (2005).

[198] Z. Jiang and V. Chandrasekhar, Phys. Rev. Lett. **94**, 147002 (2005).

[199] J. Aumentado *et al.*, Appl. Phys. Lett. **75**, 3554 (1999).

[200] Z. Jiang, H. Lim, V. Chandrasekhar, and J. Eom, Appl. Phys. Lett. **83**, 2190 (2003).

[201] P. Virtanen and T. T. Heikkilä, Phys. Rev. Lett. **92**, 177004 (2004).

[202] A. Brinkman and A. A. Golubov, Phys. Rev. B **74**, 214512 (2006).

[203] M. S. Kalenkov and A. D. Zaikin, Phys. Rev. B **75**, 172503 (2007).

[204] J. N. Ullom and P. A. Fisher, Physica B **284-288**, 2036 (2000).

[205] S. Rajauria, H. Courtois, and B. Pannetier, Phys. Rev. B **80**, 214521 (2009).

[206] P. Virtanen, (2009) (unpublished).

[207] C. C. Chi *et al.*, Phys. Rev. B **50**, 3487 (1994).

[208] W. Liniger, J. Low Temp. Phys. **93**, 1 (1993).

[209] B. Kubala, J. König, and J. Pekola, Phys. Rev. Lett. **100**, 066801 (2008).

[210] J. P. Pekola and F. W. J. Hekking, Phys. Rev. Lett. **98**, 210604 (2007).

[211] H. Grabert *et al.*, Z. Phys. B **84**, 143 (1991).

[212] H. Grabert, G.-L. Ingold, and B. Paul, Europhys. Lett. **44**, 360 (1998).

[213] J. Pleikies *et al.*, Supercond. Sci. Technol. **22**, 114007 (2009).

[214] A. M. Savin, J. P. Pekola, D. V. Averin, and V. K. Semenov, J. Appl. Phys. **99**, 084501 (2006).

[215] A. M. Clark *et al.*, Appl. Phys. Lett. **86**, 173508 (2005).

[216] J. P. Pekola *et al.*, Appl. Phys. Lett. **76**, 2782 (2000).

[217] A. Rothwarf and B. N. Taylor, Phys. Rev. Lett. **19**, 27 (1967).

[218] J. N. Ullom, P. A. Fisher, and M. Nahum, Phys. Rev. B **58**, 8225 (1998).

[219] S. B. Kaplan *et al.*, Phys. Rev. B **14**, 4854 (1976).

[220] A. A. Abrikosov, Zh. Eksp Teor. Fiz. **32**, 1442 (1957), [Sov. Phys. JETP 5, 1174 (1957)].

[221] J. N. Ullom, P. A. Fisher, and M. Nahum, Appl. Phys. Lett. **73**, 2494 (1998).

[222] K. Y. Arutyunov, T. I. Suppula, J. K. Suoknuuti, and J. P. Pekola, J. Appl. Phys. **88**, 326 (2000).

[223] A. Vasenko and F. Hekking, J. Low Temp. Phys. **154**, 221 (2009).

[224] A. Glatz, N. M. Chtchelkachev, I. S. Beloborodov, and V. Vinokur, arXiv:1106.4297 (2011).

[225] A. J. Manninen, M. M. Leivo, and J. P. Pekola, Appl. Phys. Lett. **70**, 1885 (1997).

[226] A. Luukanen *et al.*, J. Low Temp. Phys. **120**, 281 (2000).

Aalto-DD 112/2011

ISBN 978-952-60-4351-7 (pdf)
ISBN 978-952-60-4350-0
ISSN-L 1799-4934
ISSN 1799-4942 (pdf)
ISSN 1799-4934

Aalto University
School of Science
Low Temperature Laboratory
www.aalto.fi

BUSINESS +
ECONOMY

ART +
DESIGN +
ARCHITECTURE

SCIENCE +
TECHNOLOGY

CROSSOVER

DOCTORAL
DISSERTATIONS